A search for new physics in multijet final states of pp collisions at $\sqrt{s} = 13\ TeV$ using the ATLAS detector at the Large Hadron Collider

by

Brian Amadio

A dissertation submitted in partial satisfaction of the

requirements for the degree of

Doctor of Philosophy

in

Physics

in the

Graduate Division

of the

University of California, Berkeley

Committee in charge:

Professor Marjorie Shapiro, Chair
Professor Barbara Jacak
Professor Karl A. van Bibber

Fall 2017

A search for new physics in multijet final states of pp collisions at $\sqrt{s} = 13\ TeV$ using the ATLAS detector at the Large Hadron Collider

Abstract

A search for new physics in multijet final states of pp collisions at $\sqrt{s} = 13\ TeV$ using the ATLAS detector at the Large Hadron Collider

by

Brian Amadio

Doctor of Philosophy in Physics

University of California, Berkeley

Professor Marjorie Shapiro, Chair

Abstract goes here.

To Someone

Dedication goes here

Contents

Contents ii

List of Figures iv

List of Tables viii

1 Introduction 1

2 The Standard Model of Particle Physics 2
2.1 Electroweak Sector and the Higgs Mechanism . . . 3
2.2 Quantum Chromodynamics . . . 6
2.3 Limitations . . . 10

3 Supersymmetry 12
3.1 Motivation for New Physics . . . 12
3.2 Theory and Phenomenology . . . 16
3.3 R-Parity and R-parity Violation . . . 18

4 The LHC and ATLAS Detector 22
4.1 The Large Hadron Collider . . . 22
4.2 Coordinates . . . 28
4.3 Magnet Systems . . . 29
4.4 Inner Detector . . . 29
4.5 Calorimeters . . . 38
4.6 Muon Spectrometer . . . 43
4.7 Trigger . . . 49

5 Jets 52
5.1 The proton-proton collision environment . . . 52
5.2 Clustering Algorithms . . . 54
5.3 Boosted objects . . . 58
5.4 Reconstruction in ATLAS . . . 62

6 Search Strategy **68**
6.1 Strategy Overview 68
6.2 Discriminating Variables 68
6.3 Data-Driven Background Estimation 69
6.4 Event Selection 73
6.5 Control, Uncertainty Determination, Validation, and Signal Regions 74
6.6 Background Systematic Uncertainty 75
6.7 Signal Contamination 77

7 Signal Modelling and Systematics **81**
7.1 Signal Modeling 81
7.2 Signal Systematic Uncertainties 81

8 Results **83**
8.1 Data-driven Background Uncertainty 83
8.2 Background Predictions and Observed Yields in Signal Regions 83
8.3 Signal Systematics 83
8.4 Statistical Interpretation 83
8.5 Expected and Observed Limits 83

9 Conclusions **84**

Bibliography **85**

List of Figures

2.1 Summary of Standard Model production cross sections measured by ATLAS, compared to theoretical predictions. 3
2.2 Measured values of the strong coupling constant α_s and its predicted values across a range of energies 8
2.3 Parton distribution functions for the proton, calculated at NLO for two different energy scales. 9

3.1 Top-quark loop diagram, the leading correction to the Higgs mass-squared. This contribution is quadratically divergent in the cutoff scale. 13
3.2 Stop loop diagram, the leading SUSY correction to the Higgs mass-squared. This contribution is quadratically divergent in the cutoff scale. 13
3.3 Running of the three Standard Model coupling constants under the Standard Model (left) and MSSM (right) RGEs. For the MSSM, unification occurs at $\mu \approx 2 \times 10^{16}$ GeV 15
3.4 Tree-level diagram for the decay $p^+ \to \pi^0 e^+$, with both L-violating and B-violating vertices. 20
3.5 Diagrams for the two decay processes that are the subject of this search. The direct decay (left) and cascade decay (right) both involve effective RPV vertices containing off-shell squark propagators. 21

4.1 Cumulative luminosity delivered by the LHC over time for each of the years from 2011 to 2018. 23
4.2 Schematic of the LHC layout. The clockwise-rotating beam, shown in red, is referred to as beam 1, and the counter-clockwise-rotating beam, shown in blue, is beam 2. Locations of the four major detector experiments are labelled. 25
4.3 Cross-section schematic of an LHC dipole magnet. 26
4.4 Schematic of a cryomodule, containing four RF cavities used to accelerate and store the LHC beam. 27
4.5 A diagram showing the layout of the ATLAS magnet system. The central solenoid is used to apply a force that curves the trajectories of charged particles in the inner detector. In red are the toroid coils, used to bend the tracks of charged particles passing through the muon spectrometer. 30

4.6 A picture of the ATLAS barrel toroid after installation. In the center of the image is the calorimeter and central solenoid, before being moved into the final position. 31
4.7 A quarter-section plan showing the layout of inner detector susbystems and their dimensions. Not shown is the innermost layer of the pixel detector, the IBL, which was installed in May 2014. 32
4.8 Graphic illustrating how n^+-in-n pixel sensors continue to operate after the type inversion that results from irradiation. In (a), the unirradiated state, the bulk is n-type, and the depletion zone occurs between the p^+-doped back side. After type inversion, in (b), the depletion zone occurs between the now p-type bulk and the n^+-doped front side. [12] 33
4.9 The IBL as it was inserted into the pixel detector 34
4.10 Part of a TRT end-cap, showing the radial layout of the 37 cm straw tubes. . . 36
4.11 Schematic of the TRT straw wall design. Two coated Kapton layers are sealed together with polyurethane. 37
4.12 Layout of the ATLAS calorimeter system. 39
4.13 Schematic of EM calorimeter, showing the granularity of each layer. 40
4.14 Schematic of EM calorimeter, showing the granularity of each layer. 42
4.15 Schematic of the central (left) and extended (right) tile calorimeter, showing the η- and depth-dependent segmentation. 43
4.16 Schematic of hadronic end-cap calorimeter module 44
4.17 Schematic showing the layout of the forward calorimeters and end-cap calorimeters. 45
4.18 Amount of material, in units of interaction length, versus pseudorapidity, including all material before the EM calorimeter, the EM calorimeter, and the hadronic calorimeters. The light blue indicates the amount of material in front of the muon spectrometer for $|\eta| < 3.0$ 46
4.19 Layout of the muon spectrometer, indicating the location of barrel and end-cap toroids, along with the four subsystems. 47
4.20 Cross-sections in $x-y$ (left) and $y-z$ (right) of the muon spectrometer. 47
4.21 The contribution to muon spectrometer p_T resolution from various sources over a range of p_T 48
4.22 Flowchart outlining the level 1 and high-level trigger design and data acquisition system. 50

5.1 Diagram of a proton-proton collision event in which the hard scatter process is $t\bar{t}H$ production. Illustrated are the initial state radiation, underlying event, hard-scatter process, final state parton shower, fragmentation, hadron decays, and final state QED radiation. 53
5.2 Illustration comparing the results of collinear-safe (left) and collinear-unsafe (right) jet clustering algorithms. The emission of a near-collinear gluon changes the number of jets in the event, and results in diverges in theoretical calculations. The x-axis represents rapidity, and y-axis represents transverse momentum. 56

5.3 Illustration of infrared unsafety. In an event with a W boson decaying to two hard partons, the emission of a soft gluon can change the result of an infrared-unsafe algorithm. 57
5.4 Results of running four different jet clustering algorithm on the same set of parton-level simulated event data. SISCone (lower-left) is a cone-based algorithm, while the other three are sequential recombination algorithms defined by different values of p. 59
5.5 Radial separation between top decay products vs. top-quark p_T for top quarks produced from a theoretical heavy resonance, Z' 60
5.6 Illustration of the trimming procedure, one of several grooming methods used to remove the contribution of unassociated radiation to fat jet mass. 62
5.7 Measured jet mass distributions before and after grooming, for various grooming techniques. Mass distributions are shown for both dijet events (left) and $t\bar{t}$ events (right). 62
5.8 Average energy and energy resolution measured for 180 GeV and 20 GeV pions with different values of the topo-clustering parameters S, N, and P. The x-axis of each plot represents choices for all three parameters, and the y-axis indicates either the average energy deposited in each cluster $< E_{clusters} >$ or the energy resolution $RMS / < E_{clusters} >$ 64
5.9 Cluster EM probability as a function of normalized cell signal density and depth. Cell that are farther away from their cluster's center, and with lower energy density are more likely to arise from hadronic showers. The red line indicates the 50% boundary: cells falling on that line have a 50% probability of arising from electromagnetic showers, while clusters below that line have a higher probability. 65
5.10 Illustration of the procedure used to account for signal lost to lost cells and dead material. 67

6.1 Distributions of the two main discriminating observables, (a) the scalar sum of the four leading large-R jets, M_J^{Σ} and (b) the difference in pseudorapidity between the two leading jets, $|\Delta\eta_{12}|$. Selected events have ≥ 4 large-R jets. Distributions are shown for both data and simulated signal and background samples. The red and green signal distributions are for the cascade decay mode, and the violet distribution is the direct decay mode, for the superpartner masses indicated. . . 69
6.2 Two representative template distributions used in the analysis, showing a comparison between data in black and simulation in red. The solid markers show the templates derived from b-matched jets, while the empty markers show the templates derived from non-b-matched jets. In (a), template jets are required to have 600 $GeV < p_T <$ 644 GeV and $0.5 < |\eta| < 1.0$. In (b), templates jets are required to have 733 $GeV < p_T <$ 811 GeV and $1.5 < |\eta| < 2.0$. 70
6.3 Number of jets contributing to each template bin for the non-b-matched (left) and b-matched (right) templates. 71
6.4 Average dressed and kinematic jet masses for each p_T bin in the control region . 73

6.5 Jet mass response plots showing the discrepancy between average dressed and kinematic jet masses in the two uncertainty determination regions, binned by p_T and $|\eta|$. Since the discrepancy is always larger in UDR1, only UDR1 is used to derive uncertainties. 78
6.6 Signal injection test. The background prediction is first run only on a data sample (a), and then on a data sample injected with simulated signal events (b). The increase in background prediction and systematic uncertainty can be seen. . . . 79
6.7 The effect of signal contamination on the nominal background prediction. At each neutralino and gluino mass, simulated signal events are used in the kinematic sample to generate a background prediction. These predictions are compared to the prediction from data only. In both cases, the templates are drawn only from data. 80

List of Tables

3.1 The MSSM chiral superfields, including their names, symbols, and components. Quantum numbers for the Standard Model symmetry group transformations are also given. . . . 17
3.2 The MSSM gauge superfields, including their names, symbols, and components. Quantum numbers for the Standard Model symmetry group transformations are also given. . . . 18

6.1 Summary of the requirements defining the control, uncertainty determination, validation, and signal regions. Requirements are placed on the large-R jet multiplicity (N_{jet}), the presence or absence of a b-tagged small-R jet (b-tag), the p_T of the leading jet ($p_{T,1}$), the pseudorapidity difference between the two leading jets ($|\Delta\eta_{12}|$), and the scalar sum of the first four leading jets in the event (M_J^{Σ}). . . 75

Acknowledgments

Here I acknowledge all the people who helped me along the way.

Chapter 1

Introduction

Chapter 2

The Standard Model of Particle Physics

The Standard Model is a set of theories describing the interactions between elementary particles. It explains three of the four known fundamental forces, namely the electromagnetic force, the weak nuclear force, and the strong force. It does not include or account for gravitational interactions.

The Standard Model can be fairly characterized as one of the most successful theories in science. A huge number of predictions made by the theory have been confirmed experimentally, some to an astounding degree of accuracy. Precision measurements of the magnetic moment of the electron have shown the experimental and theoretical values of the fine structure constant to agree better than one part in one billion.[24] The ATLAS detector at the LHC has confirmed the predicted rate of particle production for a very wide range of production processes and final states. A summary of Standard Model measurements made by ATLAS, and their comparisons to theoretical predictions can be seen in figure 2.1. The Standard Model predicted the existence of the W boson, the top quark, and the Higgs boson, which were all later confirmed by experiment.

The Standard Model is expressed in the language of Quantum Field Theory. The theory consists of three generations of matter fields, specified by their representation under the gauge group $SU(3) \times SU(2) \times U(1)$ and the Poincaré group, as well as a complex scalar field. Poincaré symmetry consists of the Lorentz symmetry of special relativity, plus global translational symmetry.

The Standard Model is a complete theory in the sense that it is internally self-consistent, and all particles predicted by the theory have been discovered experimentally. However, the Standard Model does not account for all known physical phenomena, and so cannot be considered a complete theory of nature.

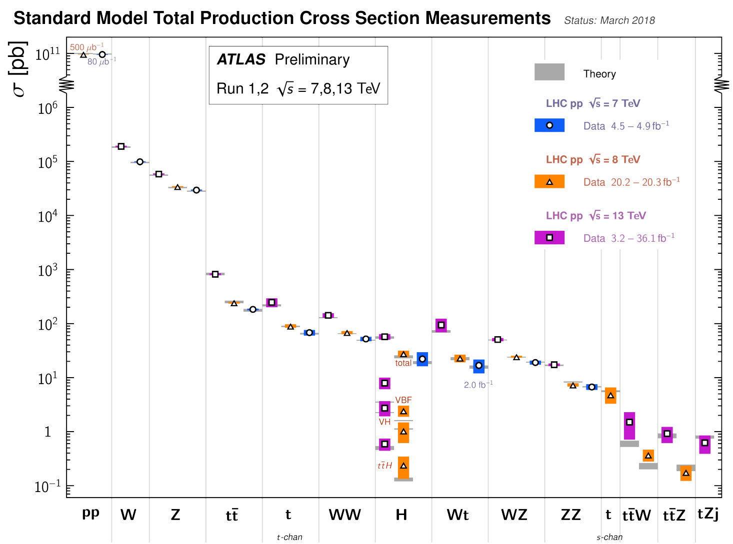

Figure 2.1: Summary of Standard Model production cross sections measured by ATLAS, compared to theoretical predictions.

2.1 Electroweak Sector and the Higgs Mechanism

Matter fields

All left-handed matter fields are $SU(2)$ doublets, while their corresponding right-handed fields are $SU(2)$ singlets. There are three generations of left-handed lepton fields:

$$\psi_L = \begin{pmatrix} \nu_e \\ l_e \end{pmatrix}_L, \begin{pmatrix} \nu_\mu \\ l_\mu \end{pmatrix}_L, \begin{pmatrix} \nu_\tau \\ l_\tau \end{pmatrix}_L \tag{2.1}$$

And three generations of right-handed lepton fields:

$$\psi_R = e_R,\ \mu_R,\ \tau_R \tag{2.2}$$

Similarly, there are three generations each of the left-handed $SU(2)$-doublet quark fields, each of which comes in three colors:

$$\psi_L = \begin{pmatrix} q_u \\ q_d \end{pmatrix}_L, \begin{pmatrix} q_c \\ q_s \end{pmatrix}_L, \begin{pmatrix} q_t \\ q_b \end{pmatrix}_L \tag{2.3}$$

Quark color will play a role in QCD interactions, as discussed in the next session. There are also the corresponding $SU(2)$-singlet right-handed fields:

$$\psi_R = q_{uR},\ q_{dR},\ q_{cR},\ q_{sR},\ q_{tR},\ q_{bR} \tag{2.4}$$

Symmetries and Lagrangian

The symmetry constraining the electroweak sector of the Standard Model Lagrangian is $SU(2)_L \times U(1)_Y$. The subscript L for the $SU(2)$ group indicates that it only acts on the left-handed fields in the theory. As we've seen, right-handed fields appear as $SU(2)$ singlets. The Lagrangian density satisfying the required symmetries, including all renormalizable terms, is:

$$\mathcal{L}_{EW} = \mathcal{L}_{kin} + \mathcal{L}_{\text{interactions}} \tag{2.5}$$

The kinetic part of the electroweak Lagrangian is:

$$\mathcal{L}_{kin} = -\frac{1}{4} W_a^{\mu\nu} W_{\mu\nu}^a - \frac{1}{4} B^{\mu\nu} B_{\mu\nu} \tag{2.6}$$

Where W_μ^a are the three $SU(2)_L$ gauge bosons, B_μ is the $U(1)_Y$ (hypercharge) gauge boson, and $W_\mu\nu = \partial_\mu W_\nu - \partial_\nu W_\mu$.

The part of the electroweak Lagrangian describing electroweak interactions is:

$$\mathcal{L}_{\text{interactions}} = \sum_{\text{generations}} \left[\frac{g}{2} \bar{\psi}_L \gamma^\mu \sigma^i W_\mu^i \psi_L + g' B_\mu \left(Y_{\psi_L} \bar{\psi}_L \gamma^\mu \psi_L + Y_{\psi_R} \bar{\psi}_R \gamma^\mu \psi_R \right) \right] \tag{2.7}$$

Where γ^μ are the Dirac gamma matrices, Y is the hypercharge associated with the relevant field. Left-handed leptons and quarks have weak hypercharge $Y = -1$ and $Y = 1/3$, respectively. Right-handed leptons have weak hypercharge $Y = -2$, while right-handed up-type quarks have weak hypercharge $Y = 4/3$, and right-handed down-type quarks have weak hypercharge $Y = -2/3$.

This Lagrangian describes the charged-current and neutral-current weak interactions, as well as weak gauge boson self-interactions. However, it is insufficient to describe nature because the gauge bosons are massless in this theory. It would be impossible to include gauge boson mass terms in the electroweak Lagrangian without explicitly breaking the symmetry. Similarly, it's impossible to introduce Lorentz-invariant fermion mass terms that keep the Lagrangian invariant under $SU(2)_L \times U(1)_Y$. In order to reconcile this theory with the experimentally observed fact of massive weak gauge bosons and massive fermions, an entirely new field will have to be introduced.

Spontaneous symmetry breaking

The original $SU(2)_L \times U(1)_Y$ symmetry will be spontaneously broken, via the nonzero Higgs vacuum expectation value, to $U(1)_{QED}$. This process of spontaneous symmetry breaking (SSB) generates fermion masses, electroweak gauge boson masses, and the Yukawa coupling terms between fermions. It also generates a new massive real scalar field, known as the Higgs field.

We introduce a new $SU(2)$-doublet complex scalar field, ϕ, as well as a potential of the form:

$$V(\phi) = \mu^2 \phi^\dagger \phi + \lambda (\phi^\dagger \phi)^2 \tag{2.8}$$

With $\lambda > 0$ and $\mu^2 < 0$. The minimum energy state satisfies: $\phi^\dagger \phi = \frac{-\mu^2}{2\lambda}$.
We can then re-parameterize the scalar field as:

$$\phi = \exp\left(i \frac{\sigma_i}{2} \theta^i(x)\right) \frac{1}{\sqrt{2}} \begin{pmatrix} 0 \\ v + H(x) \end{pmatrix} \tag{2.9}$$

Where $H(x)$ and $\theta^i(x)$ are real-valued fields, and $v = \sqrt{\frac{-\mu^2}{\lambda}}$ is the vacuum expectation value of the Higgs field.

Because of the $SU(2)_L$ symmetry of the theory, we are free to choose convenient values for $\theta_i(x)$, without affecting the outcome of any observable predictions. Selecting $\theta_i(x) = 0$, the additional kinetic term required in the Lagrangian is:

$$\Delta \mathcal{L}_{EW} = (D_\mu \phi)^\dagger (D_\mu \phi) = \frac{1}{2} \partial_\mu H \partial^\mu H + (v + H)^2 \left(\frac{g^2}{4} W_\mu^\dagger W^\mu + \frac{g^2}{8 \cos^2 \theta_W} Z_\mu Z^\mu \right) \tag{2.10}$$

Where W_μ and Z_μ are mass eigenstates of the electroweak gauge fields, linear combinations of the original W_μ^a and B_μ.

This has added interaction terms between the Higgs field and the W and Z bosons, as well as quadratic terms for these same bosons. A quadratic term in the Lagrangian is physically the same as having a mass term in the Lagrangian.

So we find that the W and Z boson masses are:

$$M_w = \frac{1}{2} v g, \; M_Z = \frac{M_W}{\cos \theta_W} \tag{2.11}$$

Through SSB, electroweak gauge boson masses have been generated without requiring explicit mass terms in the Lagrangian.

The introduction of this scalar field and its associated potential will also generate fermionic mass terms, couplings between the fermions and the scalar field, and a mass term for the scalar field itself.

Like with the gauge bosons, adding an explicit fermionic mass term would break the $SU(2)_L \times U(1)_Y$ symmetry of the theory. However, the introduction of the new scalar field allows for additional terms in the Lagrangian, which can be written, in unitary gauge, as:

$$L_Y = \frac{1}{\sqrt{2}} (v + H) \left(c_1 \bar{d} d + c_2 \bar{u} u + c_3 \bar{e} e \right) \tag{2.12}$$

Once again, after spontaneous symmetry breaking, there appear terms in the Lagrangian that are quadratic in the fields. These are mass terms for the fermions, and like for the gauge bosons, the masses are proportional to the Higgs vacuum expectation value.

$$m_d = -c_1\frac{v}{\sqrt{2}},\ m_u = -c_2\frac{v}{\sqrt{2}},\ m_e = -c_3\frac{v}{\sqrt{2}} \tag{2.13}$$

Unlike for the gauge bosons, we find no testable relationship between the fermion masses, since the coefficients are all free parameters of the theory.

The Higgs mechanism allows for the generation of masses for electroweak gauge bosons and for fermions without explicitly breaking the original symmetry of the theory. Additional consequences arising from the Higgs mechanism are the relationship between Z and W boson masses, the existence of a new massive scalar field, and interactions between this field and the fermions and gauge bosons. The massive particle associated with this field, the Higgs boson, was discovered in 2012 by the ATLAS and CMS collaborations.

2.2 Quantum Chromodynamics

Quantum Chromodynamics (QCD) is the part of the Standard Model concerned with strong interactions. Because protons are bound states of quarks and gluons, QCD is needed for making any calculation of event rates at a proton-proton collider. It's particularly important for understanding the behavior of jets, which will be described in detail in chapter 5. The particular structure of the theory yields very different behavior at high energy and low energy. At high energy, where the coupling strength is low, quarks and gluons are only weakly bound, so the theory behaves as an approximately free theory, a property known as asymptotic freedom. At lower energies, the coupling strength grows, and quarks and gluons become strongly bound, a property known as confinement.

Matter fields

The fields involved are the quark fields, which also participate in electroweak interactions. In the case of QCD, the quarks are in the fundamental **3** representation of $SU(3)$:

$$\psi = \begin{pmatrix} \psi_R \\ \psi_G \\ \psi_B \end{pmatrix} \tag{2.14}$$

Where R, G, B stand for the red, green, and blue color charges. The theory will be invariant under local transformations of this color space.

Symmetries and Lagrangian

Like the electroweak theory, QCD is a non-Abelian gauge theory. The Lagrangian is generated by positing the transformations under which the Lagrangian is invariant, and including all terms that respect these symmetries. For QCD, the symmetry group is $SU(3)$, yielding the following Lagrangian:

$$\mathcal{L}_{QCD} = \sum_{generations} i\bar{\psi} D_\mu \gamma^\mu \psi - \frac{1}{4} G^a_{\mu\nu} G^{\mu\nu}_a \tag{2.15}$$

Where

$$D_\mu = \partial_\mu - i g_s G^a_\mu T^a \tag{2.16}$$

is the gauge-covariant derivative, g_s is the strong coupling constant, G^a_μ are the eight gluon fields, and T^a are the infinitesimal generators of $SU(3)$. The gluon field strength tensor, $G^a_{\mu\nu}$, is defined as:

$$G^a_{\mu\nu} = \partial_\mu G^a_\nu - g_s f^{abc} G^b_\mu G^c_\nu \tag{2.17}$$

Where f^{abc} are the $SU(3)$ structure constants. This Lagrangian describes the kinematics of massless quarks, their interactions with gluons, and gluon self-interactions. Quarks are given mass through electroweak symmetry breaking, as described in 2.1.

QCD coupling constant

A consequence of the gluon self-interaction in the QCD Lagrangian is that the value of the strong coupling constant, g_s, depends on the energy scale. The rate of change of the coupling as energy increases is governed by the β function,

$$\beta\left(\alpha_s\right) = \frac{\alpha_s}{2\pi}\left(\frac{11}{3} n_{\text{colors}} - \frac{4}{3} n_{\text{flavors}}\right) \tag{2.18}$$

Where $\alpha_s = g_s^2/4\pi$. In QCD, there are three colors and three flavors, the consequence of which is that the coupling constant descreases with energy. This is known as the ”running” of the coupling constant, and results in very different predictions for the theory at different energy scales. Figure 2.2 shows the predicted value of α_s over a range of energies, along with values measured through a variety of physics processes.

[35]

Asymptotic freedom

At very high energies, at or above the GeV scale, the strong coupling constant becomes small. As a result, QCD calculations in this regime are *perturbative*, meaning they can be approximated by a finite sum of terms expanded in powers of the coupling constant. This is similar to the way calculations are done in quantum electrodynamics (QED).

Asymptotic freedom means that as energy grows infinite, quarks and gluons can be treated as completely un-coupled, free particles. At very high energies, their interactions can be treated as small perturbations about the free theory. At the LHC, the hard-scattering cross-section of a quark from one proton colliding with a quark from another proton can be

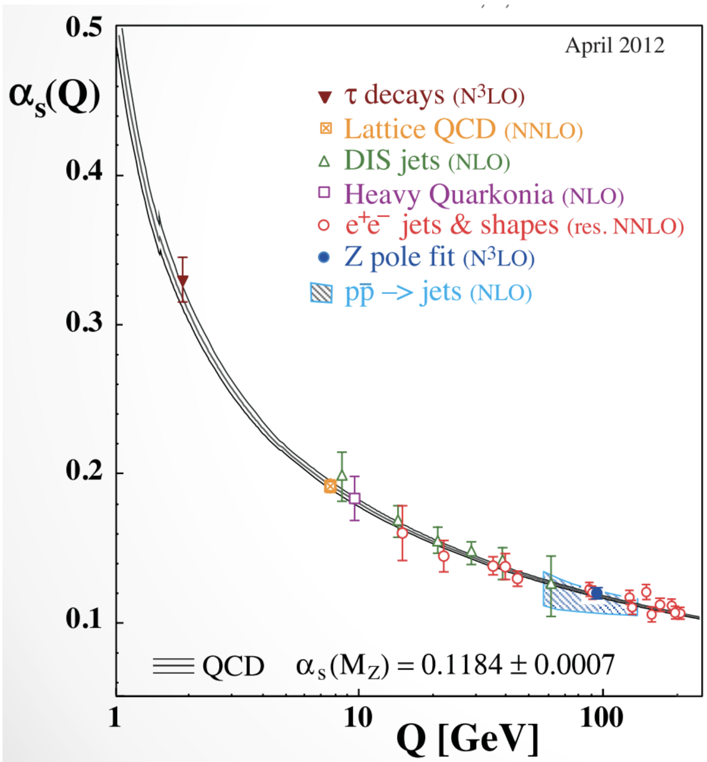

Figure 2.2: Measured values of the strong coupling constant α_s and its predicted values across a range of energies

calculated in this perturbative way. However, the full proton-proton collision cross-section calculation requires a combination of both perturbative and non-perturbative calculations.

Confinement and Hadronization

At lower energies, the strong coupling constant grows larger, and the theory can no longer be treated as perturbative. Because the coupling constant is large, a finite series expanded in powers of the coupling constant is no longer sufficient to estimate the full predictions. Instead, higher-order terms grow larger and larger, which means an infinite number of such terms would be needed to make an accurate prediction.

The exact energy scale at which QCD becomes non-perturbative is not known, but experimental evidence indicates that it occurs below approximately 200 GeV.

Confinement is a consequence of the large coupling constant at low energies. Since quarks and gluons are strongly coupled, they can no longer exist as free states. Instead, they can only exist as color-neutral bound states, called hadrons.

In a collision event, when a quark is generated in the final state, the strong force between the quark and other quarks in the event remains constant as distance between them increases. Equivalently, the potential energy between quarks increases with distance. Eventually it becomes energetically favorable for new quarks to be created from the vacuum, with the correct color charge to neutralize the color charge of the escaping quark. These new particles become bound together in color-neutral free states. This process is known as hadronization.

Hadronization, along with parton showering, is responsible for the emergence of jets from LHC collisions. Rather than observing the quarks and gluons produced in the collision, the detector can only observe the spray of hadrons that result. Jets will be discussed in detail in chapter 5.

Confinement has not been rigorously proven from a theoretical standpoint. However, the existence of color confinement is consistent with empirical evidence.

Parton distribution functions

The QCD Lagrangian describes how individual quarks and gluons behave. But the LHC collides protons, not individual quarks. Protons consist of three valence quarks: two up quarks and one down quark. But they also consist of a "sea" of quarks and antiquarks, as well as gluons. When calculating collision cross-sections for the LHC, this internal structure of the protons must be taken into account.

Parton distribution functions (PDFs) model the internal structure of the proton. They are expressed as probability distributions over momentum fraction x, normalized to the number of partons. The momentum fraction x, is the proportion of the proton momentum carried by the individual parton. PDFs are conditional on Q^2, the squared energy scale. Separate PDFs are calculated for gluons and for each quark flavor.

Examples of PDFs for different quark flavors, as well as for gluons, can be seen in figure 2.3.

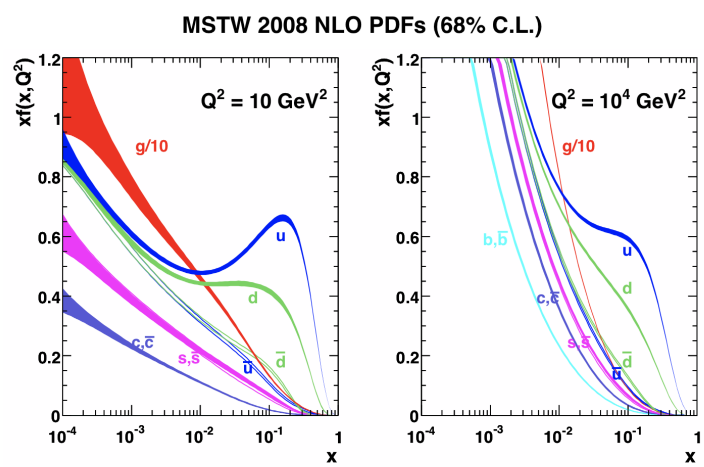

Figure 2.3: Parton distribution functions for the proton, calculated at NLO for two different energy scales.

[30]

When calculating LHC cross-sections, the hard-scattering cross-section for different types of partons must be convolved with the PDFs for each parton. The proton-proton cross-sections are thus an average of partonic cross-sections, weighted by the PDFs for those partons.

The factorization theorem of QCD allows for the non-perturbative PDF calculations to be carried out independently from the perturbative hard scattering cross sections, and then combined.

2.3 Limitations

Experimental tests of the Standard Model to date have shown no significant deviations from its predictions, across a very wide range of physical processes and energy scales. However, it is quite clear that the Standard Model is not a complete theory of nature. For one, it makes no attempt to account for gravitational interactions. But there are many other problems and questions that it leaves unanswered.

Fine tuning and the Higgs mass

The Higgs field, which is responsible for the mass of all fundamental fermions and the massive electroweak gauge bosons, was confirmed by the discovery of 125 GeV Higgs boson by ATLAS and CMS in 2012. The fact that the Higgs mass should be so small is an unsolved mystery of particle physics.

When performing QFT calculations, there often arise terms in the perturbation expansion that are formally infinite. A procedure known as renormalization is used in order to tame these divergences. One method of renormalization involves cutting off the divergent integrals at some scale, Λ, then canceling the infinities by redefining some of the free parameters of the theories.

When calculating the physical mass-squared of the Higgs, there are some terms in the series which are proportional to the square of the cutoff scale. The cutoff scale is considered to be some very large energy scale, usually the Planck energy 10^{19} GeV. As a result, an infinite sum of positive and negative terms with absolute values on the order of 10^{38} GeV^2 must cancel out to yield physical Higgs mass-squared, which is on the order of 10^4 GeV^2. This kind of cancellation is philosophically unsatisfying, because it seems to be an unreasonable amount of fine-tuning.

The fine-tuning is closely related to the so-called "hierarchy problem". Why is gravity so much weaker than the other fundamental forces? That is, why do we observe $G_F \gg G_N$? Since $G_F \propto 1/M_W^2$, and $G_N \propto 1/\Lambda_{Pl}^2$ and because M_W is proportional to the Higgs vev, the Higgs-mass fine-tuning and the hierarchy problem are really the same thing.

A possible way to avoid fine tuning and the hierarchy problem comes from Supersymmetry, which will be covered in 3

Grand unification

The symmetry groups and representations of the Standard Model have great explanatory power, but they are, at heart, axiomatic rather than derived. The Standard Model contains a large number of free parameters, the values of which are not explained by the model, but must be measured by experiment.

It's possible that a simpler model could be found, one which embeds the baroque structure of the Standard Model in a much simpler set of symmetry groups and representations. Such an idea is known as *Grand Unification*.

A Grand Unified Theory (GUT) would predict relationships between some of the free parameters of the Standard Model, resulting in a simpler and more elegant theory. This would be analogous to electroweak unification, which explains the relations between W and Z boson masses, as well as their couplings. As a result, the theory has only three free parameters, and the rest can be determined once those are known.

The GUT would explain all particle interactions with a single symmetry group. This symmetry would be broken below some energy scale to the $SU(3)_C \times SU(2)_L \times U(1)_Y$ symmetry of the Standard Model. The details of the symmetry breaking process would yield relations between the strong and electroweak coupling constants.

Going a step further, if gravitational interactions could also be incorporated into this single theory, it would be a so-called "Theory of Everything" (TOE). A very popular TOE candidate, known as String Theory, relies on the existence of Supersymmetry.

Dark Matter

The type of matter explained by the Standard Model is known to account for approximately 20% of the matter in the universe. The remaining 80% exists in the form of dark matter. The exact explanation for dark matter is not yet known, those many of its properties can be inferred. It is massive and invisible, and its primary interaction with visible matter is through gravity.

Dark matter is known to be massive, because it interacts gravitationally. This can be seen in its effect on the rotation curves of galaxies, gravitational lensing of distant galaxies, and on the anisotropy of the Cosmic Microwave Background Radiation.

Dark matter could possibly be explained by the Standard Model, if it exists in the form of Massive Compact Halo Objects (MACHOs). This form of dark matter is become less and less favored by experimental measurements over time.

Another likely explanation for dark matter is that it is composed of a new fundamental particle, one which is not explained by the Standard Model. Many versions of Supersymmetry, described in 3, provide a viable dark matter candidate.

Chapter 3

Supersymmetry

Supersymmetry (SUSY) is an extension to the Standard Model, that introduces a new space-time symmetry relating fermionic and bosonic fields. It is a remarkable theory, which has the potential to resolve many of the known problems of the Standard Model in one fell swoop.

3.1 Motivation for New Physics

As described in 2.3, the Standard Model leaves open some very important questions. These mysteries all point towards a more fundamental theory, one which is applicable at short distances scales, or equivalently, higher energies. The most important task of this new theory is to explain why the Higgs mass is so small, in a way that avoids the extreme fine-tuning required by the Standard Model. But a more fundamental theory of particle physics could potentially simplify the symmetry structure of the model, and provide an explanation for the seemingly arbitrary quantum numbers of the Standard Model particles. This new theory should not be seen as a replacement for the Standard Model, but rather an extension of it. Whatever the new theory is, it should be applicable at very short distance scales. And at low energies, it must reduce to the Standard Model. We know this because all experimental evidence gathered so far indicates the Standard Model is a correct theory up to the energy scales at which it has been probed. In this view, the Standard Model is considered an effective field theory (EFT), valid below the scale of new physics, Λ_{NP}.

Naturalness

As explained in 2.3, the Standard Model suffers from a problem of extreme fine tuning. Quadratic diverges in the quantum corrections to the Higgs mass-squared require the bare mass of the Higgs to be specified to one part in 10^{19}, which is phenomenally unlikely to happen by chance.

The quadratic divergences occur in loop diagrams, the largest contribution coming from the top quark loop, shown in figure 3.1

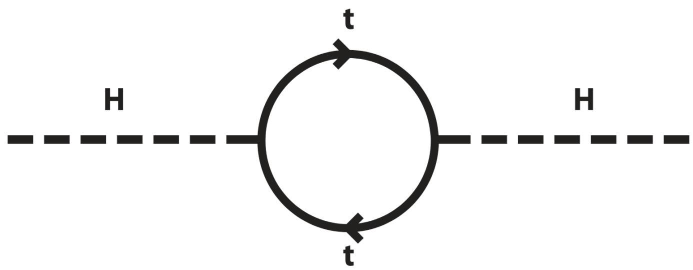

Figure 3.1: Top-quark loop diagram, the leading correction to the Higgs mass-squared. This contribution is quadratically divergent in the cutoff scale.

The correction to the Higgs mass-squared coming from this diagram is:

$$\delta m_h^2 = \frac{3m_t^2}{2\pi^2 v^2}\Lambda_{UV}^2 \tag{3.1}$$

Where m_t is the top quark mass, v is the Higgs vacuum expectation value, and Λ_{UV} is the ultraviolet cutoff. Supersymmetry introduces a so-called superpartner for each Standard Model particle. Standard Model fermions have bosonic superpartners, and Standard Model bosons have fermionic superpartners. Superpartners always have the same quantum numbers as their Standard Model partners, except for spin. The details of how this comes about will be discussed in 3.2. The superpartner of the top is called the stop. It's a scalar particle with all the same quantum numbers as the top quark, except for spin.

The introduction of superpartners leads to new quantum corrections to the Higgs mass-squared. One of those corrections can be seen in 3.2.

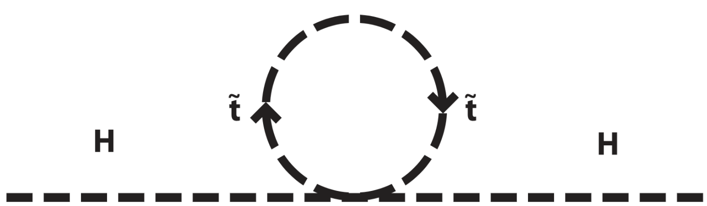

Figure 3.2: Stop loop diagram, the leading SUSY correction to the Higgs mass-squared. This contribution is quadratically divergent in the cutoff scale.

The correction to the Higgs mass-squared coming from this diagram is:

$$\delta m_h^2 = -\frac{3m_t^2}{2\pi^2 v^2}\Lambda_{UV}^2 \tag{3.2}$$

Thus, the quadratically-divergent top-loop correction is cancelled exactly. A similar cancellation occurs for all other quadratic divergences in the calculation, leaving terms that are only logarithmically divergent in the cutoff.

In SUSY, the leading correction to the Higgs mass-squared is proportional to the log of the cutoff scale, and the squared difference between the top and stop masses:

$$\delta m_h^2 \propto \left(m_{\tilde{t}}^2 - m_t^2\right) \Lambda_{UV} \tag{3.3}$$

[33]

The amount of fine-tuning required can be quantified by $m_h/\delta m_h$, so in order to preserve naturalness, the stop mass cannot be much heavier than the top quark mass. If we allow for fine-tuning of only 1 part in 10, then the stop mass shouldn't be higher than the 1 TeV scale, which indicates that SUSY should be accessible by the LHC .

Grand Unification

Grand Unification is the idea that the $SU(3)_C \times SU(2)_L \times U(1)_Y$ symmetry of the Standard Model could be embedded in a simpler symmetry group, which constrains the theory at energies above Λ_{GUT}. In a Grand Unified Theory (GUT), there would be no distinction between quarks and leptons at energies above Λ_{GUT}, and the differences in interactions between these two types of matter fields would be explained by the details of the theory and the mechanism by which it is broken. Furthermore, at energies above Λ_{GUT}, the three forces of the Standard Model would be replaced by a single, unified force. Grand unification would be the logical next step after electroweak unification, in which the electromagnetic and weak forces are shown to be the same force at energies above $\Lambda_{EW} \approx 246\ GeV$. Similarly to how electroweak unification gives a relationship between electric charge and weak isospin, grand unification would give a relationship between color charge and the electroweak quantum numbers.

Several different symmetry groups have been proposed as GUTs, including $SU(5)$, $SO(10)$, E_6, and $SU(5) \times SU(5)$.[32] However, in order for unification to occur, the value of the three Standard Model coupling constants must converge at some energy scale. The running of coupling constants is determined by the renormalization group equation (RGE):

$$\frac{\partial g}{\partial \log \mu} = \beta(g) \tag{3.4}$$

Where g is the coupling constant of interest, μ is the energy scale at which the coupling is being measured, and β is a function that depends on the gauge structure and matter content of the theory.

Using the RGE, and measured values of the coupling constants at specific starting energies, one can calculate the value of the three constants over a large range of energy scales. It turns out that for the Standard Model, there is no energy scale at which all three Standard Model constants converge, as would be required for a grand unified theory.

However, when the β function is modified to include supersymmetric particles, it is possible for all three Standard Model forces to unify. In one particular SUSY model, known as the Minimal Supersymmetric Standard Model (MSSM), unification of the forces occurs at $\mu \approx 2 \times 10^{16}$ GeV.[32] The running of the coupling constants under the Standard Model and MSSM can be seen in figure 3.3.

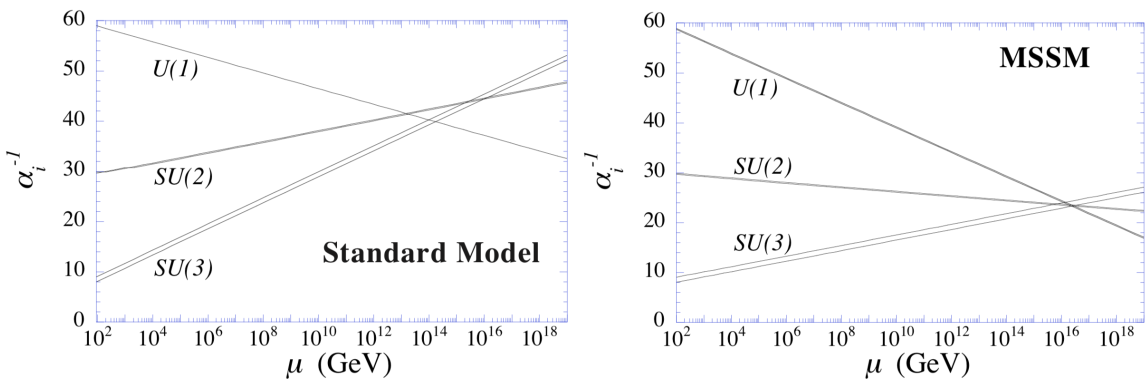

Figure 3.3: Running of the three Standard Model coupling constants under the Standard Model (left) and MSSM (right) RGEs. For the MSSM, unification occurs at $\mu \approx 2 \times 10^{16}$ GeV

[33]

Dark Matter

As mentioned in 2.3, SUSY could explain Dark Matter, which comprises approximately 80% of matter in the universe, but still cannot be explained by any known particle.

In SUSY models that conserve R-parity, the lightest supersymmetric particle (LSP) is always stable. The LSP must be stable because R-parity prevents the LSP from decaying to a final state without SUSY particles, and conservation of energy prevents it from decaying to a final state with SUSY particles, since all SUSY particles are by definition more massive than the LSP .

In so-called "natural" SUSY, the LSP is a neutralino, χ_0^1. The neutralino is a mixture of the electroweak gauge superpartners, the wino and bino, and the Higgs superpartner, the higgsino. The neutralino in this theory would be stable, massive, electrically neutral, and it would interact via the weak force. As such, it is a viable candidate for WIMP dark matter.

Intriguingly, if one assumes that dark matter was thermally produced in the early universe, and calculates the required production cross-section to match the dark matter abundance measured today, the result is $\langle \sigma v \rangle \approx 3 \times 10^{-26}$ cm^3/s, which is very close to what would be expected for a weakly-interacting LSP .[27]

3.2 Theory and Phenomenology

Supersymmetry starts by positing a transformation that converts a boson field to a fermion field and vice versa, and a Lagrangian which is invariant under such transformations. Fields are represented in supermultiplets, which always contain a Standard Model particle and its superpartner. Standard Model bosons are always paired with fermionic superpartners, and Standard Model fermions are always paired with bosonic superpartners. SUSY transformations commute with all symmetries of the Standard Model, except for the Lorentz transformations. As a result, a Standard Model particle has all the same quantum numbers as its superpartner, except for spin. Additionally, SUSY requires both members of the supermultiplet to have the same mass. Experiments have ruled out the existence of same-mass superpartners for all Standard Model particles, so for SUSY to be compatible with experimental evidence, it must be broken. The method by which SUSY is broken should have an impact on the phenomenology of the model, specifically on the differences in mass between the Standard Model particles and their superpartners. A framework called soft SUSY breaking allows for the specifics of the SUSY breaking to be factored out, by adding effective terms to the SUSY Lagrangian which account for the consequences of SUSY breaking without specifying the mechanism. These new terms break SUSY explicitly, and so this is an effective field theory, valid only at energies well below the SUSY-breaking scale.[19]

Superfields and superpotentials

Superfields can be categorized into *chiral* and *gauge* superfields. Standard model fermions and their superpartners will belong to chiral supermultiplets, while Standard Model gauge bosons and their superpartners will belong to gauge supermultiplets.

A generic chiral superfield can be represented as $\Phi(x, \theta)$, where x represents spacetime, and θ denotes the additional two fermionic degrees of freedom needed for supersymmetry transformations. It can alternatively be represented as $\Phi = (\phi, \psi)$, where ϕ is the complex scalar component, and ψ is the fermion component.

A generic *vector* superfield can be represented at $V(x, \theta, \bar{\theta})$, where $\bar{\theta}$ are the conjugate degrees of freedom to θ. In component form, vector supermultiplets can be represented as $V = (A^\mu, \lambda)$, where A^μ is the gauge boson and λ is the fermionic superpartner.

The generic supersymmetric action can then be written as:

$$S = \int d^4x \int d^2\theta d^2\bar{\theta} \Phi^\dagger e^V \Phi + \int d^4x \int d^2\theta \left(W(\Phi) + W_\lambda(V) W_\lambda(V)\right) + h.c. \tag{3.5}$$

[32]

Where the first integrand is the kinetic term for the matter fields, and the second integrand contains the generic superpotential, $W(\Phi)$, and the gauge kinetic term $W_\lambda(V)W_\lambda(V)$.

The function $W_\lambda(V)$ is defined as:

$$W_\lambda(V) = (D)^2\bar{\mathcal{D}}V \tag{3.6}$$

where $\mathcal{D} \equiv \partial_\theta - i\sigma\dot{\partial}_x$[32]

SUSY particles

In the MSSM, the minimum number of new particles and free parameters are added to the already large assortment of Standard Model ones. Each Standard Model fermion is paired with a spin-0 superpartner, and each Standard Model gauge boson is paired with a spin-1/2 superpartner. For the Higgs boson, introducing a single superpartner is not enough. There must be at least two Higgs chiral supermultiplets, with hypercharge values 1/2 and −1/2. This is needed in order to keep the electroweak theory anomaly-free, and for the Higgs mechanism to still give mass to all the fermions.[31].

Superpartner states will be denoted with a tilde, and are also referred to as sparticles. For example, the superpartner of the electron, called the selectron, will be denoted as $\tilde{e}$.

The MSSM chiral superfield content is summarized in table 3.2, and gauge superfields are summarized in table 3.2.

Names		spin 0	spin 1/2	$SU(3)_C$, $SU(2)_L$, $U(1)_Y$
squarks, quarks	Q	$(\widetilde{u}_L \;\; \widetilde{d}_L)$	$(u_L \;\; d_L)$	$(\,\mathbf{3},\, \mathbf{2}\,,\, \frac{1}{6})$
(×3 families)	$\overline{u}$	$\widetilde{u}^*_R$	$u^\dagger_R$	$(\,\overline{\mathbf{3}},\, \mathbf{1},\, -\frac{2}{3})$
	$\overline{d}$	$\widetilde{d}^*_R$	$d^\dagger_R$	$(\,\overline{\mathbf{3}},\, \mathbf{1},\, \frac{1}{3})$
sleptons, leptons	L	$(\widetilde{\nu} \;\; \widetilde{e}_L)$	$(\nu \;\; e_L)$	$(\,\mathbf{1},\, \mathbf{2}\,,\, -\frac{1}{2})$
(×3 families)	$\overline{e}$	$\widetilde{e}^*_R$	$e^\dagger_R$	$(\,\mathbf{1},\, \mathbf{1},\, 1)$
Higgs, higgsinos	H_u	$(H_u^+ \;\; H_u^0)$	$(\widetilde{H}_u^+ \;\; \widetilde{H}_u^0)$	$(\,\mathbf{1},\, \mathbf{2}\,,\, +\frac{1}{2})$
	H_d	$(H_d^0 \;\; H_d^-)$	$(\widetilde{H}_d^0 \;\; \widetilde{H}_d^-)$	$(\,\mathbf{1},\, \mathbf{2}\,,\, -\frac{1}{2})$

Table 3.1: The MSSM chiral superfields, including their names, symbols, and components. Quantum numbers for the Standard Model symmetry group transformations are also given. [31]

The MSSM superpotential is then:

$$W = h_l^{ij} e_i^c L_j H_d + h_d^{ij} Q_i d_j^c H_d + h_u^{ij} Q_i u_j^c H_u + \mu H_u H_d \tag{3.7}$$

Names	spin 1/2	spin 1	$SU(3)_C,\ SU(2)_L,\ U(1)_Y$
gluino, gluon	$\widetilde{g}$	g	$(\,\mathbf{8},\ \mathbf{1}\,,\ 0)$
winos, W bosons	$\widetilde{W}^{\pm}\quad \widetilde{W}^{0}$	$W^{\pm}\quad W^{0}$	$(\,\mathbf{1},\ \mathbf{3}\,,\ 0)$
bino, B boson	$\widetilde{B}^{0}$	B^{0}	$(\,\mathbf{1},\ \mathbf{1}\,,\ 0)$

Table 3.2: The MSSM gauge superfields, including their names, symbols, and components. Quantum numbers for the Standard Model symmetry group transformations are also given.

[31]

Where all renormalizable terms that preserve the gauge symmetries, and are holomorphic in the chiral superfields have been included, except for terms that violate baryon or lepton number conservation. The indices i, j, k are generation indices. Here, the superpotential is expressed only in terms of the left-handed superfields and components, and the hermitian conjugate terms are implied.

3.3 R-Parity and R-parity Violation

In equation 3.7, certain terms were excluded from the superpotential because they violate either baryon number or lepton number conservation. But this requirement is in fact overly constraining. While processes that violate baryon number or lepton number conservation have never been observed experimentally, neither have they been ruled out. Additionally, while there are no explicit B or L-violating terms in the Standard Model, and no perturbative process in the Standard Model violates either, there are in fact non-perturbative effects in the Standard Model which lead to violations of both.[2]

R-parity

R-parity is a new symmetry which is introduced in order to eliminate the explicit B and L-violating terms from the theory, without have to postulate that B and L are individually conserved.

Each particle has an R-Parity quantum number, defined as:

$$P_R = (-1)^{3(B-L)+2s} \tag{3.8}$$

Where B is the particle's baryon number, L is its lepton number, and s is its spin. Quarks and squarks carry baryon number 1/3, leptons an sleptons carry lepton number 1, and their corresponding antiparticles carry baryon number $-1/3$ and lepton number -1.

Every Standard Model particle has $P_R = +1$, and every sparticle has $P_R = -1$.

A necessary consequence of R-Parity conservation is the existence of a stable LSP . In an R-parity-conserving (RPC) theory, interaction vertices that involve Standard Model particles cannot involve an odd number of sparticles. As a result, when a sparticle decays, there must be at least one sparticle in the decay products, in addition to any Standard Model particles. So the lightest sparticle cannot decay, since there is no lighter sparticle for it to decay to. Furthermore, in RPC SUSY, superpartners can only be produced in pairs at collider experiments, since their production vertices necessarily include Standard Model particles.

R-parity violating superpotential terms

If R-Parity conservation is not required, additional terms should be added to the MSSM superpotential. Each term explicitly violates either baryon number or lepton number by one unit. The R-Parity-violating (RPV) superpotential terms are:

$$W_{RPV} = \frac{1}{2}\lambda_{ijk} L_i L_j \bar{e}_k + \lambda'^{ijk} L_i Q_j \bar{d}_k + \mu'^{i} L_i H_u + \frac{1}{2}\lambda''^{ijk} \bar{u}_i \bar{d}_j \bar{d}_k \tag{3.9}$$

Where μ', λ, λ', and λ'' are new coupling constants. The first three terms result in interaction vertices with $\Delta L = 1$, and the last term is has $\Delta B = 1$.

Rapid proton decay

In general, RPV SUSY would result in proton decay rates far higher than experimental bounds. The main process leading to rapid proton decay requires both the λ' and λ'' terms from equation 3.9. In this process, the proton decays to a pi^0 and a positron, via an off-shell squark. The tree-level diagram leading to such a decay is shown in figure 3.4

[31]

The tree-level rate for this process is approximately:

$$\Gamma_{p^+ \to \pi^0 e^+} \sim \frac{m_p^5}{m_{\tilde{d}}^4} \sum_{i=2,3} \left| \lambda'^{11i} \lambda''^{11i} \right|^2 \tag{3.10}$$

[31]

Experimental bounds on the proton lifetime are greater than 10^{23} years, so in order for RPV SUSY to be consistent with experiment, either the squark masses have to be extremely large, or one of the couplings λ', λ'' must be extremely small.

Specifically, the coupling and squark masses must satisfy:

$$\lambda'_{11k} \lambda''_{11k} < 10^{-23} \left(\frac{m_{\tilde{q}}}{100\ GeV} \right)^2 \tag{3.11}$$

[25]

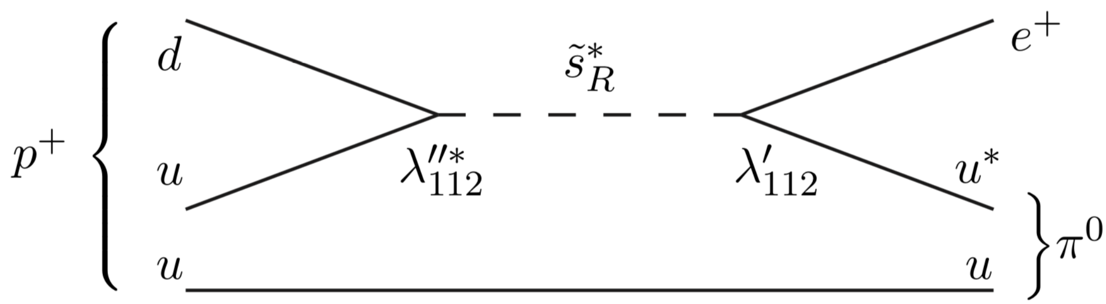

Figure 3.4: Tree-level diagram for the decay $p^+ \rightarrow \pi^0 e^+$, with both L-violating and B-violating vertices.

For the search presented here, the ad-hoc assumption that $\lambda' = 0$ is made, in order to prevent predicted proton decay rates inconsistent with experiment.

R-parity violating gluino decays

The λ'' RPV term in the superpotential allows for two potential gluino discovery channels at the LHC. The first involves pair-produced gluinos each decaying to three quarks via an effective vertex with an off-shell squark propagator. This decay mode will be referred to as the direct decay model.

The second decay mode has the gluino first decaying to two quarks and an on-shell neutralino, via an RPC vertex, and then the neutralino decaying to thre quarks through an effective RPV vertex, which also includes an off-shell squark propagator. This is the cascade decay model.

Diagrams for these two decay modes are shown in figure 3.5

Both decay modes result in a large number of high-momentum jets in the event. The production and decay rates will depend on the values of the gluino mass, neutralino mass, and λ''. A detailed discussion of the signal modeling is presented in chapter 7.

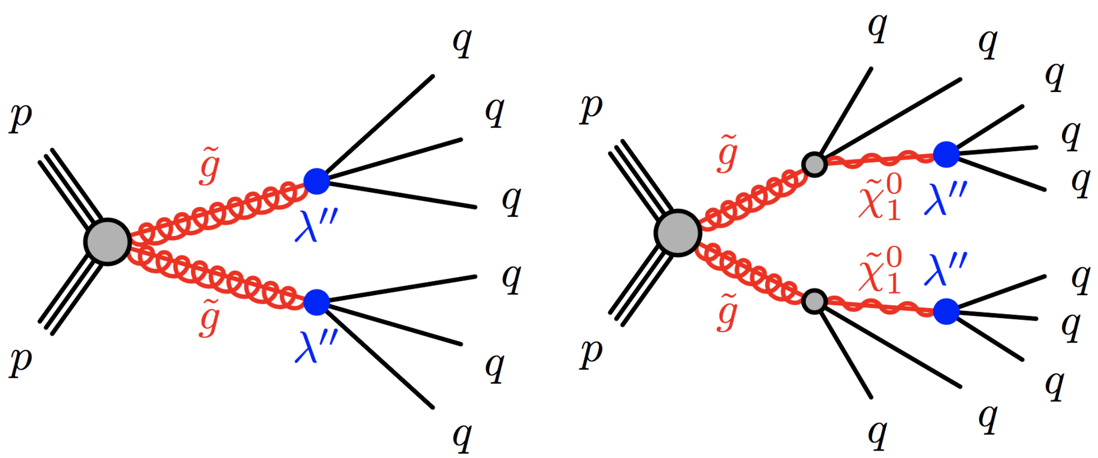

(a) gluino direct decay model (b) gluino cascade decay

Figure 3.5: Diagrams for the two decay processes that are the subject of this search. The direct decay (left) and cascade decay (right) both involve effective RPV vertices containing off-shell squark propagators.

Chapter 4

The LHC and ATLAS Detector

ATLAS is a system of particle detectors built to measure collisions of both proton-proton and heavy ion collisions generated by the LHC.[16] The full detector is 44 m long and 25 m in diameter. It consists of an inner detector subsystem for charged particle tracking and electron identification, electromagnetic and hadronic calorimeters, and a muon spectrometer.

4.1 The Large Hadron Collider

The Large Hadron Collider (LHC) is the world's largest, highest-energy, and highest-luminosity particle accelerator. It is located inside a 27 km circular underground tunnel below the French-Swiss border. The LHC was built to generate 14 TeV center-of-mass energy proton-proton collisions, as well as lead-ion collisions at a center-of-mass energy of 2.7 TeV/u. There are two counter-rotating beams of particles, which are accelerated to nearly the speed of light and steered into each other at predefined collision points along the ring, where detectors have been built to measure the particles generated in the collisions. The actual collision energy achieved for proton-proton collisions is 13 TeV, with a peak luminosity of 10^{24} $cm^{-2}s^{-1}$.[29].

Collisions generated by the LHC are measured by seven different experiments. The original four experiments are ATLAS, CMS, LHCb, and ALICE . ATLAS and CMS are the two general-purpose detectors designed for a variety of measurements and searches for physics beyond the Standard Model. They are mainly used to study proton-proton collisions, but are also used for heavy-ion collisions. LHCb, as the name implies, is a specialized detector built to measure the decays of B mesons. ALICE is a specialized detector for studying Pb − Pb collisions. In addition to these four experiments, there are three smaller, specialized experiments called TOTEM, LHCf, and MoEDAL .

The LHC is actually the last in a chain of progressively larger accelerators, each of which adds additional energy to the proton beams until they are injected into the LHC for the final acceleration. Atoms from a bottle of Hydrogen gas are passed through an electric field to strip their electrons, resulting in bare protons. These bare protons are passed into a linear accelerator known as Linac2, which accelerates them to 50 MeV. The Proton Synchrotron

Booster (PSB) then accelerates the beams to 1.4 GeV, before injecting them into the Proton Synchrotron (PS), which accelerates them to 25 GeV. The final link in the injection chain before the LHC is the Super Proton Synchrotron, which accelerates the beams up to 450 GeV per proton. The LHC provides the final boost up to 6.5 TeV per proton. This final stage of acceleration takes approximately 20 minutes, after which the beams can circulate at this energy for at least 10 hours.

The LHC was not always operating at 13 TeV. It took a number of years, over which the energy was increased in steps, before this energy could be reached. The cumulative luminosity delivered over time each year from 2011 to 2018 is shown in figure 4.1. The LHC was shut down for most of 2013 and 2014 for the upgrade to 13 TeV to take place. The most time-consuming part of the upgrade involved cycles of cooling and quenching of the superconducting dipole magnets, which is known as "training" the magnets.

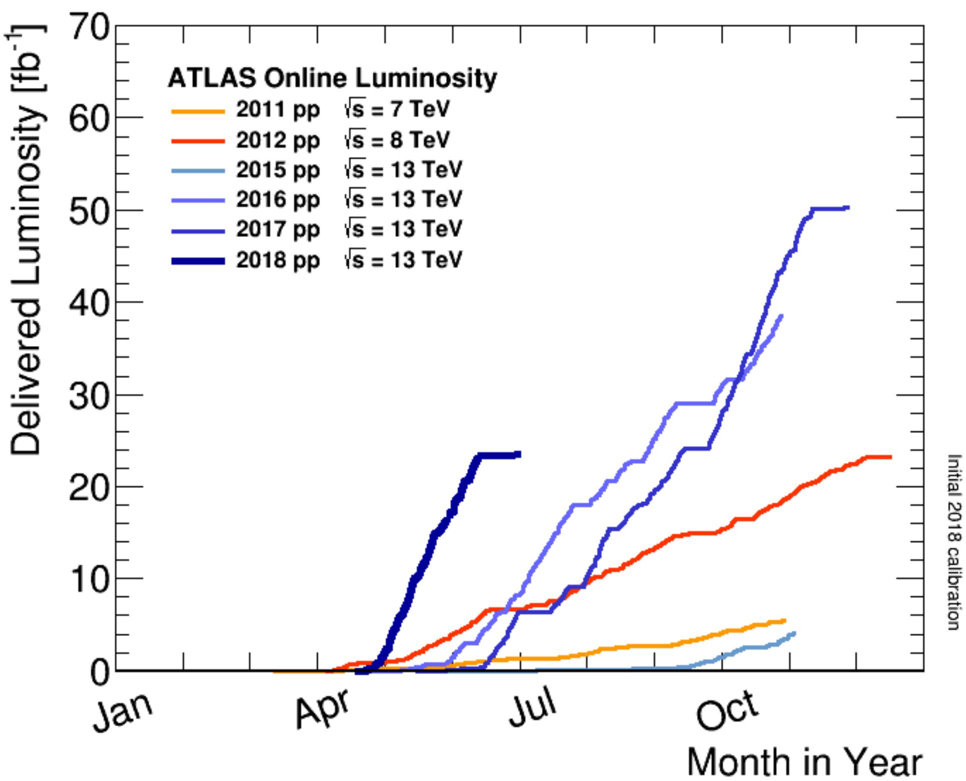

Figure 4.1: Cumulative luminosity delivered by the LHC over time for each of the years from 2011 to 2018.

Layout

The LHC was built inside an already existing tunnel, which was originally built to house a previous experiment called the Large Electron-Positron Collider (LEP). The tunnel is roughly circular and 27 km in circumference. It is buried at an average depth of 100 m below ground, sloping at a gradient of 1.4% from its deepest point of 175 m to its shallowest at 50m below ground.

The ring consists of eight arcs and eight straight regions. The straight regions are referred to as insertions, and the arcs are called sectors. The arcs contain dipole magnets which generate the field needed to bend the beams around the ring. The straight regions are known as insertions. Four of the insertions are used for particle collisions, where the two beams are focused with quadrupole magnets in order to collide the greatest number of particles in the smallest possible space. Each of the four main detector experiments are located at one of these insertions. The other four insertions are used for beam injection, cleaning, and dumping. Figure 4.2 shows a schematic of the layout of the LHC, including locations of the four major detector experiments.

In figure 4.2, the ring is divided into eight octants. Octants span from the halfway point of one arc to the halfway point of the next arc, and contain exactly one insertion.

Magnets

Dipoles

Each of the eight sectors uses 154 dipole magnets to bend the beams around the ring. All dipole magnets in a sector are connected in series and cooled in the same continuous crystotat. Each sector is powered independently. The magnetic field generated by these magnets points in the y-direction in order to generate a force that points towards the center of the LHC, according to the Lorentz force law $\vec{F} = q\left(\vec{E} + \vec{v} \times \vec{B}\right)$.

The maximum beam energy that can be kept in orbit is proportional to the strength of the magnetic field generated by the dipole magnets. So the design and performance of the dipole magnets is crucial achieving high energies needed by the LHC physics goals.

The dipole magnets are superconducting electromagnets, which generate a field of 8.3 T. The superconducting wires are made of NbTi, which has a critical temperature of 10 K, but are cooled to and operated at 1.9 K. Cooling is done with superfluid helium, which has a very high heat capacity at this temperature. The wires are made of 7 μm filaments, thousands of which are twisted together into 15 mm strands. Each cable is then composed of 36 of these strands twisted together. In order to generate the 8.3 T magnetic field, a current of 11.85 kA passes through the superconducting wires.

Each dipole magnet is 15 m long and weighs 35 t. A schematic of the cross-section of an LHC dipole magnet can be seen in figure 4.3.

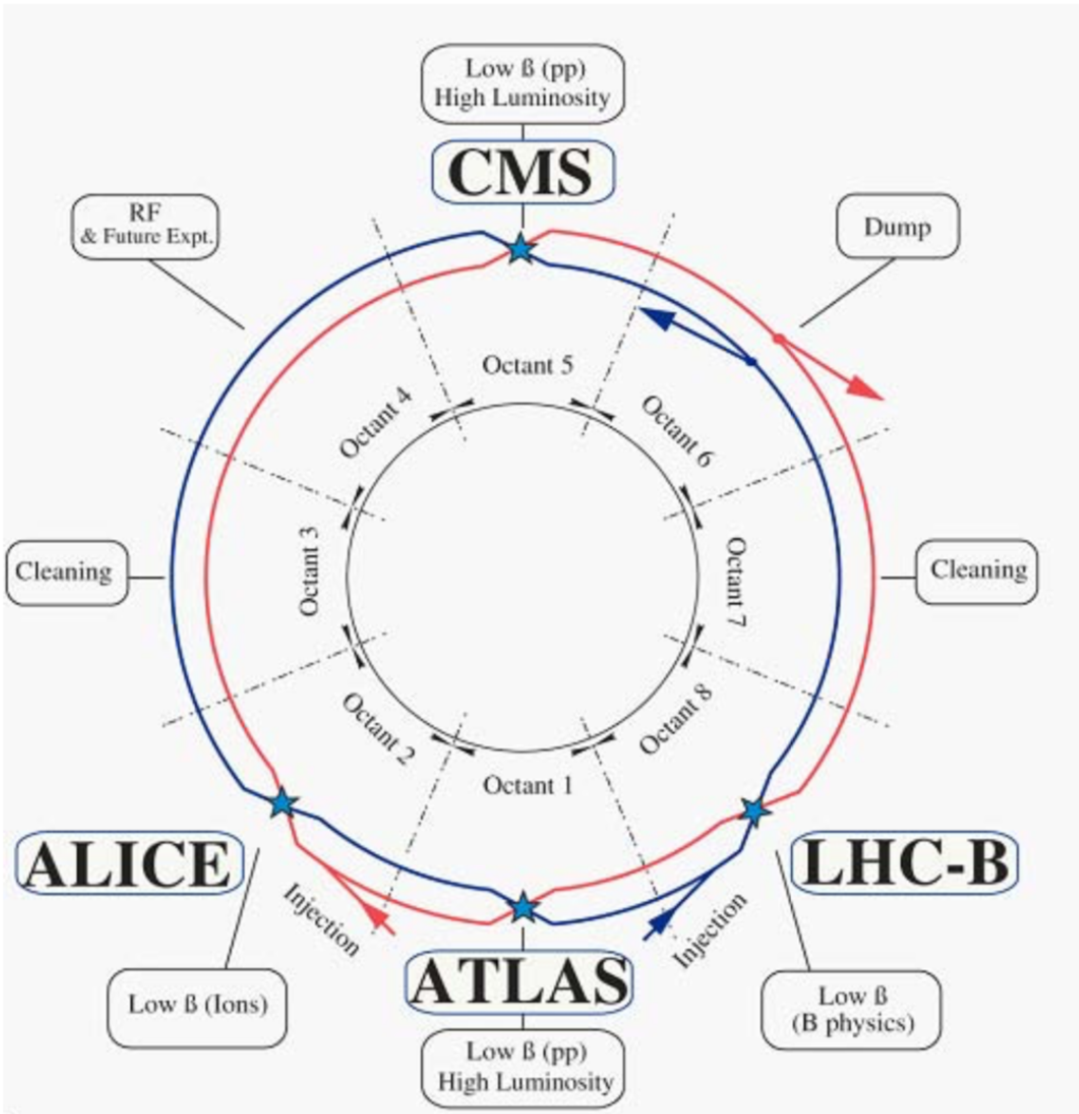

Figure 4.2: Schematic of the LHC layout. The clockwise-rotating beam, shown in red, is referred to as beam 1, and the counter-clockwise-rotating beam, shown in blue, is beam 2. Locations of the four major detector experiments are labelled.

[21]

Quadrupoles and higher order

Quadrupole magnets are located near the interaction points of each detector experiment, for focusing the beams into the smallest possible area before collisions. When a beam passes through a quadrupole magnet, it is squeezed along one axis perpendicular to the direction of travel of the beam. It is simultaneously un-squeezed in the direction perpendicular to

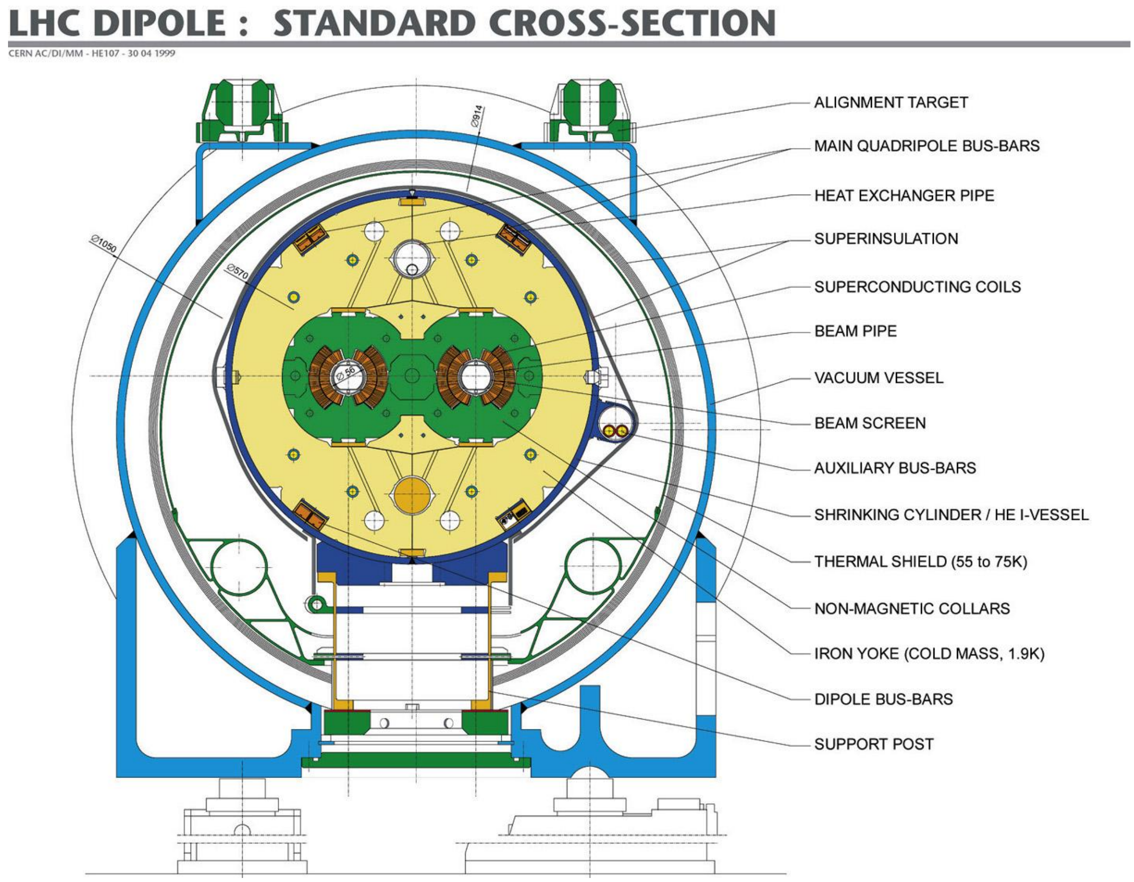

Figure 4.3: Cross-section schematic of an LHC dipole magnet.

[41]

both the beam and the squeezing direction, but the magnitude of the un-squeezing is less than the magnitude of squeezing. When a beam passes through two successive quadrupole magnets with squeezing directions at 90 degrees to each other, the net effect is a uniform squeezing of the beam towards its center. Before entering ATLAS, a series of quadrupole magnets squeezes the beams from approximately 0.2 mm to less than 20 μm.

Additional higher-order magnets are used in locations around the LHC for beam corrections and damping of oscillations. There are also special single-bore dipoles which are used to separate the beams in the region of the RF cavities, so that separate RF cavities can be used for each beam.

Radio frequency cavities

Superconducting radio frequency (RF) cavities, operating at 400 MHz, and 2 MV, are used to accelerate and store the beams. The RF cavities accelerate the beams to their nominal energy, and continue to supply power over the lifetime of the beams to compensate for energy lost through synchrotron radiation. There are a total of 16 RF cavities, contained within 4 cryomodules. Figure 4.4 is a schematic of an RF cavity cryomodule.

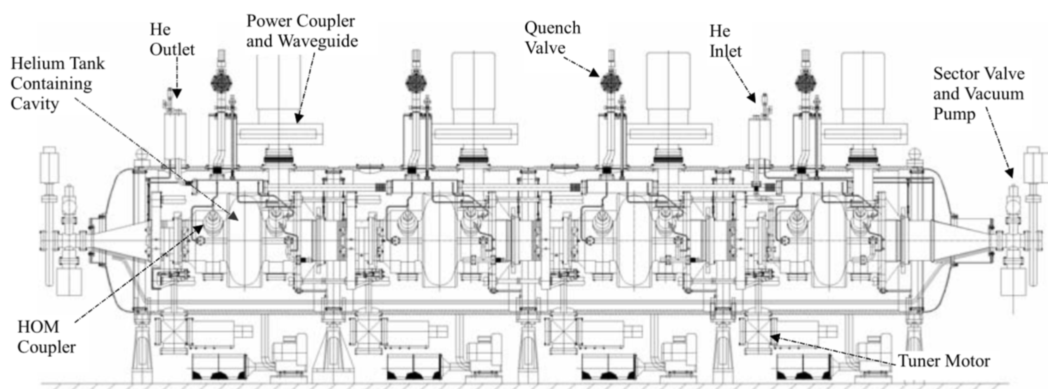

Figure 4.4: Schematic of a cryomodule, containing four RF cavities used to accelerate and store the LHC beam.

[21]

The RF cavities are tuned such that the resonant frequency of electromagnetic waves inside the cavity is 400 MHz. Protons passing through the cavity will be accelerated or decelerated by the electromagnetic field, depending on their time of arrival in the cavity. A proton travelling with the exactly the right energy will enter the cavity with just the right timing to experience zero overall force. Protons travelling slightly too slowly or too quickly will be decelerated or accelerated until their energy is exactly right. This process results in protons bunching up around the beam, with all protons traveling at the same 13 TeV energy.

Beams and luminosity

Each beam consists of 2,808 bunches of 10^{11} protons each. The frequency of cycles around the LHC is $11,245$ Hz. Bunches are mostly evenly spaced, with a few gaps that are needed for beam injection or dumping. Except for the gaps, bunches are spread out to arrive at the collision points every 25 ns. When the gaps are taken into account, actual bunches cross with an average frequency of 30 MHz. For a given bunch crossing, an average of 40 proton-proton collisions will occur. Thus the average number of events delivered to ATLAS per second is approximately 1 billion.[29]

Instantaneous luminosity is defined as:

$$\mathcal{L} = \frac{1}{\sigma}\frac{dN}{dt} \tag{4.1}$$

Where σ is the physics process under consideration, N is the number of events of that type, and t is time. Because luminosity is independent of the physics process being considered, it is a characteristic only of the LHC machine. Luminosity is therefore a useful metric for characterizing the performance of the LHC .

Luminosity is proportional to the square of the number of particles per bunch. It's also proportional to the number of bunches in each beam, and the frequency of revolution around the accelerator, according to the equation 4.2.

$$\mathcal{L} = \frac{N_b^2 n_b f_{rev}}{2\pi \Sigma_x \Sigma_y} \tag{4.2}$$

This is why it is most important to maximimize the number of particles per bunch when maximizing luminosity.

In equation 4.2, N_b is the number of particles per bunch, n_b is the number of bunches per beam, f_{rev} is the frequency of revolutions around the LHC, and Σ_x, Σ_y are the transverse widths of the beam in the x and y direction.

In order to increase luminosity, it is also therefore important to squeeze the beams as much as possible before collisions. This equation determines how to maximize instantaneous luminosity: put as many protons as possible into as small a space as possible, and accelerate them as fast as possible.

The peak luminosity delivered to ATLAS by the LHC is $10^{34} cm^{-2} s^{-1}$ for proton-proton collisions, and $10^{27} cm^{-2} s^{-1}$ for Pb-Pb collisions.

4.2 Coordinates

The coordinate system used in this document is the standard ATLAS coordinate system, detailed here. For both Cartesian and polar coordinates, the origin is defined as the nominal interaction point. The z-axis points down the beamline. The x-y plane is perpendicular to the beamline. The positive y-direction points up, and the positive x-direction points towards the center of the LHC ring. The positive z-direction therefore points counterclockwise along the LHC, when viewed from above, as required by a right-handed coordinate system.

For cylindrical coordinates, the z-axis is defined the same way as for Cartesian coordinates. The azimuthal angle ϕ is the angle from the positive x-axis, while the polar angle θ is the angle from the beamline.

A more convenient measure of angle from the beamline is the *rapidity*, because rapidity differences are invariant under Lorentz boosts in the z-direction. Rapidity is defined as:

$$y = \frac{1}{2} \ln \frac{E + p_z}{E - p_z} \tag{4.3}$$

Another frequently used quantity is the *pseudorapidity*, which is defined as:

$$\eta = -\ln \frac{\theta}{2} \tag{4.4}$$

Pseudorapidity differences are also invariant with respect to longitudinal Lorentz boosts. In the limit where $p_T \ll m$, rapidity and pseudorapidity are equal.

Pseudorapidity ranges from zero to plus or minus infinity. The x-y plane, which is perpendicular to the beamline, is described by a pseudorapidity $\eta = 0$. The z-axis, which is parallel to the beamline, is described by pseudorapidity $\eta = \pm\infty$

Finally, a distance measure in $\eta - \phi$ space is often used, especially when describing jets. This distance, ΔR is defined as:

$$\Delta R = \sqrt{\Delta\eta^2 + \Delta\phi^2} \tag{4.5}$$

4.3 Magnet Systems

The two ATLAS magnet systems are used to curve the tracks of charged particles passing through the detector, so that their momenta can be measured.

The layout of the magnet systems can be seen in figure 4.5.

The first magnetic field is produced by the central solenoid, which surrounds the entire inner detector, and is surrounded by the barrel calorimeters. It generates a uniform 2 T axial magnetic field in the inner detector. The coils are made of Al-stabilized NbTi. The length is 5.8 m, and the outer diameter is 2.56 m[16].

The second magnet system, used to bend the trajectories of muons passing through the muon spectrometer, has a more complicated geometry. It consists of a barrel toroid section, and two symmetrical end-cap toroids. The exact shape of the resulting magnetic field is quite complex, but roughly runs in a circular direction around the calorimeters.

The axial length of the barrel toroid is 25.3 m, and the outer diameter measures 20.1 m. The average field strength is 0.5 T and the superconducting material used is similar to that used in the central solenoid[16]. The magnetic field in the region $|\eta| < 1.4$ is dominated by the barrel toroid, while the end-cap field dominates the region $1.6 < |\eta| < 2.7$. The region $1.4 < |\eta| < 1.6$ is the transition region, where both sources contribute significantly to the magnetic field.

Figure 4.6 shows an end-on view of the barrel toroid, after installation, and before the calorimeters are inserted.

The end-cap toroids are used to generate the magnetic field for muons passing through the end-cap region of the muon spectrometer. The properties and geometry of the end-cap toroids are similar to the barrel toroid, with peak magnetic field reaching 4.1 T[16].

4.4 Inner Detector

The inner detector consists of silicon pixel detectors, silicon strip detectors, and transition radiation trackers. It covers a region from $R = 33$ mm to $R = 1082$ mm and $|\eta| = 0$ to $|\eta| = 2.5$. The entire inner detector is immersed in a 2 T magnetic field, generated by a

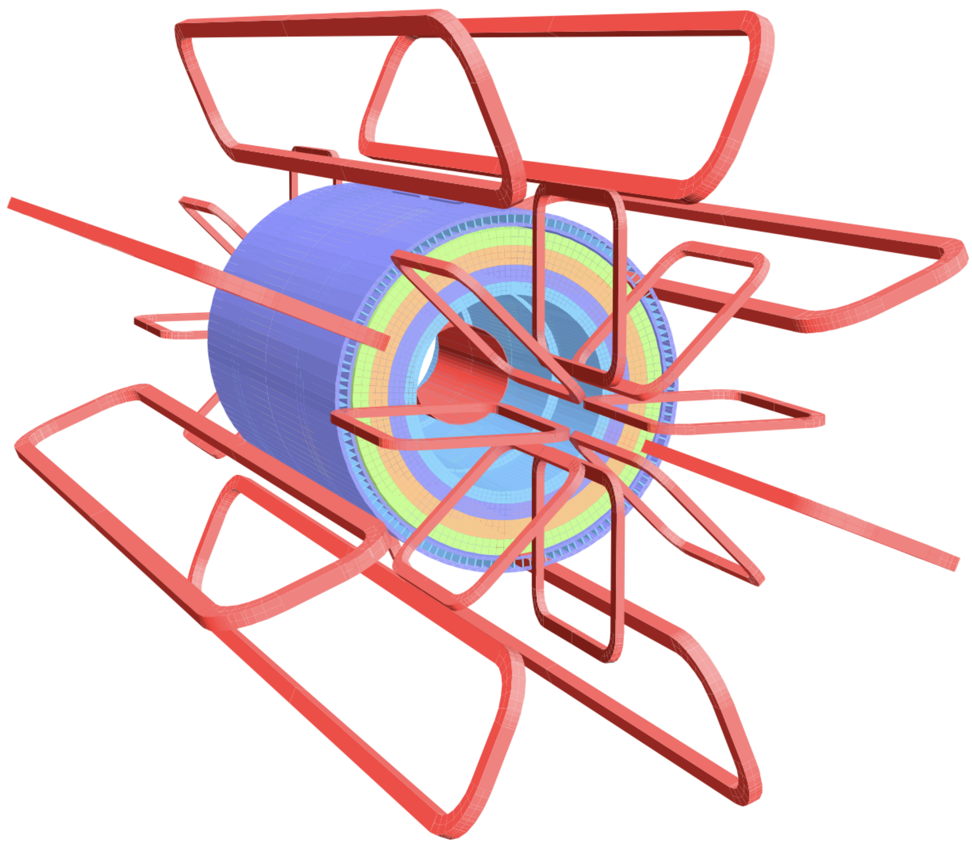

Figure 4.5: A diagram showing the layout of the ATLAS magnet system. The central solenoid is used to apply a force that curves the trajectories of charged particles in the inner detector. In red are the toroid coils, used to bend the tracks of charged particles passing through the muon spectrometer.

solenoid coil which surrounds it.[16] The layout of inner detector subsystems is shown in figure 4.7.

Pixel Detector

The innermost layer of ATLAS detectors is the pixel system. Since it lies closest to the interaction point, the pixel system experiences the highest flux of any ATLAS subdetector. This means that the pixel detector must have the greatest radiation hardness, greatest resolution, and greatest occupancy of any subdetector.[16] The pixel system consists of 1744 solid-state pixel sensors, arranged into a barrel region and two endcap regions. In total, there are 80.4 million pixel readout channels.[16]

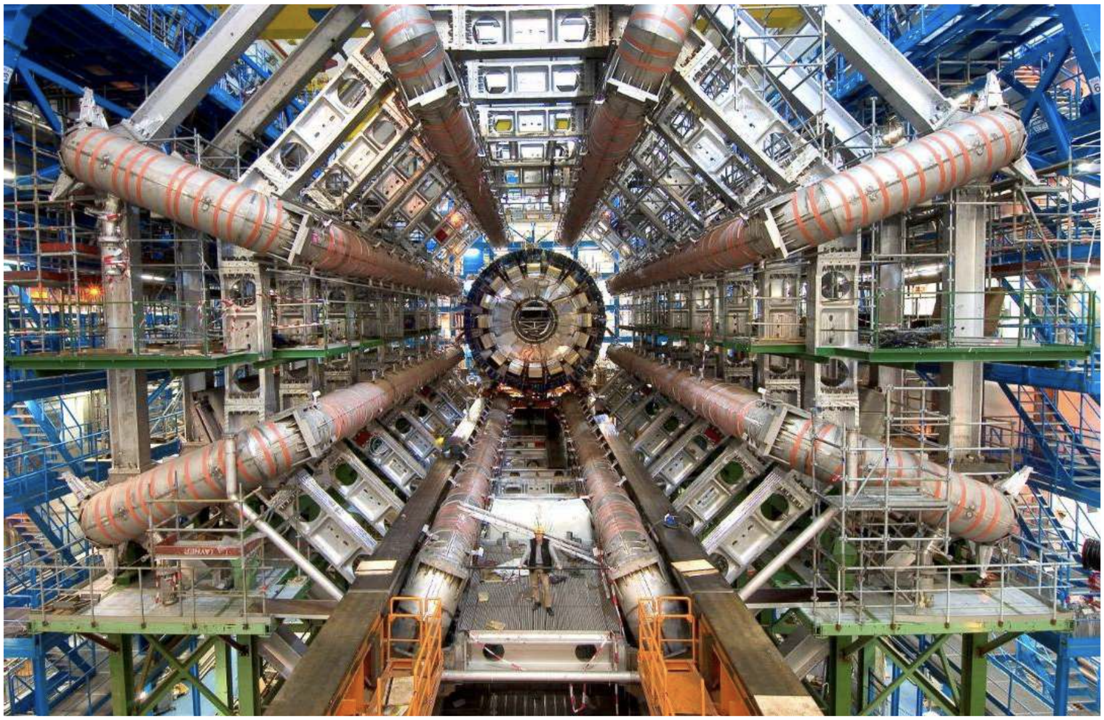

Figure 4.6: A picture of the ATLAS barrel toroid after installation. In the center of the image is the calorimeter and central solenoid, before being moved into the final position.

Layout

The barrel region consists of four concentric cylindrical layers, coaxial with the beamline. The two endcap regions are each made up of three disks, arranged perpendicular to the beamline.

The pixel barrel envelope covers a region from $z = 0$ to $|z| = 400.5\ mm$. The four layers are located at increasing distances from the beamline, at $R = 33\ mm, 50.5\ mm, 88.5\ mm, 122.5\ mm$.

The six endcap disks are located at $|z| = 495\ mm, 580\ mm, 650\ mm$ and cover the region $88.8\ mm < R < 149.6\ mm$.[16]

Figure 4.7 shows a quarter-section of the entire inner detector, as well as a detailed view of the pixel subsystem, not including the Insertable B Layer (IBL), which was installed in 2014.

Sensors

The ATLAS pixel sensors are solid-state silicon detectors. The basic operating principle of a solid-state detector is that charged particles passing through the material generate electron-hole pairs, which are accelerated towards opposite ends of the material via an electric field.

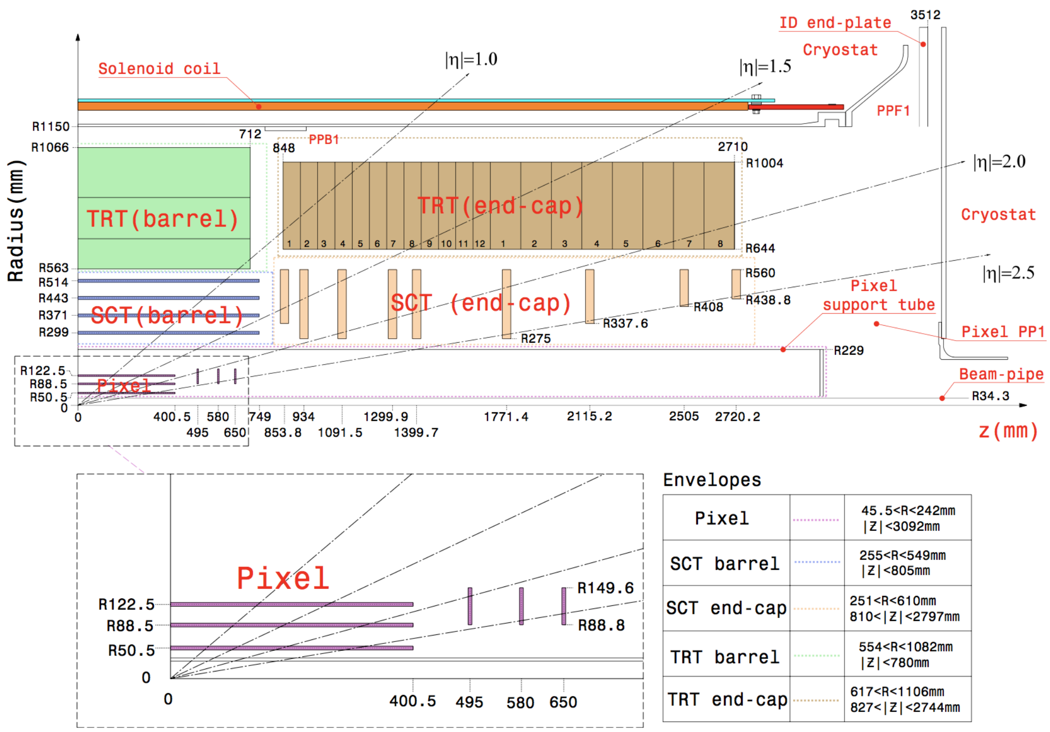

Figure 4.7: A quarter-section plan showing the layout of inner detector susbystems and their dimensions. Not shown is the innermost layer of the pixel detector, the IBL, which was installed in May 2014.

This generates a current, which can be measured by charge-sensitive sensors at the edge of the material.[40]

In a silicon detector, the active material is a pn junction, operated with a reverse bias voltage, until fully depleted. This reduces the thermal noise from free charge carriers to a low enough level that electron-hole pairs from signal particles can be detected.[40]

In ATLAS, the pixel sensors consist of an n-type bulk, with p^+ implants on the back side and n^+ implants on the front side. Before irradiation, the active pn junction region exists between the n-type bulk and p^+- implanted side. Irradiation leads to the reduction in the effective doping concentration, until the bulk material undergoes type inversion. After type inversion, the active pn junction region switches to the n^+-doped side.[12] This process is illustrated in figure 4.8.

This n^+-in-n design allows the sensors to continue to operate both before and after large doses of radiation.

Each pixel tile has 47232 pixels, laid out in a grid of 144 columns by 328 rows. Some of the pixels are grouped to common read-out channels, resulting in 46080 read-out channels. This grouping is done so that an equal number of read-out channels can be connected to each of the 16 front-end read-out chips.[12]

In 128 of the columns, each pixel implant is $382.5 \times 30\ \mu m^2$, with pitch (center-to-center distance) of $400 \times 50\ \mu m^2$. In the remaining 16 columns, the pixel sizes are $582.5 \times 30\ \mu m^2$, with a pitch of $600 \times 50\ \mu m^2$.[12]

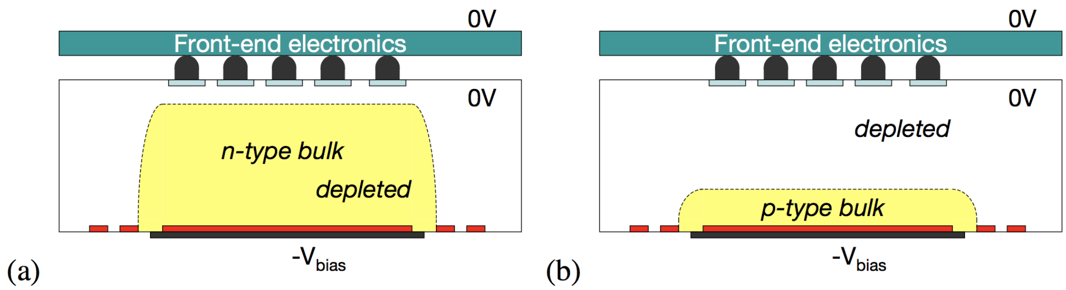

Figure 4.8: Graphic illustrating how n^+-in-n pixel sensors continue to operate after the type inversion that results from irradiation. In (a), the unirradiated state, the bulk is n-type, and the depletion zone occurs between the p^+-doped back side. After type inversion, in (b), the depletion zone occurs between the now p-type bulk and the n^+-doped front side. [12]

The IBL

A major upgrade that occurred during the long shutdown in 2014 was to install the Insertable B-Layer (IBL) to the pixel detector. The IBL became the fourth and innermost layer of the pixel detector. The IBL provides several key improvements to the tracking system, which will allow the pixel detector to maintain good performance even in the higher-luminosity environment that will be present in the High Luminosity LHC (HL-LHC).[11] The IBL does this by improving tracking robustness against module failures, adding measurement redundancy to mitigate the effects of pileup, and adding an additional measurement closer to the interaction point.[11]

As part of the IBL insertion project, the original beam pipe was removed, and replaced with a smaller-radius beampipe. Precision tooling and methods for insertion were developed and practiced for two years before the procedure was finally carried out. The tolerances were extremely tight, with only a 0.2 mm gap between the IBL and inner supporting tube.[10]. An image of the IBL being inserted can be seen in figure 4.9

Silcon Strip Tracker

After the pixel detector system, the next innermost subdetector is the SemiConductor Tracker, or SCT . The SCT consists of 4088 modules, with a total silicon surface area of 63 m^2.[16] The SCT sensors are silicon strips rather than pixels. In order to obtain two-dimensional resolution, SCT modules are paired back-to-back at a small stereo angle.

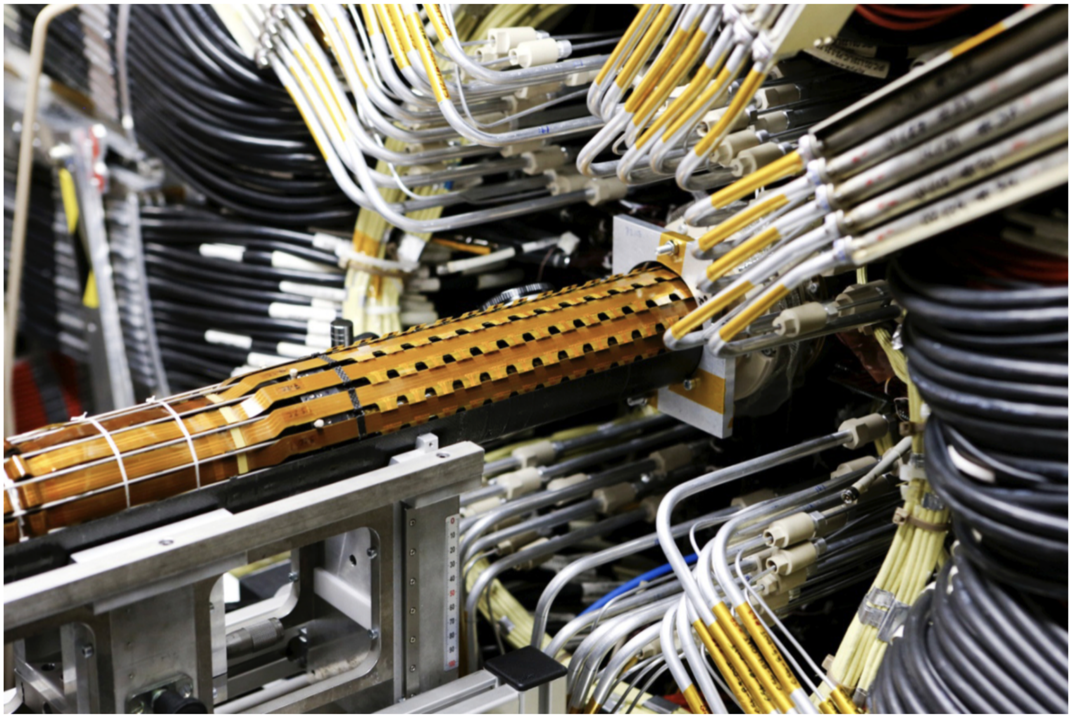

Figure 4.9: The IBL as it was inserted into the pixel detector

[10]

Layout

Like the pixel system, the SCT barrel region consists of four concentric cylindrical layers, coaxial with the beamline. The two endcap regions are each made up of nine disks, arranged perpendicular to the beamline.

The SCT barrel envelope covers a region from $z = 0$ to $|z| = 746\ mm$, and the four layers are located at increasing distances from the beamline, at $R = 299\ mm, 371\ mm, 443\ mm, 514\ mm$.[18]

The nine endcap disks on each side range from $|z| =\ \ mm$ to $|z| =\ \ mm$, and cover the region $275\ mm < R < 560\ mm$.[16]

The modules are arranged in back-to-back pairs at a stereo angle of 40 $mrad$, in order to provide two-dimensional resolution.

Modules

Like in the pixel system, the SCT sensors are solid-state silicon detectors. Instead of pixels, the base unit is a strip of silicon, ranging in length from 6 to 13 cm. These strips are made of p-type silicon, and are embedded in n-type silicon. The average pitch is 80 μm.[23]

The resolution resulting from this design is 17 μm in the $r-\phi$ direction, and 580 μm in the z-direction.[23]

Transition Radiation Tracker

Moving outwards from the pixel system and SCT, the final inner detector subsystem is the transition radiation tracker, or TRT . Unlike the pixel or SCT systems, the TRT uses proportional drift tubes, referred to as straws, as sensors.

To make accurate track measurements, the TRT relies on a larger number of hits over a longer distance than the pixel system or SCT . Since the TRT measures approximately 36 hits per track, and makes measurements over a longer distance, less spatial precision is required per hit.[16]

The TRT only provides tracking information in the $R-\phi$ direction, unlike the pixel and SCT systems, which each provide three-dimensional tracking information.

The main purpose of the TRT is to provide additional tracking information. But transition radiation photons generated in the TRT gas-filled tubes can also aid in electron identification.[16]

Operating Principle

The TRT uses proportional drift tubes to detect charged particles. A tube is filled with a mixture of two or more gases, including an inert gas such as Xenon. And an electric field is applied across the tube. When a charged particle passes through the tube, ion pairs are generated from the inert gas. Positive and negative ions drift in opposite directions, towards the cathode and anode, respectively. If a particle's energy is completely absorbed in the tube, the number of ions produced in stopping the particle is proportional to the original energy of the particle.[28]

In addition to the inert gas, it is common to add another gas, such as Carbon Dioxide, to stabilize the ionization process. This additional gas is referred to as a quencher gas.

Layout

Like the pixel system and SCT systems, the TRT consists of a barrel region and two end-cap regions. In the barrel region, straw tubes are arranged coaxial to the beamline and measure 144 cm in length. In the end-cap region, straw tubes are arranged radially, and measure 37 cm in length.[16]

The TRT barrel envelope covers a region from $z = 0$ to $|z| = 780$ mm, and $554 < R1082$ mm, and the end-cap envelop covers a region from $z = 848$ to $|z| = 2710$ mm, and $644 < R1004$ mm. This provides tracking coverage out to $|\eta| = 2.0$.[16]

A charged track passing trough the TRT will typically produce 36 hits. Each straw provides a hit resolution of 130 μm. There are 351,000 total readout channels.

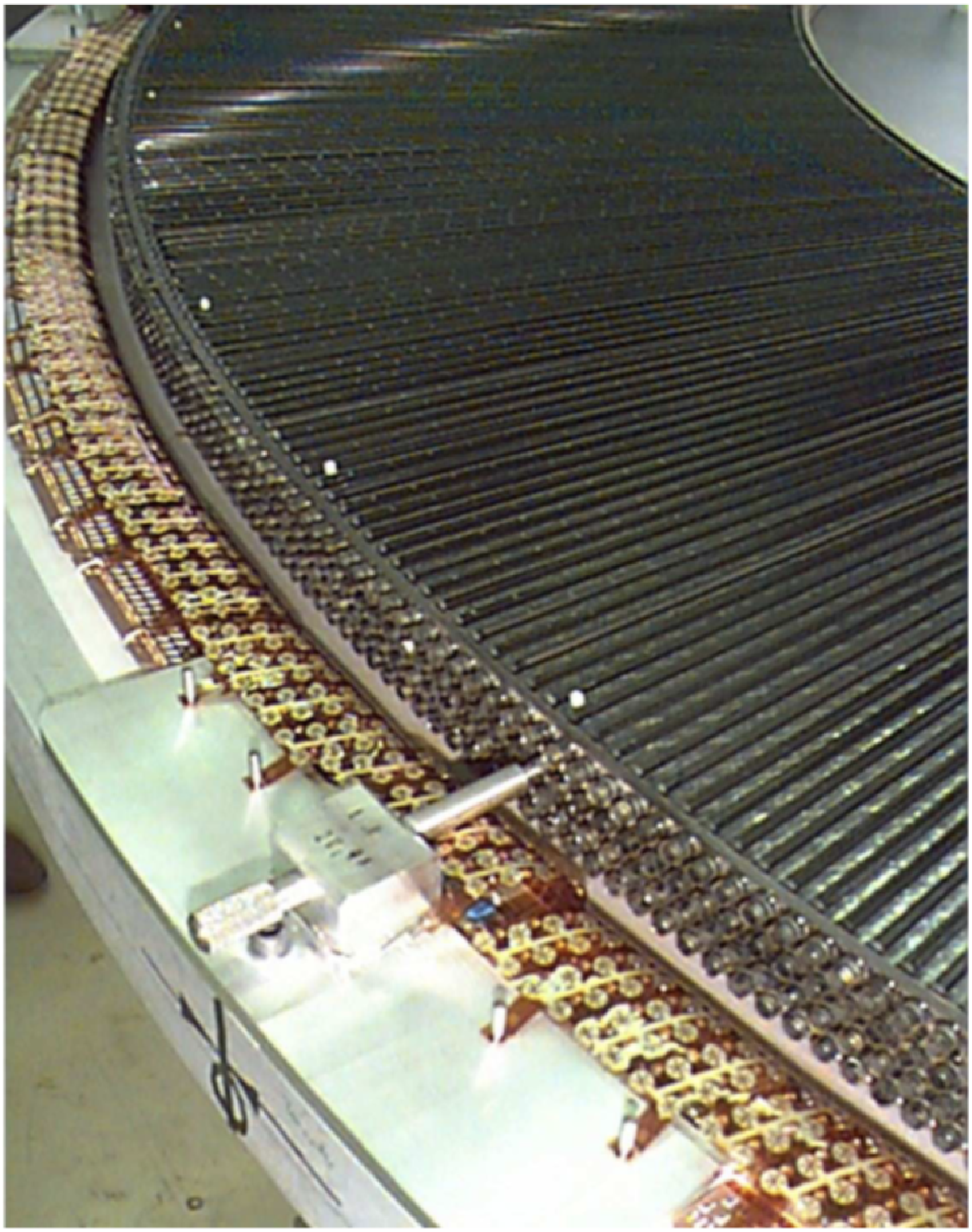

Figure 4.10: Part of a TRT end-cap, showing the radial layout of the 37 cm straw tubes. [17]

Sensors

The TRT straw tube walls are constructed of two layers of 25 μm-thick Kapton film. The Kapton is coated with a 0.2 μm-thich layer of aluminum, followed by a 6 μm-thich layer of carbon-polyimide. The Aluminum layer serves to provide electrical conductivity, and the carbon-polyimide layer is to protect the aluminum. The two Kapton layers are sealed together with a 5 μm-thick polyurethane layer.[17] The TRT straw wall design is shown in figure 4.11

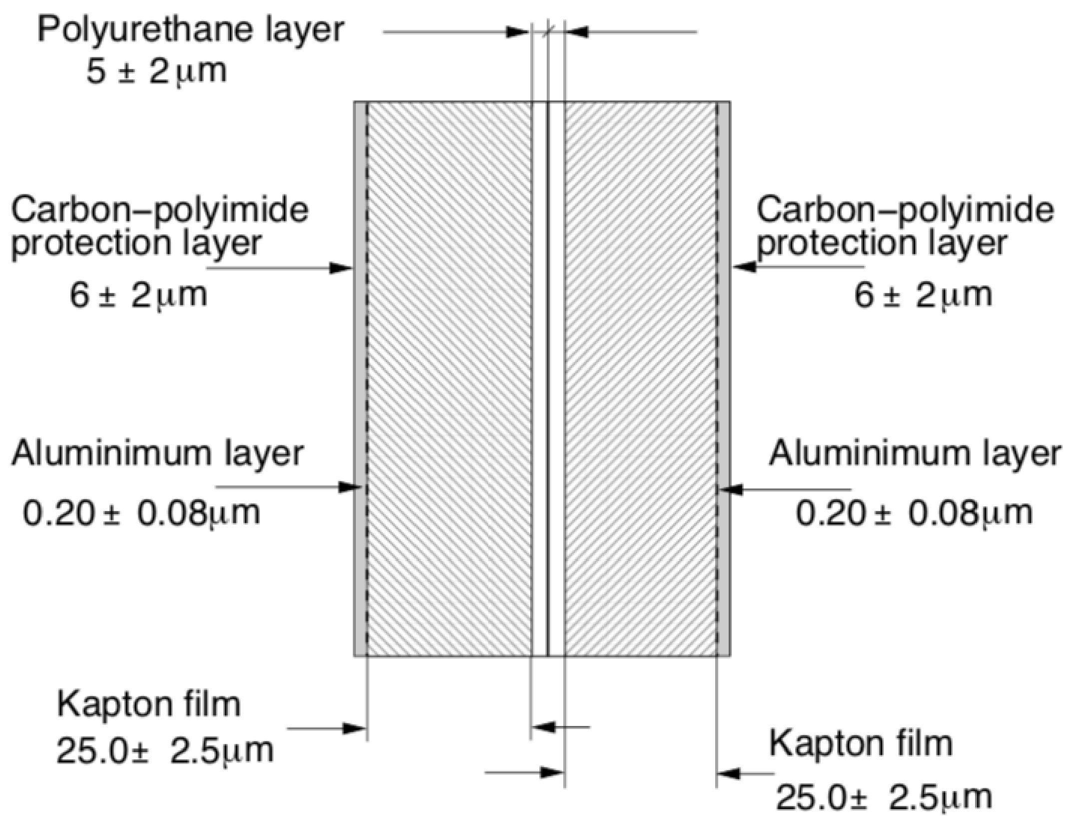

Figure 4.11: Schematic of the TRT straw wall design. Two coated Kapton layers are sealed together with polyurethane.

[17]

The straws are filled with a mixture of 70% Xe, 27% CO_2, and 3% O_2. Carbon dioxide is used as a quencher gas, which is needed to guarantee that the ionization procedure is stable. The addition of a small amount of oxygen increases the voltage difference between the working point and the breakdown voltage, further stabilizing the process.[17]

In order to maximize hit efficiency, the straw diameter should be as large as possible. But there is a tradeoff: as straw diameter increases, so does the drift time. The optimal diameter to ensure acceptable time resolution for 25 ns bunch-spacing was chosen as 4 cm.[17]

4.5 Calorimeters

The ATLAS calorimeters are designed to absorb and measure the energy of both electromagnetic and hadronic showers. Different materials and geometries are used for different calorimeter subsystems, but the operating principle is the same. In each calorimeter, there is an absorber medium, and a sampling medium. When a particle strikes the absorber medium, it triggers a shower of particles which then pass into the sampling medium. The sampling medium is ionized by these showering particles, and instrumentation is used to measure the amount of ionization. In order to accurately measure shower energy, the ATLAS calorimeters are designed to fully absorb both electromagnetic and hadronic showers.

The innermost calorimeter is a high-granularity detector optimized for measuring electromagnetic showers. Lead is used as an absorber and LAr as the sampling medium. It covers the range $|\eta| < 3.2$.

The outer calorimeter has a coarser granularity and is optimized for measuring jets and E_{Tmiss} . It consists of scintillator tiles and uses steel as the absorber.

In addition to the EM and hadronic calorimeters, there is copper-tungsten/LAr calorimeter providing coverage out to $|\eta| < 4.9$. This is known as the forward calorimeter, or FCal.

The layout of the ATLAS calorimeter system can be seen in figure 4.12

Electromagnetic Calorimeters

The electromagnetic calorimeter is located just outside the solenoid that surrounds the inner detector. It is optimized for measuring the energy of electromagnetic showers. The EM calorimeter is also designed to measure the direction of neutral particles, which cannot be tracked by the inner detector.

In the barrel region, the EM calorimeter covers the range $|\eta| < 1.475$. In the end-cap region, it covers a range of $1.375 < |eta| < 3.2$.

The calorimeters have to be thick enough to fully absorb shower energy and to minimize punch-through into the muon system. The EM calorimeter depth was designed to be 22 interaction lengths (X_0) in the barrel, and 24 X_0 in the end-caps. An interaction length is defined as the average distance traveled by a particle through a material when it has lost $1 - 1/\mathrm{e}$ of its original energy.[34]

The calorimeters consist of accordion-shaped lead absorber plates with copper-kapton electrodes in between. The accordion shape provides full symmetry in $|\phi|$ with no gaps. The absorber plates are grounded and the electrodes are kept at 2000 V in the barrel region and between 1000 and 2500 V in the end-cap region. The whole system is immersed in liquid argon.[16]

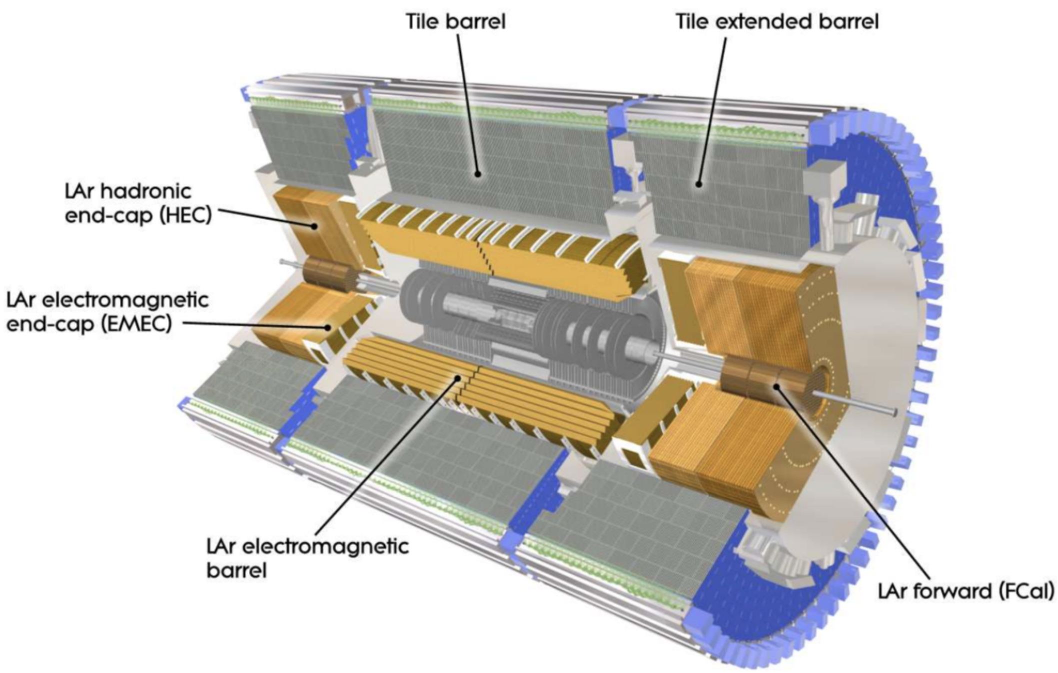

Figure 4.12: Layout of the ATLAS calorimeter system.

[16]

A particle passing through the lead absorbers generates a shower of particles, which ionize the LAr. Due to the electric field between the absorber plates and electrodes, ions drift towards the electrodes. This generates a pulse in the electrodes which can then be recorded.

The calorimeter cells are arranged into three layers, with highest granularity closest to the interaction point. Cells in layer 1 have a granularity of $\delta\phi \times \delta\eta = 0.0245 \times 0.0031$. This very fine segmentation is useful in accurately determining the direction of incoming particles. It is also useful in discriminating between an individual photons and a neutral π meson decaying to two photons.[34]

In the second layer, the granularity is reduced $\delta\phi \times \delta\eta = 0.0245 \times 0.025$.

In the third and final layer, the granularity is further reduced to $\delta\phi \times \delta\eta = 0.0245 \times 0.05$.

The geometry of the EM calorimeter cells can be seen in figure 4.13

Inside the innermost layer of the barrel EM calorimeter is an 11 mm-thin presampler, covering a range of $|\eta| < 1.8$. The purpose of this presampler is to correct for energy lost to material upstream of the EM calorimeter.

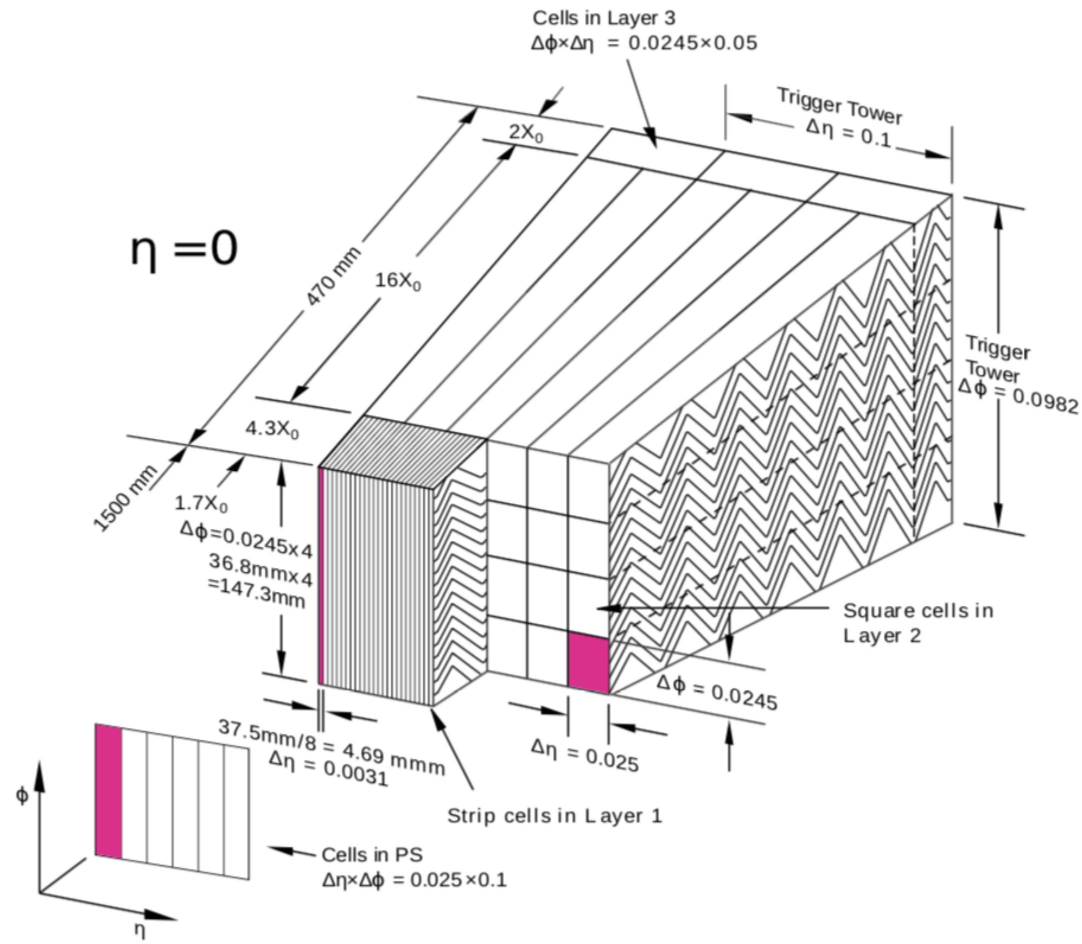

Figure 4.13: Schematic of EM calorimeter, showing the granularity of each layer.

[34]

Hadronic Calorimeters

The most important ATLAS subdetector for measuring jets is the hadronic calorimeter system.

The hadronic calorimeter system consists of central and extended tile calorimeter barrels, two end cap calorimeters, and a forward calorimeter.

Tile calorimeters

The central tile barrel covers the range $|\eta| < 1.0$, the extended tile barrels cover the range $0.8 < |\eta| < 1.7$, and the end-cap calorimeters cover the range $1.5 < |\eta| < 3.2$. The forward calorimeters (FCal) cover the extreme forward region, $3.1 < |\eta| < 4.9$.

The central barrel is 5.8 m long, and the extended barrels are each 2.6 m long. Both the central and extended barrels cover the range 2.28 $m < R < 4.25$ m. Each of the three tile calorimeters is composed of 64 wedge-shaped modules. The geometry of the hadronic calorimeter system, not including the end-caps, can be seen in figure 4.12.

The hadronic calorimeters in the central and extended barrel regions are tile calorimeters. They consist of alternating steel absorber plates and scintillating tiles. Particles that pass through the steel plates generate hadronic showers. The hadrons from these showers then stimulate the production of photons in the scintillating tiles. Those photons are then collected by photomultiplier tubes, producing a current that can be measured. A wavelength-shifting fiber is used to convert the ultraviolet photons produced in the scintillator into optical photons before entering the photomultipliers.

A schematic of a tile calorimeter module can be seen in figure 4.14

The η- and depth-dependent segmentation of the tile calorimeter modules can be seen in figure 4.15

Hadronic end-cap calorimeters

The hadronic end-cap calorimeter (HEC) consists of two cylindrical wheels on each side of the barrel, each of which is 2.03 m in radius. Each of these wheels is made up of 32 modules. The HEC wheels closest and farthest from the interaction point are called HEC1 and HEC2. HEC1 modules have higher granularity and sample fraction than HEC2 modules. A schematic of the HEC modules can be seen in figure 4.16.

The HECs use LAr as the sampling material and copper as the absorber material. The copper plates are separated by gaps of 8.5 mm, with three electrodes in between. This creates four drift zones between each copper plate. Typical drift time across the drift zones is $430ns$, at a potential difference of $1800V$.[16]

There are a total of 5632 readout cells. In the region $|\eta| < 2.5$, the readout cell size is $\delta\phi \times \delta\eta = 0.1 \times 0.1$, and $\delta\phi \times \delta\eta = 0.2 \times 0.2$ elsewhere.

Forward Calorimeters

Special forward calorimeters (FCal) were designed to cover the forward region, $3.1 < |\eta| < 4.9$. This region experiences very high particle flux compared to the barrel or end-cap regions, so a different design was needed. Each FCal consists of three modules. The module closest to the interaction point (FCal1)is optimized for EM showers, while the middle and outer modules (FCal2 and FCal3) are optimized for hadronic showers. All three modules are 45 cm deep, and use LAr as the sampling material.

FCal1 uses copper as the absorber material, while FCal2 and FCal3 use tungsten as the primary absorber. To further reduce punch-through into the muon system, a copper shield plug is placed behind FCal3.

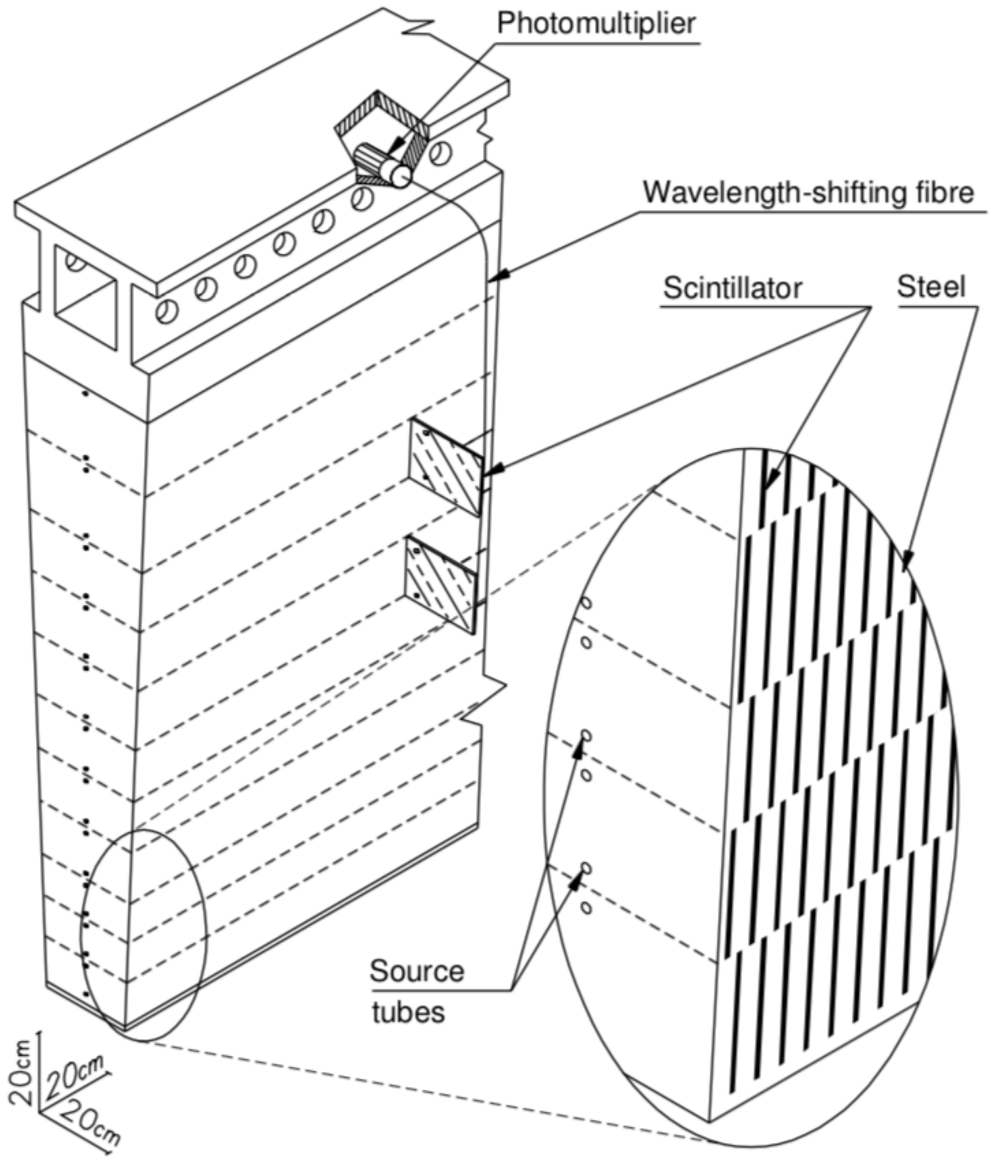

Figure 4.14: Schematic of EM calorimeter, showing the granularity of each layer.

[16]

The location of the FCal with respect to the end-cap calorimeters can be seen in figure 4.17 The FCal, hadronic end-cap, and electromagnetic end-cap calorimeters are all contained in the same end-cap cryostat.

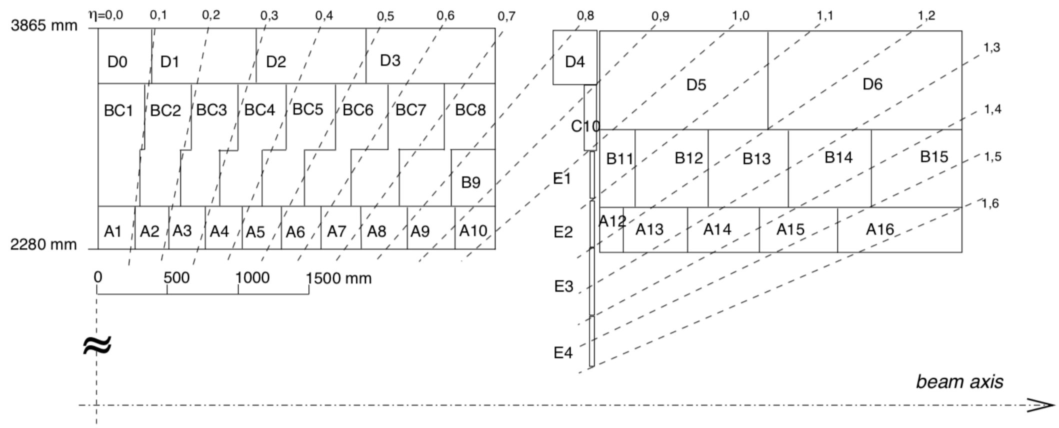

Figure 4.15: Schematic of the central (left) and extended (right) tile calorimeter, showing the η- and depth-dependent segmentation.

[16]

The overlapping design of the end-cap and forward calorimeters allows for hermetic coverage with minimal energy loss out to $|\eta| < 4.9$.

Energy absorbtion

In order to provide accurate energy measurements of photons, jets, and E_{Tmiss}, it is necessary for the calorimeters to absorb as much shower energy as possible. Any particles that don't get absorbed by the calorimeter are considered punch-through particles. These punch-through particles add noise to the muon system, and so should be minimized.

For hadronic showers, the analog to a radiation length is called an interaction length, λ . The amount of energy absorbed by each part of the calorimeter, as measured in radiation lengths, can be seen in figure 4.18.

4.6 Muon Spectrometer

The outermost ATLAS system is the muon spectrometer, used to measure the momenta of charged particles that exit the calorimeter systems. Muons are not absorbed by the EM calorimeter because they undergo less bremsstrahlung than electrons due to their high mass. They are also no absorbed by the hadronic calorimeter because they do not interact strongly. As a result, muons are the most common particle to escape the calorimeter system.

The overall dimensions of the muon spectrometer, which define the demensions of ATLAS, are 44 m long by 22 m high. The muon spectrometer consists of four subsystems. The monitored drift tubes (MDTs) and cathode strip chambers (CSCs) are used for high-precision tracking, while the resistive plate chambers (RDCs) and thin-gap chambers (TGCs) are

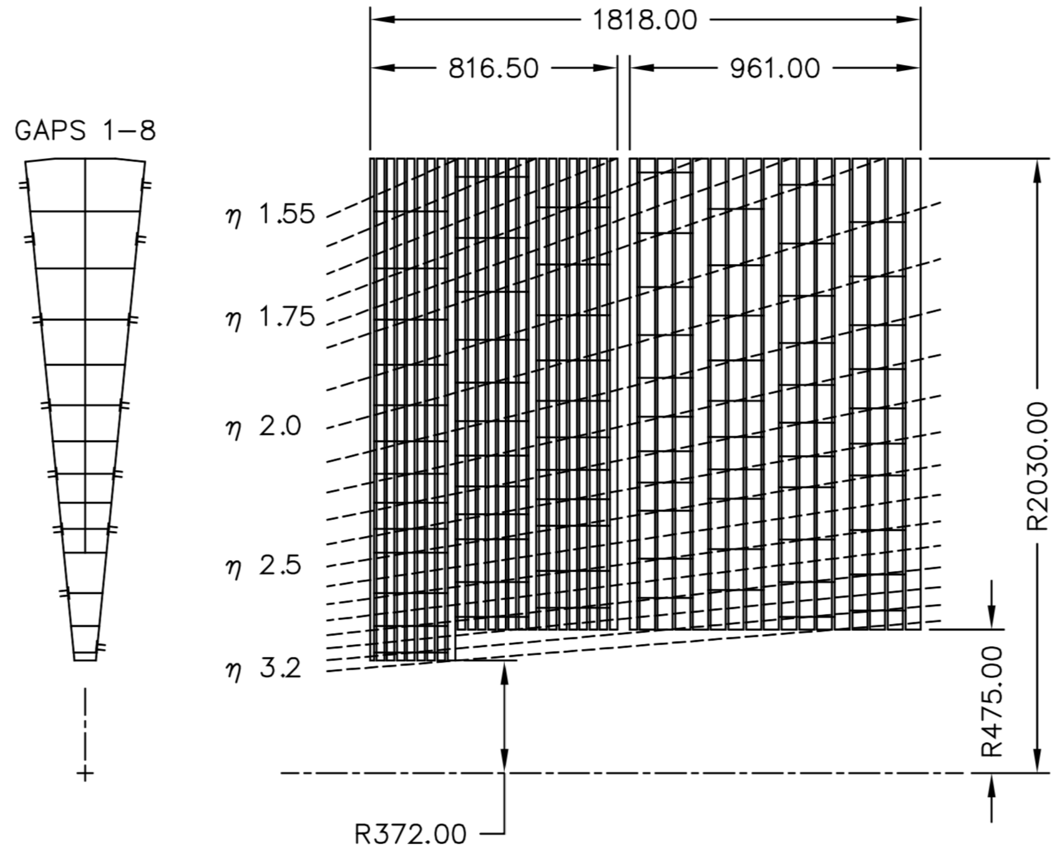

Figure 4.16: Schematic of hadronic end-cap calorimeter module

[16]

used for triggering and bunch-crossing identification. The location of each of the four muon subsystems can be seen in figure 4.19

As described in section 4.3, the magnetic field in the muon system runs in a roughly circular direction around the beamline. As a result, charged particles are bent in the η direction in the muon spectrometer.

In the barrel region, covering $|\eta| < 1.0$ the muon system is laid out in three concentric cells, located at 5 m, 7.5 m, and 10 m from the interaction point. Full coverage is provided in this region, except for a small gap at $|\eta| = 0$, to allow for services to the solenoid, calorimeters, and inner detector systems. The size of the acceptance gap is $|\eta| < 0.04$ in the innermost layer, and $|\eta| < 0.08$ in the outer layers. The end-cap consists of large wheels, located at $|z| \approx 7.4$ m, 10.8 m, 14 m, and 21.5 m. Figure 4.20 shows a cross-section of the barrel region of the muon spectrometer in the $x - y$ plane, and a cross-section of the barrel and end-cap regions in the $y - z$ plane. The small acceptance gap at $\eta = 0$ can be seen.

The muon spectrometer provides high-precision momentum measurements out to $|\eta| <$

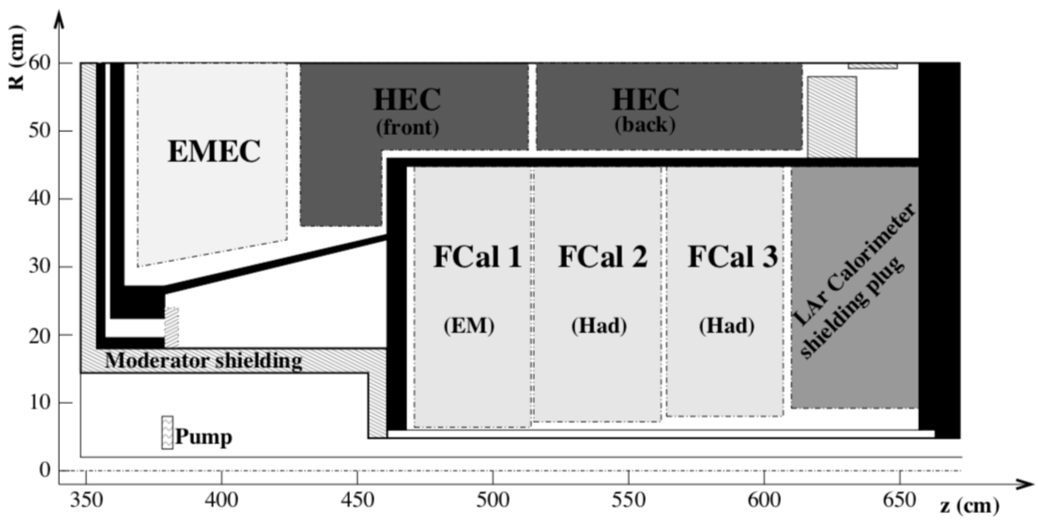

Figure 4.17: Schematic showing the layout of the forward calorimeters and end-cap calorimeters.

[16]

2.7, and triggering on high-momentum muons out to $|\eta| < 2.4$.

The ATLAS design specification requires momentum resolution of 10% for 1 TeV muons. This resolution is achieved or exceeded for the range 10 $GeV < p_T < 1$ TeV. The contribution to p_T resolution from various sources at different p_T is shown in figure 4.21. The dominant contribution at low-p_T is from energy loss fluctuations, while at high-p_T it's from wire resolution and autocalibration.[36]

Monitored drift tubes (MDTs)

Most of the precision momentum measurements in the muon spectrometer are performed by MDTs. The MDT subsystem covers the region $|\eta| < 2.7$, except for the innermost end-cap layer, where they cover out to $|\eta| = 2.0$. There are a total of 1174 MDT chambers, each made up of between 3 and 8 layers of drift tubes. The aluminum tubes are 3 cm in diameter and range between 0.9 m and 6.2 m in length. They are filled with a mixture of 80 %Ar and 20 %CO_2. The MDTs provide a resolution of 80 μm per tube, and 35 μm per chamber.

In order to provide high-precision measurements, the locations of all chambers and their support structures are constantly monitored. Temperature and magnetic field conditions are also monitored, in order to account for thermal expansion and changes to drift time.[36]

The MDTs can be safely operated at a rate of up to 150 Hz/cm^2. In the forward region of the innermost end-cap, where the background rate is highest, CSCs are used in place of MDTs.

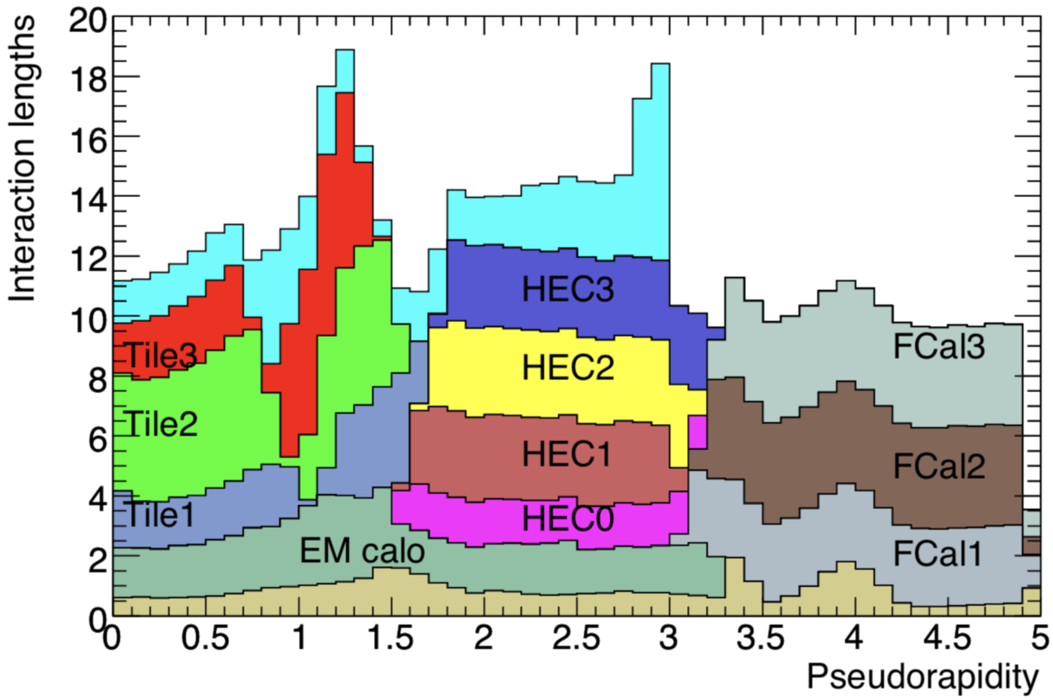

Figure 4.18: Amount of material, in units of interaction length, versus pseudorapidity, including all material before the EM calorimeter, the EM calorimeter, and the hadronic calorimeters. The light blue indicates the amount of material in front of the muon spectrometer for $|\eta| < 3.0$

[16]

Cathode strip chambers (CSCs)

In the innermost end-cap layer, covering the region $2.0 > |\eta| > 2.7$, the background rate is too high for safe operation of MDTs. Instead, precision momentum measurements are performed using cathode strip chambers, which can be safely operated at rates up to 1000 Hz/cm^2[16].

The CSC chambers use the same gas mixture as MDT chambers. Instead of drift tubes there are grids of anodes and cathodes, allowing for measurements of η and ϕ based on the charge induced in the wires.

There are a total of 32 CSC chambers, arranged into 4 disks of 8 chambers each. Each chamber contains 4 CSC layers, resulting in 4 independent measurements of η and ϕ for each track. Cathodes are made of 17 mm copper strips, and anodes are gold-plated tungsten measuring 30 mm in diameter. Sense-wire pitch is 2.54 mm, but resolution is limited by readout pitch, which is 5.08 mm. This results in an η resolution of 60 μm, and a ϕ resolution of 5 mm.[36] Since the magnetic fields bend muons in the η plane, precice momentum measurements require far greater resolution in η.

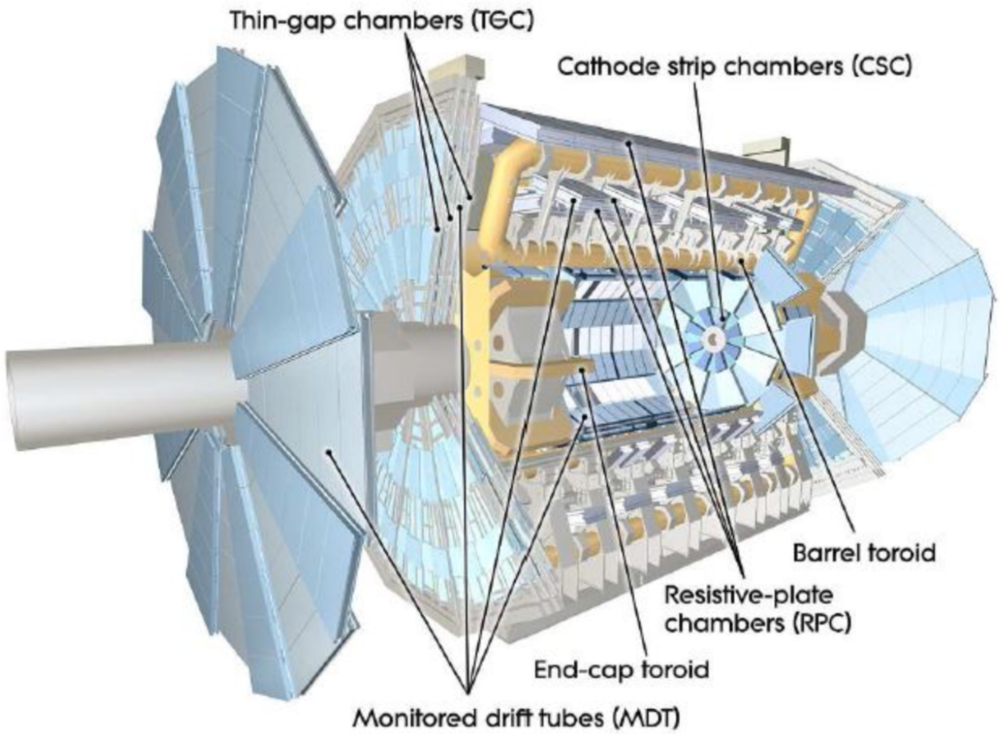

Figure 4.19: Layout of the muon spectrometer, indicating the location of barrel and end-cap toroids, along with the four subsystems.

[16]

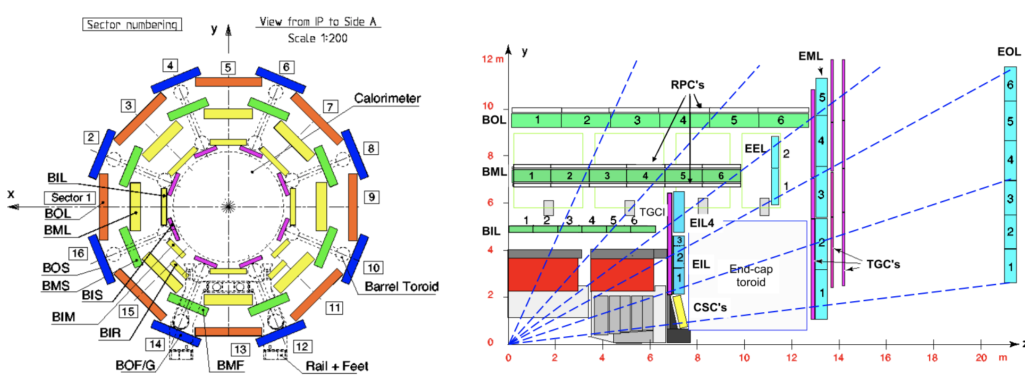

Figure 4.20: Cross-sections in $x-y$ (left) and $y-z$ (right) of the muon spectrometer.

[36]

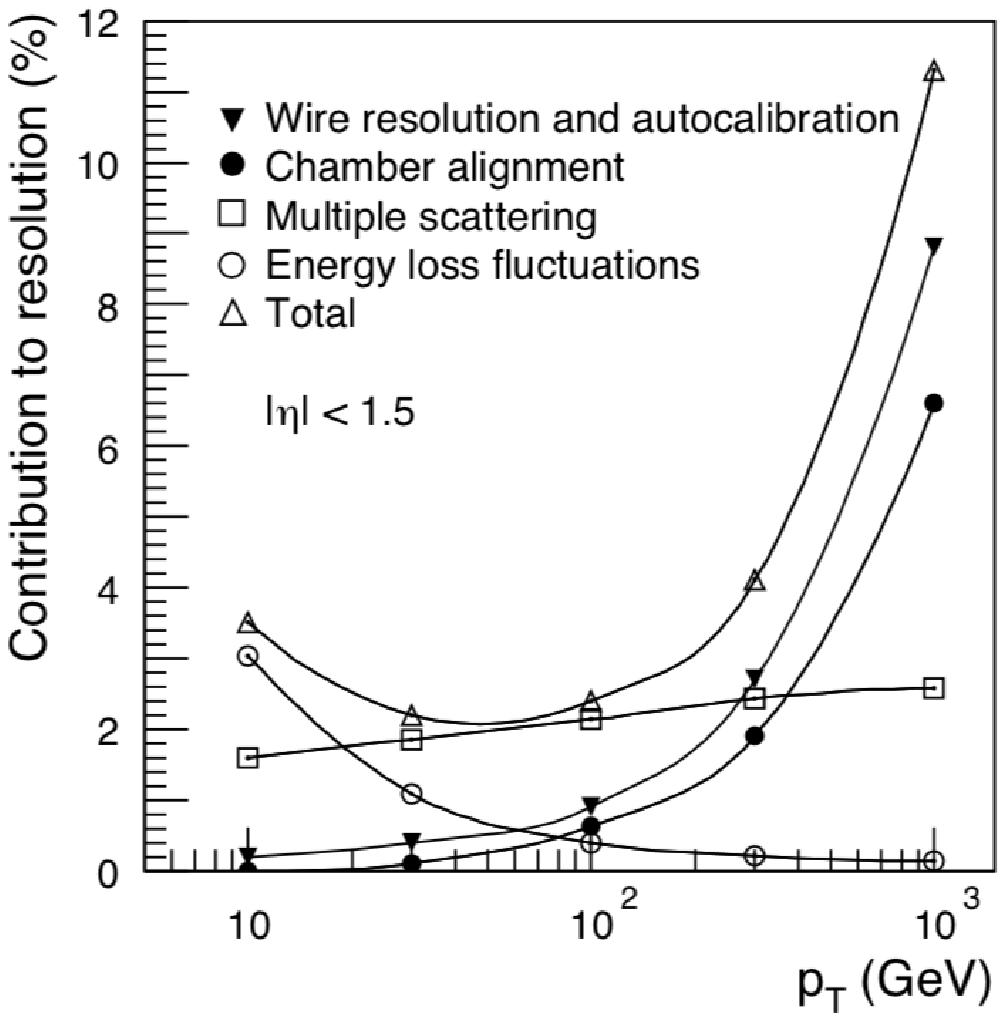

Figure 4.21: The contribution to muon spectrometer p_T resolution from various sources over a range of p_T

[36]

Resistive plate chambers (RPCs)

Resistive plate chambers are used for the muon trigger in the barrel region $|\eta| < 1.05$. In the middle station, there are two layers of RPCs, used for the low-p_T threshold trigger. This trigger threshold is $6-9$ GeV. In the outer station, there is a single layer of RPCs, used for the high-p_T threshold trigger, with a threshold of $9-35$ GeV.

Each RPC consists of two rectangular detectors, called units. Standard RPCs are paired with MDTs, and have the same dimensions. A few additional smaller RPCs are included in areas where MDTs cannot be installed due to lack of space.

Each RPC provides two measurements of η and ϕ for a charged particle passing through it. A charged particle passing through all three layers therefore generates 6 $\eta-\phi$ measurements. To reduce fake tracks, 3 out of 4 of the middle-station detectors and at least one outer layer station must register hits.

An RPC detector consists of two plastic insulating plates, separated by 2 mm, with a gas occupying the internal space. A voltage difference of 9.8 kV is applied across the plates. Charged particles passing through the plates generate an avalanche of charge which can then be measured by metallic strips connected to the plates. The insulator plates are made of phenolic-melaminic plastic laminate, and the gas is a mixture of $\mathrm{C_2H_2F4}$, $\mathrm{Iso-C_4H_{10}}$, and $\mathrm{SF_6}$ in the proportions 94.7%, 5%, 0.3%.[16]

The RPCs provide a time resolution of 2 ns.

Thin-gap chambers (TGCs)

In the forward region, $1.05 < |\eta| < 2.4$, muon triggering is provided by thin-gap chambers (TGCs). TGCs also provide a ϕ measurement to complement the η measurement provided by the MDTs.

In the MDT end-cap middle layer, there are seven layers of TGCs, and in the inner layer, there are 2 layers of TGCs. Each TGC layer consists of two concentric rings..

Like the CSCs, the TGCs are multi-wire proportional chambers (MWPCs). To reduce drift time so that an acceptable time resolution can be achieved, the drift distance must be kept small, and the electric field kept high. The wire-to-cathode distance is 1.4 mm in the TGCs, even closer than the wire-to-wire distance of 1.8 mm. The voltage is kept at 2.9 kV. A highly quenching gas mixture of $55\%\mathrm{CO_2}$ and $45\%\mathrm{n-C_5H_{12}}$ is used in the TGCs.[16]

The time resolution provided by the TGCs is 4 ns.[36]

4.7 Trigger

Because of the very high event rate at the LHC, and the large amount of data collected per event, it is impossible to record every single event. There are 40 million events per second, and each event generates 1.6 MB of raw data. The ATLAS trigger system is designed to make very fast decisions about which events to record and which to ignore, in order to reduce the event rate to approximately 1 kHz. The challenge of trigger design is to balance processing time against decision accuracy, to make sure that events that could be useful for physics analysis are not lost. The selection criteria used by each level of the trigger are known as the trigger menu. A large number of possible trigger selection criteria are designed, in order to serve the broad range of physics analyses performed at ATLAS .

The ATLAS trigger system consists of a hardware based level 1 (L1) trigger, and a software-based high-level trigger (HLT). The L1 trigger reduces the event rate from the original 40 MHz to approximately 100 kHz. The HLT further reduces the event rate to approximately 1 kHz, which is the maximum rate of data transfer from the detector. The flowchart of data through the trigger system can be seen in figure 4.22

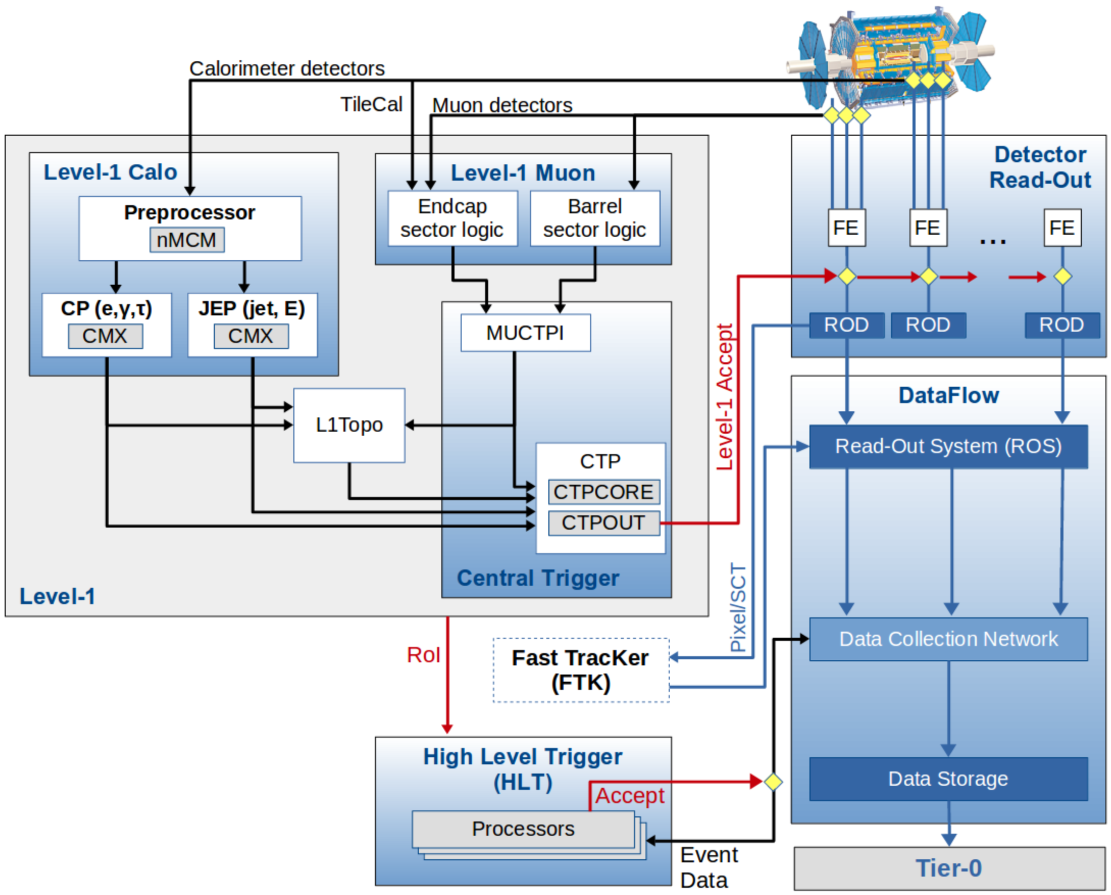

Figure 4.22: Flowchart outlining the level 1 and high-level trigger design and data acquisition system.

For every event, the L1 trigger system reads reduced-granularity measurements from both the hadronic and electromagnetic calorimeters. Special calorimeter cells, called trigger towers, in each calorimeter were designed for this purpose. The trigger towers have a granularity of $\delta\eta \times \delta\phi = 0.1 \times 0.1$. The location of the trigger towers at the back of the electromagnetic calorimeter can be seen in figure 4.13. The L1 trigger also reads data from the RPCs and TGCs of the muon spectrometer system, as discussed in 4.6. The calorimeter data will be used for photon, electron, tau, jet, and E_{Tmiss} triggers, and the muon data will only be used for muon triggers. Data from these two sources are fed into the central trigger processor (CTP), which makes the decision about whether or not accept each event at level 1.

If an event is accepted at L1, full detector raw data for that event is read out and temporarily stored until the HLT decision is made. Some amount of reconstruction is done at this time, including a high-speed, reduced-accuracy version of the tracking algorithms, known as Fast TracKer (FTK). Later, if an event is accepted by the HLT, the full tracking reconstruction algorithm will be applied. The L1 system then sends region-of-interest information to the HLT . Regions of interest are the subsections of the detector that the L1 trigger has identified as possibly containing interesting physics objects. The full detector information and L1 region-of-interest data are combined by the HLT, which then makes the final decision on whether or not to keep an event. Only when an event passes both the L1 and HLT decision criteria will its be permanently stored.

The L1 trigger system desicision time is just 2.5 μm, while the HLT makes decsisons on the order of seconds.

Chapter 5

Jets

A jet is a collimated spray of stable particles measurable in the detector, which arises from the production of a quark or gluon in the scattering process. Due to QCD confinement, the quarks and gluons themselves can never be observed, so jets serve as a kind of observable proxy for these more fundamental particles. However, there is not a simple one-to-one correspondence between each jet measured in an event and a quark or gluon in the hard scattering process. Due to the complex nature of proton-proton collisions, as well as the fundamental probabilistic nature of quantum mechanics, the partonic source for a given jet can never be specified exactly. Likewise, when performing theoretical calculations, the number and property of jets that arise from a given parton produced in the hard scattering can only be specified probabilistically. Section 5.1 will explain the many different parts of a proton-proton collision that contribute to jet production.

Furthermore, the number and properties of jets measured in a single event will depend on the choice of jet reconstruction algorithm. In order for experimentalists to test the predictions of theory, it's important for standard jet definitions to be decided upon. While there is no one theoretically correct choice of jet definition, there are certain properties of jet algorithms that make them more or less desirable. The different kinds of jet algorithms and their properties will be discussed in section 5.2

Section 5.3 will discuss jet substructure, which are the internal properties of jets. And section 5.4 will explain the process of jet reconstruction and calibration in ATLAS.

5.1 The proton-proton collision environment

As discussed in 2.2, the goal of proton-proton collision experiments is to understand the interactions between fundamental particles, but due to QCD confinement it is impossible to simply collide the individual partons of interest. Instead, complicated bound states of quarks and gluons are collided, with the goal of measuring the processes that occur when constituent partons collide with each other. As a result, proton-proton collision events create a very messy environment from which the hard-scatter process has to be deduced.

QCD confinement also has the consequence that the final state quarks and gluons created in LHC collisions can never be directly detected. Instead, collimated sprays of hadrons, called jets, must be measured in order to attempt to reconstruct the hard scattering process that gave rise to them.

Figure 5.1 illustrates a typical proton-proton collision event, in which two gluons annihilate to generate a Higgs boson along with a top-antitop quark pair. Even though this is not a dijet or multijet production event, it is useful for understanding all the parts of a proton-proton collision that must be considered when calculating the predicted rates of multijet production.

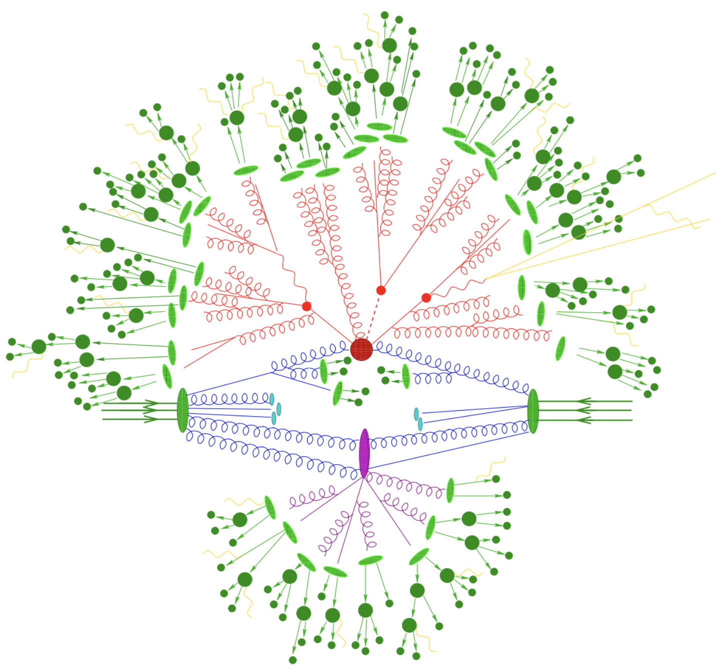

Figure 5.1: Diagram of a proton-proton collision event in which the hard scatter process is $t\bar{t}H$ production. Illustrated are the initial state radiation, underlying event, hard-scatter process, final state parton shower, fragmentation, hadron decays, and final state QED radiation.

[22]

The incoming protons are illustrated by green blob with three incoming arrows to represent the constituent quarks. The initial state parton showering, governed by QCD, is shown in blue. The hard scatter process, in which two gluons annihilate to produce a Higgs boson and top-antitop pair is represented by the large red circle. Quarks and gluons from the incoming proton that do not participate in the hard scatter process can nonetheless interact with each other, creating a so-called underlying event, shown in purple. The Higgs decays to a quark-antiquark pair, shown in red, and all of the strongly-interacting final state quarks and gluons undergo final state parton showering, also in red. Once the final state parton shower particles reach a low enough energy, they hadronize, a non-perturbative process indicated by the light green blobs. The resulting hadrons then decay through various decay chains, shown in dark green. Photon radiation, governed by QED, can occur at any of these stages, and is shown in yellow.

The final measured objects in the detector are the jets. But every process leading up to the final state is quantum mechanical, meaning that interference terms between the various processes lead to a fundamental and unresolvable ambiguity in the source of a given jet.

An event with 3 high-pT jets could be explained by a $2 \to 3$ hard-scattering process, or a $2 \to 2$ hard scattering process, with an additional jet arising from ISR or FSR, the underlying event, or even from a hadronic decay. All of these processes must be taken into account when calculating the rate of 3-jet events, each contributing its own source of uncertainty. The final rate calculation combines the perturbative QCD calculations for the matrix elements and parton showering with empirically measured probability distributions for the non-perturbative parts of the collision, including soft gluon emission, long-distance couplings, hadronization, and multi-parton interactions (MPI). As the number of jets in the final state increases, so does the complexity and uncertainty when calculating event rates.

Monte Carlo (MC) generators attempt to account for all of these effects to calculate the rate of multijet events at the LHC . However, the MC estimates have very large uncertainties, for the reasons given above. As a result, data driven estimation methods are used for determining the background rate of multijet events.

5.2 Clustering Algorithms

In order to measure jets in an event, a decision has to be made on the type of jet reconstruction algorithm to use. The observable result of a collision event can consists of many clusters of stable particles or calorimeter hits. Exactly which particles to cluster together is highly non-trivial, and developing the algorithms to make these decisions is an active area of research in particle physics.

The 1990 Snowmass accord defined a set of criteria which should be met by any jet algorithm. The criteria for a developing a jet reconstruction algorithm are:

1. Simple to implement in an experimental analysis
2. Simple to implement in the theoretical calculation
3. Defined at any order in perturbation theory
4. Yields finite cross sections at any order of perturbation theory
5. Yields a cross section that is relatively insensitive to hadronization

[37, 26]

Jet reconstruction algorithms that meet all of these criteria allow experimentalists to test theoretical prediction, because both the theoretical calculations and experimental analysis can use the same jet definition. Jet algorithms are defined as acting on abstract "objects". The last Snowmass criteria ensures that in theoretical calculations, jet algorithms can be applied at either the parton-level or hadron level. In either case, the object which the algorithm acts on will be a particle. Jet algorithms can also be applied by experimentalists to reconstruct jets from either simulated or real calorimeter hits. In this case, the object which the algorithm acts on is a cluster of calorimeter hits.

Historically, there have been two major types of jet algorithms used in particle physics experiments: cone-based algorithms and sequential recombination algorithms. Cone-based algorithms, which were developed first, aim to cluster jets in $\eta - \phi$ space. They are fast and easy to implement, and produce jets with regular boundaries in $\eta - \phi$ space, but have many theoretical and practical downsides compared to sequential recombination algorithms. They typically use the highest-transverse-momentum (hardest) object in the event as a seed for a jet cone, then define a cone around that seed as the leading jet, before moving on to the next-hardest object. Cone-based algorithms have the advantage of producing regularly-shaped jet boundaries, which can simplify theoretical calculations and make experimental calibration easier [7]. However, cone-based algorithms typically collinear safety, which are properties that need to be satisfied to meet the Snowmass criteria.

IRC Safety

Jet algorithms should ideally possess infrared and collinear (IRC) safety. This means that their results should not change due to soft gluon emissions or near-collinear emissions during either the parton shower or hadronization process. IRC safety is important because soft and collinear emissions are extremely common in QCD, occur randomly, are hard to predict, and can lead to divergences in perturbative calculations if the algorithm is IRC-unsafe.[37]

Collinear safety

A collinear-safe algorithm is insensitive to near-collinear emissions that occur during parton showering or hadron decays. Cone-based algorithms are collinearly unsafe because they seed jets with the hardest object in the event, which is very likely to change if there is a near-collinear emission.

In figure 5.2, for the collinear-unsafe cone-based algorithm, the hardest object in the event changes depending on whether the radiated gluon is reabsorbed or emitted nearly collinear to the original quark. Thus, the resulting seed will change, yielding different jet results. The loop diagram and collinear emission diagram both lead to divergences in the theoretical cross-section. In a collinear-safe algorithm, the two divergences would cancel out because both amplitudes must be added to calculate the rate of the single jet being produced.

But in a collinear-unsafe algorithm, the two divergences do not cancel out, so perturbation cross-sections are not finite.

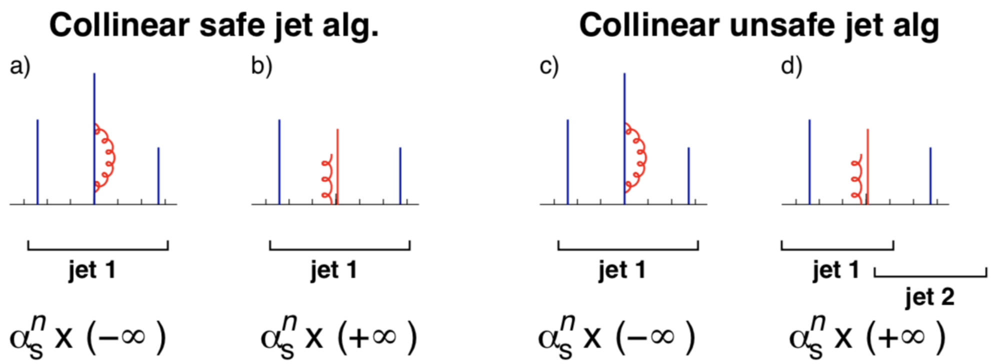

Figure 5.2: Illustration comparing the results of collinear-safe (left) and collinear-unsafe (right) jet clustering algorithms. The emission of a near-collinear gluon changes the number of jets in the event, and results in diverges in theoretical calculations. The x-axis represents rapidity, and y-axis represents transverse momentum.

[37]

Infrared safety

A related concept is that of infrared safety. Jet algorithms should insensitive to soft gluon emissions. These emissions are extremely common during parton showering, and since they occur in the non-perturbative regime of QCD, very hard to accurately predict.

Figure 5.3 illustrates the result of an infrared-unsafe algorithm. A W boson decays to a quark-antiquark pair, which should result in two hard jets. Diagrams (b) and (c) each lead to IR divergences, which would cancel if the algorithm is infrared-safe. But for an infrared-unsafe algorithm, diagram (c) leads to a different number of jets from diagram (b), so the divergences do not cancel.

[37]

Sequential recombination algorithms

Sequential recombination algorithms are the most commonly used jet algorithms in ATLAS today. Instead of clustering in $\eta - \phi$ space, they cluster in transverse momentum space. The resulting jets have irregular boundaries, which adapt to soft radiation. Sequential recombination algorithms are generally slower to run, but have become more popular since the invention of the FastJet[9] algorithm. Sequential recombination algorithms are IRC safe.

All sequential recombination algorithms start by defining a distance measure:

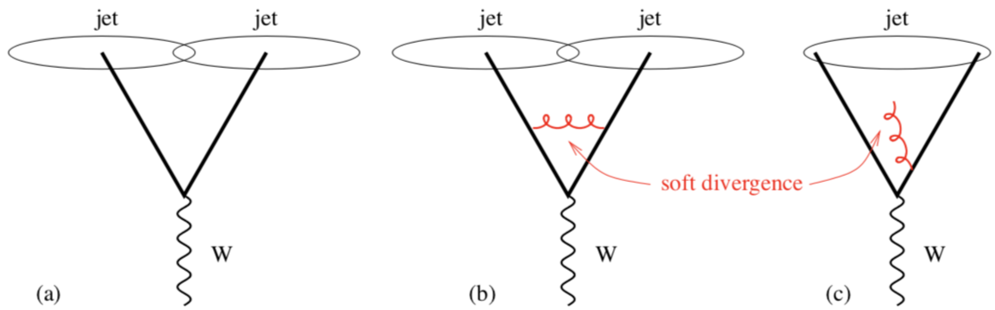

Figure 5.3: Illustration of infrared unsafety. In an event with a W boson decaying to two hard partons, the emission of a soft gluon can change the result of an infrared-unsafe algorithm.

$$d_{ij} = min\left(k_{Ti}^{2p}, k_{Tj}^{2p}\right)\frac{\Delta_{ij}}{R^2} \tag{5.1}$$

$$d_{iB} = k_{Ti}^{2p} \tag{5.2}$$

Where the indices i and j are used for two objects under consideration, d_{ij} is the distance between those two objects, k_T is the transverse momentum, $\Delta_{ij}^2 \equiv (\eta_i - \eta_j)^2 + (\phi_i - \phi_j)^2$ is the distance-squared in $\eta - \phi$ space, and p and R are two parameters that control the behavior of the algorithm. The object-beam distance, d_{iB} is also used by the algorithms, and is defined for each object individually rather than for pairs of objects.

The choice of R^2 roughly controls the area of the resulting jets. It is often referred to as a radius parameter, but the jets that result from these algorithms have irregular shapes, so this term is used loosely.

The choice of p determines the class of sequential recombination algorithms, each of which has different properties.

All sequential reclustering algorithms use these distance measures in the following way:

1. Calculate d_{ij} over all pairs of objects, and d_i for each object individually

2. If the minimum of the set $\{d_{ij}, d_i\}$ is one of the d_{ij}'s:

   Sum the four vectors of objects i and j

   Add the resultant four-vector to the list of objects, and remove the four vectors for objects i and j

   Go to Step 1

3. Else if the minimum of the set $\{d_{ij}, d_i\}$ is one of the d_i's:

   Call the object i a jet

Remove the object i from the list of objects

Go to Step 1

An inclusive clustering algorithm stops when all objects have been clustered into a jet. An exclusive algorithm stops when a pre-defined number of jets have been clustered.[6]

The Cambridge-Aachen (C/A) algorithm has $p = 0$, and so does not directly use the transverse momentum of the jets. Instead the distance measure is purely in terms of pseudorapidity and azimuthal angle, so objects are clustered based on how close together they are in this radial distance measure. The boundaries of resulting jets are sensitive to random fluctuations of soft objects, such as those from pileup and the underlying event.

The k_T algorithm has $p = 1$, and so starts by clustering objects which are both spatially close together and have low momentum. Like with the C/A algorithm, the resulting jets are sensitive to random flucutations in soft objects from pileup and the underlying event.

In the anti-k_T algorithm, the objects which are closest together and hardest are clustered together first. The resulting jet shapes are insensitive to the details of the soft radiation. So the impact of pileup and the underlying event on jet momentum resolution is smallest for the anti-k_T algorithm[8].

A comparison of the different jet clustering algorithms can be seen in figure 5.4. The same parton-level simulated event data was input into four different jet clustering algorithms. Random soft particles were also added to the parton-level event data. The resulting jets are plotted in $y - \phi$ space, with colors labelling the different jets, and the height of each bar indicating the transverse momentum in that region. For the k_T and C/A algorithms, the jet boundaries are highly irregular, and depend strongly on the details of the random soft particles.[8]

[8]

5.3 Boosted objects

As the center-of-mass energy of collisions increases, it becomes increasingly important to study the internal structure of jets, in addition to the kinematic properties of jets within events. The decay products of hadronically-decaying heavy objects, such as W or Higgs bosons, become harder to resolve into separate jets as the momentum of the original object increases. Recently, a large number of jet substructure observables have been developed, and an entire subfield has emerged dedicated to the study of the internal properties of jets.

For a two-pronged decay, for example $W \to q\bar{q}$, the angular separation between the decay products is given by:

$$\Delta R = \frac{p_T}{2m} \tag{5.3}$$

Where p_T is the transverse momentum of the W, and m is the W mass. For W bosons with $p_T \gg m$, jets with radius parameter $R = 0.4$ will no longer resolve the decay products into separate jets, but instead will contain the all decay products of the W into a single jet.

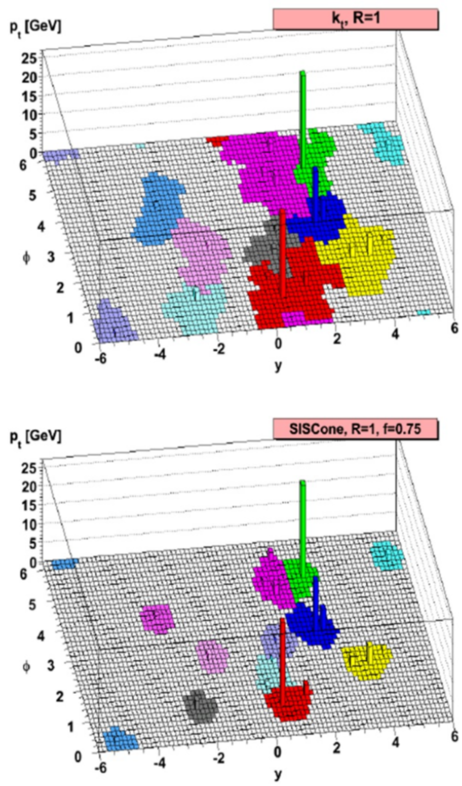

Figure 5.4: Results of running four different jet clustering algorithm on the same set of parton-level simulated event data. SISCone (lower-left) is a cone-based algorithm, while the other three are sequential recombination algorithms defined by different values of p.

Figure 5.5 illustrates the boosting effect for the simulated decay $Z' \to t\bar{t}$, where the Z' represents a new heavy resonance. Since $m_{Z'} \gg m_t$, the top quarks are highly boosted, so their decay products cannot be resolved by jets with $R = 0.4$.

On the other hand, jets with $R = 1.0$ will capture all decay products with high efficiency, so the substructure of $R = 1.0$ jets can potentially be used to reconstruct these boosted tops.

When dealing with boosted objects, larger radius parameters are often used, in order to increase the probability of capturing the full decay products of a boosted object. Jets with large radius parameters, typically $R = 1.0$ or $R = 1.2$ are referred to as fat jets.

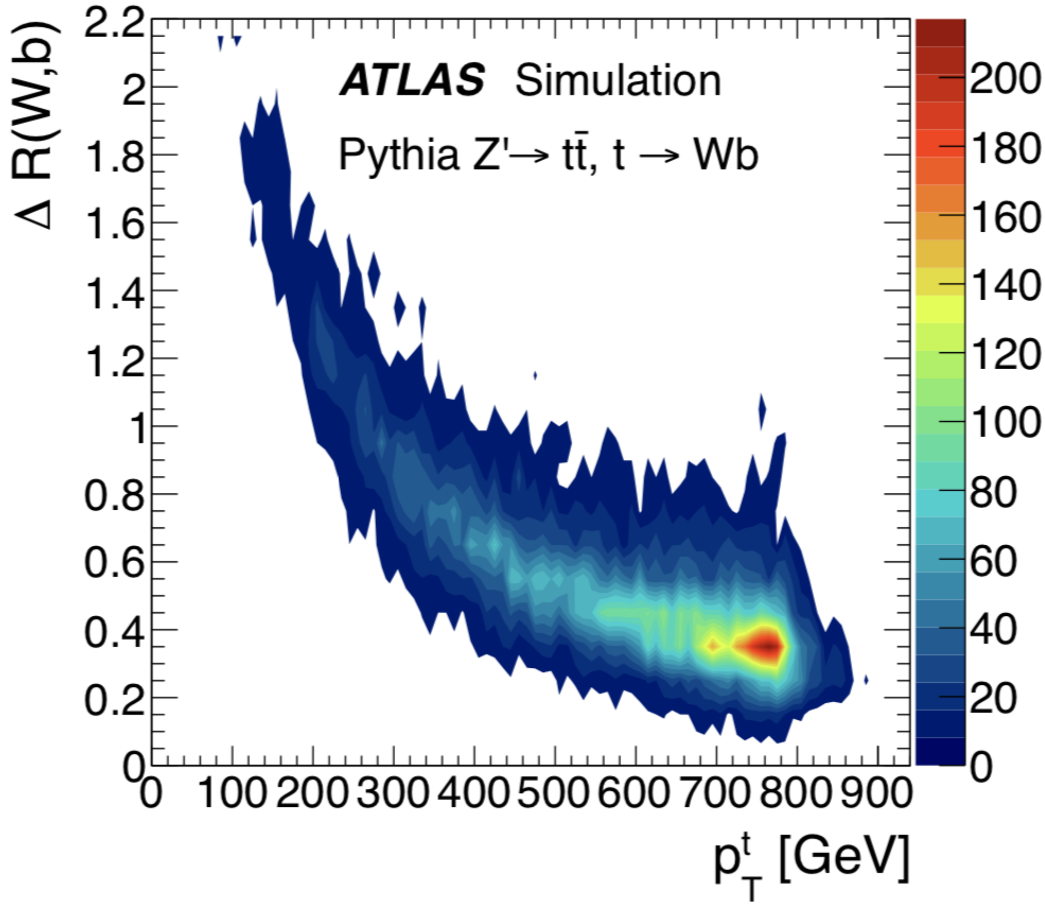

Figure 5.5: Radial separation between top decay products vs. top-quark p_T for top quarks produced from a theoretical heavy resonance, Z'

Jet Mass

Jet mass origin

The earliest-developed, and most straightforward jet substructure observable is mass. The mass of a jet is calculated from the four-vectors of its constituent objects:

$$m^2 = \left(\sum E_i\right)^2 - \left(\sum \vec{p}_i\right)^2 \tag{5.4}$$

For a jet that contains the collimated decay products of an individual boosted resonance, the mass of the jet corresponds to the mass of the resonance, $m_{jet} \approx m_{resonance}$.

For a QCD jet, i.e. one that is a result of a high-p_T gluon or light quark, one might expect the mass to also be very low or close to zero. But in fact perturbative QCD processes lead to a nonzero expected mass for light quark and gluon jets. Calculations of perturbative QCD jet mass is beyond the scope of this thesis, but the resulting mass is proportional to the jet radius parameter, R, and the transverse momentum p_T of the jet. Jets arising from light quarks will have different mass than jets arising from gluons. After taking relative production cross-sections for quark and gluon jets into account at different energy scales, the resulting relationship between jet p_T and mass at next-to-leading order (NLO) is well-approximated by:

$$m \approx 0.2 p_T R \tag{5.5}$$

[20]

Trimming

Additional contributions to the jet mass come from initial state radiation (ISR), pileup (PU), the underlying event (UE), and multi-parton interaction (MPI).

A variety of so-called grooming techniques are used to remove the dependence on unassociated radiation, so that the resulting jet mass is a result of the hard-scattering process only.

Trimming is a grooming method applied to fat jets after they have been clustered, typically with the anti-k_T algorithm. Trimming is defined as:

For each fat jet:

1. Recluster the fat jet constituents with a smaller radius parameter, R_{sub}
2. Reject subjets with $p_T < f_{cut} p_T^{jet}$
3. Sum the four-vectors of the subjets that are not rejected to form the final trimmed jet

In the first step, a radius parameter and clustering algorithm must be chosen. The subjet radius parameter must be smaller than the original radius parameter. Often the k_T algorithm is used for subjet clustering, in order to preserve as much of the FSR as possible. Rejecting FSR results in reduced jet mass resolution.[38] The trimming procedure is illustrated in figure 5.6

The values of R_{sub} and f_{cut} can be chosen to reduce pileup sensitivity and maximize jet mass resolution for the signal of interest.

The effect of different grooming techniques, including trimming, on jet mass resolution can be seen in figure 5.7. For dijet events, high-mass jets are highly suppressed by grooming, which leads to a better signal-to-background ratio for signals of hadronically decaying boosted objects with QCD dijet backgrounds. For $t\bar{t}$ events, the top-mass peak is somewhat visible before grooming, although much wider than after grooming. The W-mass peak, which is originally completely hidden due to unassociated radiation effects, can be recovered with any of the grooming methods.

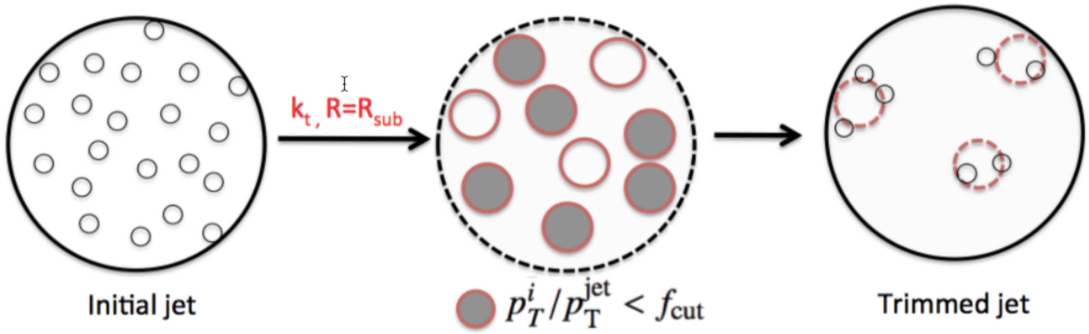

Figure 5.6: Illustration of the trimming procedure, one of several grooming methods used to remove the contribution of unassociated radiation to fat jet mass.

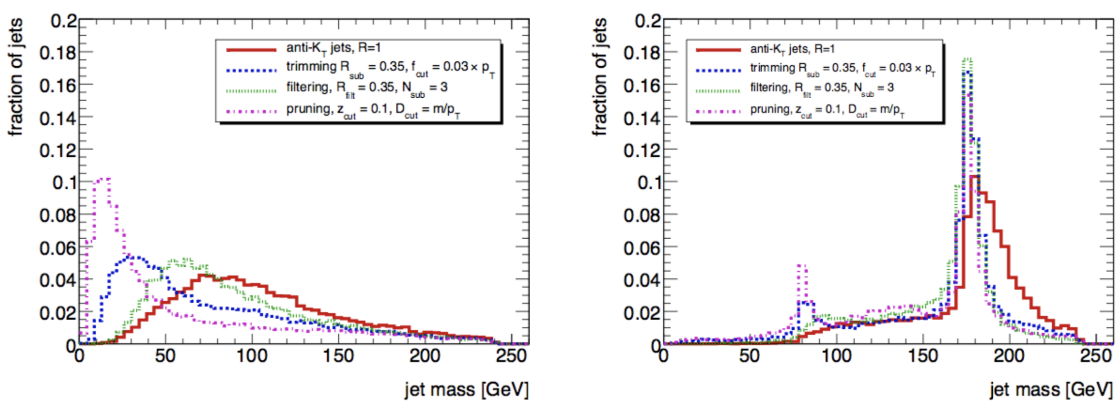

(a) dijets, 500–600 GeV (b) $t\bar{t}$, 500–600 GeV

Figure 5.7: Measured jet mass distributions before and after grooming, for various grooming techniques. Mass distributions are shown for both dijet events (left) and $t\bar{t}$ events (right).

5.4 Reconstruction in ATLAS

The goal of jet measurements in ATLAS is to capture and reconstruct both the energy and momentum of jets leaving the collision point. Calorimeter jets use clusters of calorimeter cell hits as inputs to the clustering algorithms outlined in 5.2.

Topological cell clusters

Topological cell clusters, or topo-clusters, are three-dimensional clusters of calorimeter cell energy measurements. By clustering groups of calorimeter cells into topo-clusters, the number of inputs to the jet reconstruction algorithm is reduced. Topo-clustering also reduces calorimeter noise by rejecting cell signals not associated to other nearby significant cell signals.[3] Topo-clusters serve as the main input to the jet clustering algorithms when reconstructing calorimeter jets in ATLAS . The two sources of calorimeter cell noise are electronic noise and pileup.

The algorithm is based on the signal-to-noise ratio in each cell, $\zeta_{cell} = E_{cell}/\sigma_{cell}$. There are three tunable parameters used in the algorithm, labeled S, N, and P, where $S > N \geq P$.

For purposes of the algorithm, a cell is considered to be a *neighbor* of another cell if the two cells are adjacent in the same layer, or if they are in adjacent layers and have any overlap.[3]

The algorithm is as follows:

- Label any cell with $\zeta_{cell} > S$ a seed cell.
- Collect all neighboring cells to a seed cell into a proto-cluster.
- If any cell in the proto-cluster has $\zeta_{cell} > N$, collect its neighbors into the proto-cluster.
- Repeat the previous step until the set of neighbors collected has $\zeta_{cell} < N$.
- Reject any cells with $\zeta_{cell} < P$.

At any time in the algorithm, if any cell with $\zeta_{cell} > N$ belongs two proto-clusters, then the two proto-clusters are merged.[3]

Once the algorithm terminates, the final set of topo-clusters are used as the inputs to the desired jet clustering algorithm.

A result of this algorithm is that isolated cells with $\zeta_{cell} < N$ are rejected, which reduces that amount of noise entering the jet clustering algorithm. These cells are less likely to contain signal than cells with $\zeta_{cell} < N$ that neighbor cells with higher signal-to-noise ratio.

This clustering algorithm does not guarantee that all the energy of a given particle in the jet will be captured by a single topo-cluster, nor does it guarantee that a single topo-cluster only contains energy from a single particle. So topo-clusters are not measurements of individual particles in the jet.

The three parameters S, N, and P are tuned on test-beam data with known energy to maximize the measured energy while minimizing the energy resolution[39].

Results of the test beam energy measurements with 180 GeV and 20 GeV pions can be seen in 5.8.

[39]

Based on these measurements, the default parameter values chosen for ATLAS topo-clustering are $S = 4$, $N = 2$, $P = 0$.

The topo-cluster four momenta are used as the input objects to the jet clustering algorithms. Other properties of the topo-clusters, known as cluster moments, are used in calibration of the topo-clusters.

(a) Average of the energy deposited in all clusters by 180 GeV pions

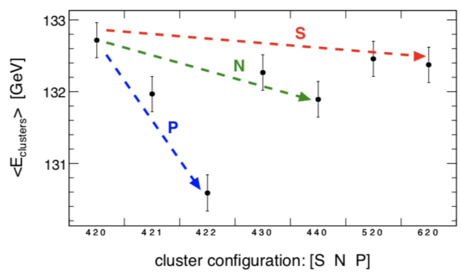

(b) Resolution of the distribution of the energy deposited in all clusters by 180 GeV pions

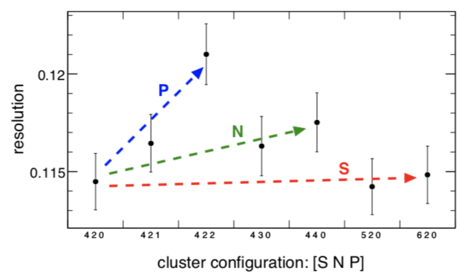

(c) Average energy deposited in all clusters by 20 GeV pions

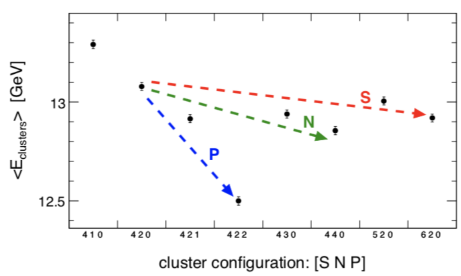

(d) Resolution of the distribution of the energy deposited in all clusters by 20 GeV pions

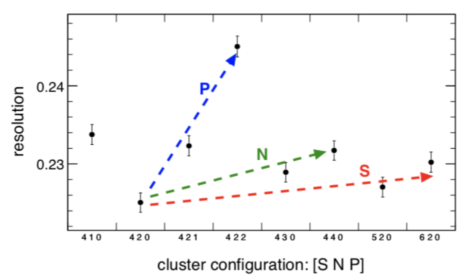

Figure 5.8: Average energy and energy resolution measured for 180 GeV and 20 GeV pions with different values of the topo-clustering parameters S, N, and P. The x-axis of each plot represents choices for all three parameters, and the y-axis indicates either the average energy deposited in each cluster $< E_{clusters} >$ or the energy resolution $RMS/ < E_{clusters} >$

Calibration

Calibration of topo-clusters is performed before inputting them into the jet clustering algorithms. Calibration is needed in order to correct for the calorimeters' differing response to electromagnetic and hadronic showers, to correct for signal loss arising from the clustering algorithm, and to account for signal loss due to inactive material. The calibration strategy known as Local Cell Weighting (LCW) is used to correct for all three of these.

Calibration is done using Monte Carlo simulations of neutral and charged pions in a simulated detector. Pions with energies up to 2 TeV and over a range of η values are used.

Topo-cluster calibration

subsubsec:topo$_calibrationHadronicandelectromagneticresponsesTheATLAScalorimetersarenon-compensatingcalorimeters, whichmeanstheyhavealowerresponseforhadronicshowersthanforelectroma$

$clusterarosefromanelectromagneticshower. This probability is called P^{EM}$. The calibration weight for cell i in cluster j is then:

$$w_i = P_j^{EM} w_i^{EM} + \left(1 - P_j^{EM}\right) w_i^{had} \tag{5.6}$$

Where P_j^{EM} is the predicted probability that cluster j arose from an electromagnetic shower, w_i^{EM} is the calibration weight for cell i assuming the electromagnetic response, and w_i^{had} is the calibration weight for cell i assuming the hadronic response.[3]

Cluster classification probabilities are determined using the topo-cluster depth and signal density, as hadronic showers tend to deposit energy deeper in the calorimeter and have lower energy density.[3]

Figure 5.9 shows the EM classification probability as a function of these two topo-cluster moments. The cell signal density is measured as energy density of the cell normalized to the total energy of the cluster to which it belongs.

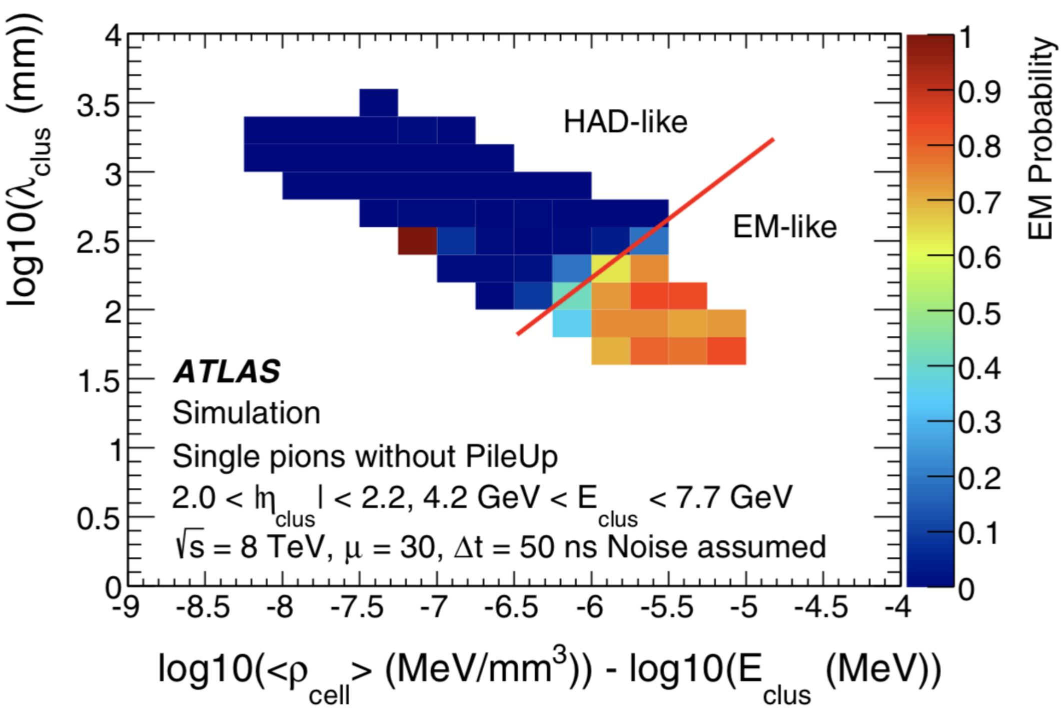

Figure 5.9: Cluster EM probability as a function of normalized cell signal density and depth. Cell that are farther away from their cluster's center, and with lower energy density are more likely to arise from hadronic showers. The red line indicates the 50% boundary: cells falling on that line have a 50% probability of arising from electromagnetic showers, while clusters below that line have a higher probability.

[3]

The hadronic calibration weight is then determined as

$$w_i^{had} = \frac{E_i^{dep}}{E_i^{EM}} \tag{5.7}$$

Where E_i^{dep} is the true energy deposited in the cell, and E_i^{EM} is the energy measured in the cell.

Out-of-cluster During the topo-clustering process, cells with signal fractions belows the necessary thresholds can be rejected, resulting in a certain amount of signal energy being lost.

Lost cells with true signal energy deposited are attributed to nearby clusters. The relevant search area for a cluster depends on the cluster η, and ranges from 14 deg to 60 deg.[3] Lost cells can be attributed to more than one cluster, with a weight proportional to the energy deposited in each cluster.

An out-of-cluster correction weight is then calculated as

$$w_j^{ooc} = \frac{E_j^{ooc} + E_j^{dep}}{E_j^{dep}} \tag{5.8}$$

Where E_j^{ooc} is the total energy deposited in lost cells associated to the cluster, including a fraction of the energy from lost cells shared by multiple clusters.

This correction is determined separately for electromagnetic and hadronic showers, using neutral and charged pions respectively[3]

Dead material

Dead material is also accounted for using simulated pions in a simulated detector. Figure 5.10 shows an illustration of the lost cell and dead material calibration procedure.

Jet Calibration

After calibration, the jet clustering algorithms can be run on the topo clusters according the procedures decribed in 5.2.

After jet clustering, further calibration is required on the resulting jets in ord

Flavor Tagging

Simulation

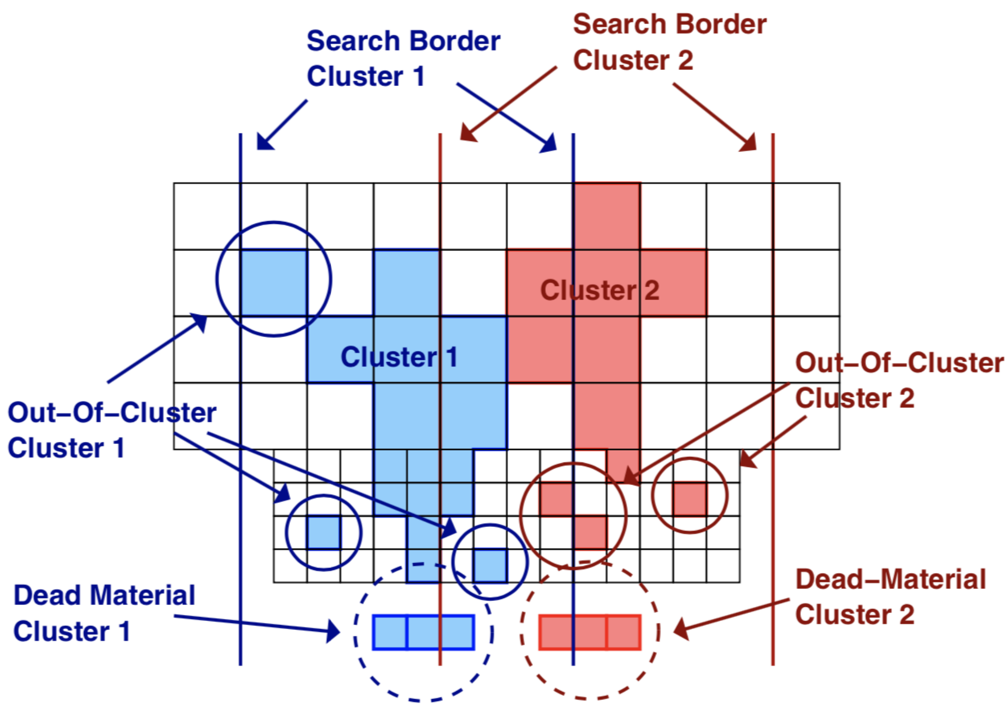

Figure 5.10: Illustration of the procedure used to account for signal lost to lost cells and dead material.

[3]

Chapter 6

Search Strategy

6.1 Strategy Overview

A data-driven method is used to predict the background yield in the signal regions, as well as the uncertainties on those predictions. First, jet mass templates are created from control region jets. Randomized jet masses, known as dressed masses, are generated from these templates for each jet in the kinematic sample. Summing the dressed masses for each of the up to four leading jets in an event gives the dressed M_J^{Σ} for that event. The dressed M_J^{Σ} distribution for each signal region is used to estimate the expected background contribution to that region.

6.2 Discriminating Variables

Two of the main discriminating observables, namely M_J^{Σ} and $|\Delta\eta_{12}|$ are the same as those used in the Run-1 version of the analysis [15].

The first observable, M_J^{Σ}, is the scalar sum of the first four leading large-R jets, ordered by p_T, in an event. Large-R jets have $R = 1.0$ and are required to have $p_T > 200\ GeV$ and $|\eta| < 2.0$. In case an event has less than four jets, the sum of all large-R jet masses passing the kinematic cuts is used.

M_J^{Σ} provides good separation between signal and background because it takes into account both the energy and angular structure of an event, unlike a purely energy-dependent observable like H_T [4, 5].

The second discriminating variable is $|\Delta\eta_{12}|$, which is the pseudorapidity differences between the first two leading jets in an event. Events with small $|\Delta\eta_{12}|$ have their leading two jets more central than average. For regions with high jet multiplicity, requiring large $|\Delta\eta_{12}|$ reduces the signal to background ratio, allowing for the creation of high-multiplicity control and signal regions.

Distributions of the two discriminating variables are shown in figure **??** for data as well as background and signal Monte Carlo.

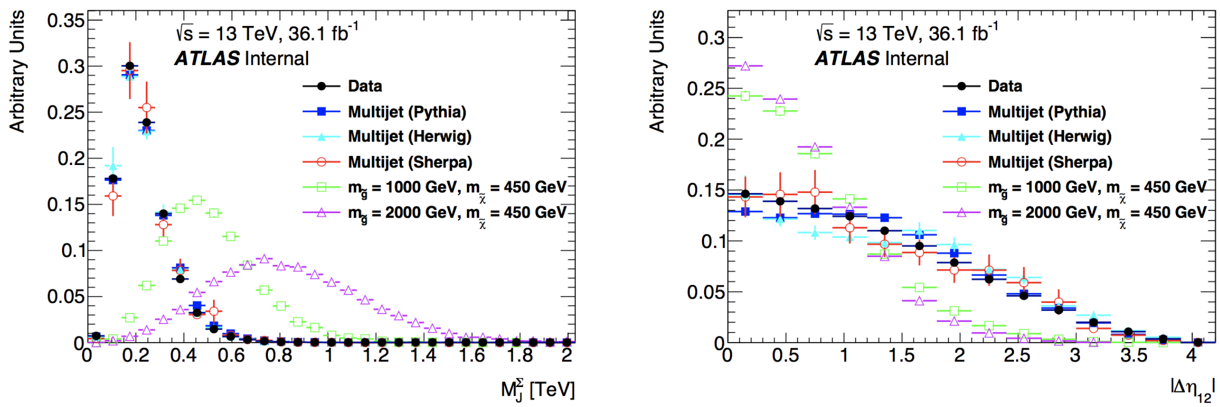

(a) M_J^Σ (b) $|\Delta\eta_{12}|$

Figure 6.1: Distributions of the two main discriminating observables, (a) the scalar sum of the four leading large-R jets, M_J^Σ and (b) the difference in pseudorapidity between the two leading jets, $|\Delta\eta_{12}|$. Selected events have ≥ 4 large-R jets. Distributions are shown for both data and simulated signal and background samples. The red and green signal distributions are for the cascade decay mode, and the violet distribution is the direct decay mode, for the superpartner masses indicated.

6.3 Data-Driven Background Estimation

A data-driven jet mass template method is used to estimate the background. The method is similar to that used in the Run-1 version of the analysis [15], with a few important differences.

In the Run-1 analysis, the templates were smoothed with a kernel density estimate before sampling the dressed masses. In this version of the analysis, the templates remain binned. This allows for an estimate of the statistical uncertainty from the control sample size. By Poisson fluctuating each template bin before sampling, the statistical uncertainty is propagated to the dressed M_J^Σ distributions.

Secondly, in the Run-1 version of the analysis, two separate sets of templates were generated: one set for the leading two jets in each event, and one set for the third leading jet. In this analysis, the templates are instead divided into b-matched and non-b-matched jets. The discrepancy in template shape between b-matched and non-b-matched jets was seen to be larger than that between the third leading jet and first two leading jets.

Finally, the Run-1 version of the analysis used Monte-Carlo non-closure as one contribution to the background systematic uncertainty. In this analysis, a data-driven method is used instead. This is due to the fact that the sample size of available simulated data was not large enough to make an accurate estimate of the non-closure.

Jet mass templates

Jet mass templates are derived from a signal-depleted control region consisting of events with exactly three large-R jets. For each p_T, $|\eta|$, and b-match bin, the distribution of individual jet masses in that bin is taken as the template. The templates combine to form the binned conditional probability distribution: $p(m|p_T, |\eta|, b - match)$.

Separate templates are created for b-matched and non-b-matched jets. For the b-matched templates, only events with $|\Delta\eta_{1,2}| > 1.4$ are included in the templates. Templates derived from b-matched jets are used to dress b-matched jets in the kinematic sample, and templates derived from non-b-matched jets are used to dress non-b-matched jets in the kinematic sample.

Each template is a one-dimensional histogram of $\log(m/p_T)$, with 50 bins. Jets with $\log(m/p_T) < -7$ are excluded from the templates.

Example templates are shown in figure 6.2 for two representative p_T-$|\eta|$ bins. A clear difference can be seen between the templates derived from b-matched and non-b-matched jets. Jets that are b-matched have a higher value of m/p_T than non-b-matched jets, for the same p_T-$|\eta|$ bin. This feature can be seen in both data and simulation. Additionally, agreement between data and simulation is observed in the general template shapes.

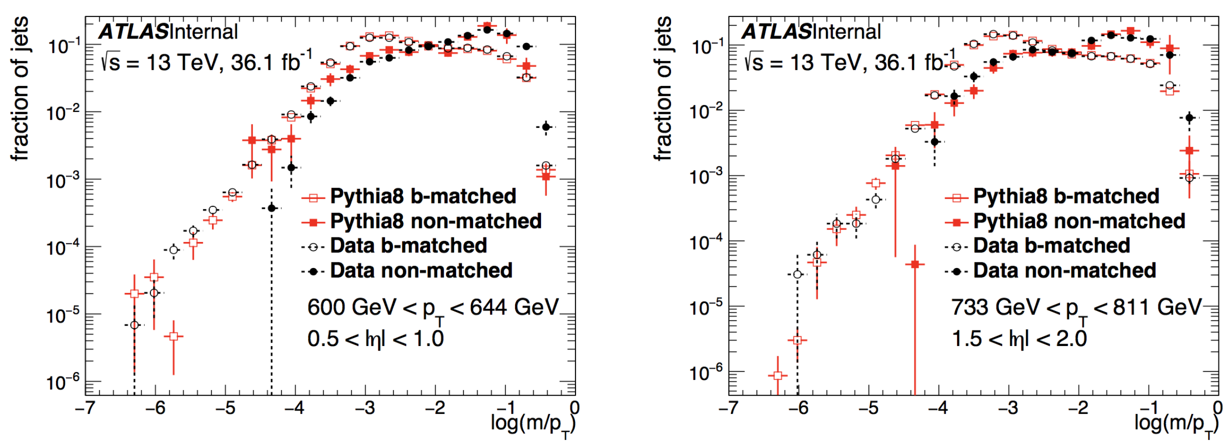

(a) 600 GeV < p_T < 644 GeV, 0.5 < $|\eta|$ < 1.0 (b) 733 GeV < p_T < 811 GeV, 1.5 < $|\eta|$ < 2.0

Figure 6.2: Two representative template distributions used in the analysis, showing a comparison between data in black and simulation in red. The solid markers show the templates derived from b-matched jets, while the empty markers show the templates derived from non-b-matched jets. In (a), template jets are required to have $600\ GeV < p_T < 644\ GeV$ and $0.5 < |\eta| < 1.0$. In (b), templates jets are required to have $733\ GeV < p_T < 811\ GeV$ and $1.5 < |\eta| < 2.0$.

Templates are binned in p_T and $|\eta|$. The p_T bins are approximately logarithmic, while the $|\eta|$ bin boundaries are at 0.0, 0.5, 1.0, and 1.5.

The template binning and number of jets contributing to each bin are shown in figure 6.3.

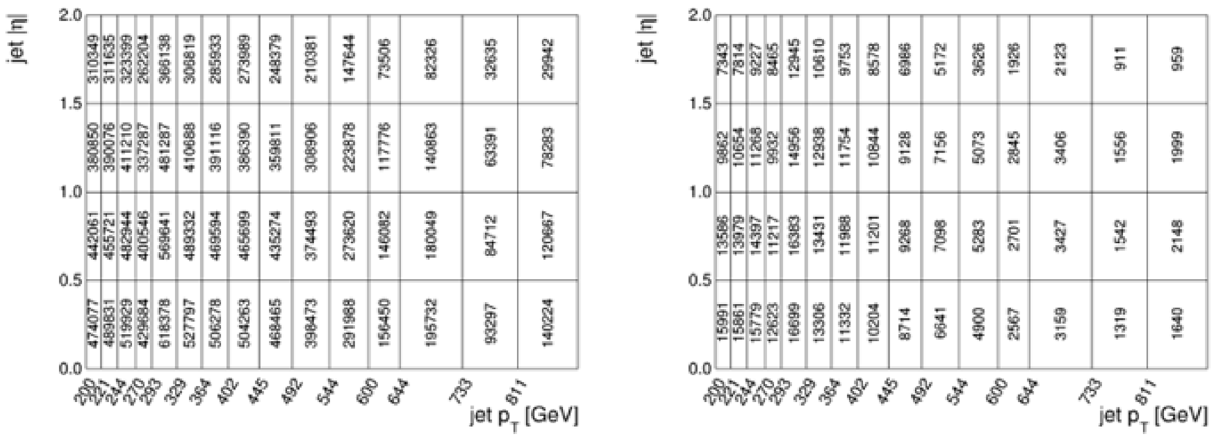

Figure 6.3: Number of jets contributing to each template bin for the non-b-matched (left) and b-matched (right) templates.

Dressed mass and dressed M_J^Σ

For each jet in the kinematic region, a dressed mass is generated by sampling from the template corresponding to its p_T, $|\eta|$ and b-match bin. To generate a dressed mass, the empirical cumulative distribution fucntion (ECDF) is calculated for the template. A uniform random number, y, in the range $[0, 1)$ is then generated. The inverse of the ECDF, $\Phi^{-1}(y)$, gives a randomized $\log(m/p_T)$ bin. A second uniform random number, x, is sampled from the range $[x_1,x_2)$, where x_1, x_2 are the edges of the selected bin. The dressed mass is then computed as $m_{dressed} = p_T e^x$.

To obtain a dressed M_J^Σ for an event, one dressed mass is generated for each jet, and the dressed masses are summed. For events with more than four jets, only the first four leading jets are included in the sum.

Dressed M_J^Σ distributions

To obtain the nominal dressed M_J^Σ distribution, n_{toys} histograms of M_J^Σ are created, where each histogram is generated by dressing all events in the sample once. For each M_J^Σ bin, the average bin content over all histograms is taken as the nominal value, and the standard deviation of bin contents is taken as one contribution to the statistical uncertainty.

The M_J^Σ histograms are binned in the following manner. There are ten equal-width bins covering the range $0\ TeV \leq M_J^\Sigma < 0.5\ TeV$. The next three bins cover the ranges

$0.5\,TeV \leq M_J^\Sigma < 0.6\,TeV$, $0.6\,TeV \leq M_J^\Sigma < 0.8\,TeV$, and $0.8\,TeV \leq M_J^\Sigma < 1.0\,TeV$. The final bin is $M_J^\Sigma \geq 1.0\,TeV$

Normalization

The dressed M_J^Σ distributions are scaled such that the dressed yield in the range $0.2\,TeV < M_J^\Sigma < 0.4\,TeV$ is equal to the kinematic yield in the same range. Separate scale factors are derived for each of the validation and signal regions.

Calculating nominal and systematically-shifted predictions

To determine the nominal predicted background yield, one thousand toys are generated, where a toy consists of a dressed M_J^Σ value for each event in the kinematic sample. For each toy, the number of events with dressed M_J^Σ greater than the signal region M_J^Σ cut are counted, giving a distribution of one thousand dressed background yields. The central value of this distribution is multiplied by the scale factor to obtain the nominal background prediction. The standard deviation of this distribution is multiplied by the scale factor to obtain the statistical uncertainty on the background prediction.

Systematically-shifted background yield predictions are determined by repeating the above procedure for the systematically-shifted dressed M_J^Σ values. The systematic uncertainties are taken as the difference between the nominal and systematically-shifted background yield predictions. Scale factors are only derived from the nominal M_J^Σ distributions and applied to both the nominal and systematically-shifted predictions.

The two systematic uncertainties are symmetrized by taking the maximum of the downward-shifted and upward-shifted uncertainties.

Dressed Mass Response

Dressed mass response plots are created by plotting the average dressed and average kinematic jet mass in each p_T bin. The dressed mass response for the control region is shown in figure 6.4. Good agreement between average dressed and kinematic masses is observed in this region, because the dressing procedure is applied to the same jets from which the templates are derived.

Dressed mass response plots in other regions are used to evaluate how well the mass templates generalize to events with different jet multiplicities. In the absence of signal events, a disagreement between the average dressed and kinematic masses would indicate that an individual jet mass is dependent on the number of jets in that jet's event, violating the assumptions of the template method.

A data-driven method is used to estimate the extent to which this assumption is violated, and the size of the effect this can have on the background estimation uncertainty. This method is described in 6.6

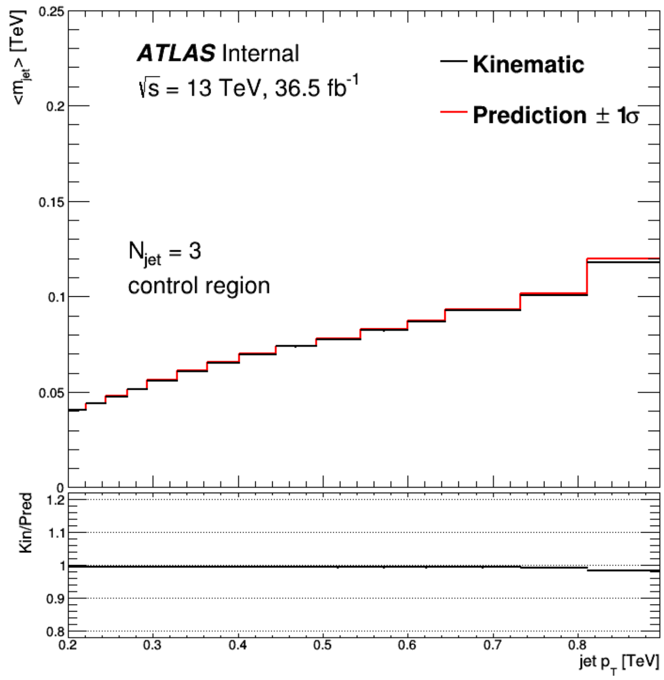

Figure 6.4: Average dressed and kinematic jet masses for each p_T bin in the control region

6.4 Event Selection

This analysis uses the entire 2015 and 2016 ATLAS datasets, comprising 36.1 fb^{-1} ($\pm 2.1\%$). All collisions occurred as $\sqrt{s} = 13\ TeV$.

The trigger selects events with $H_T > 1.0\ TeV$, where H_T is the scalar sum of the p_T of all jets in an event. The trigger efficiency for the benchmark signal samples is found to be 100%.

Additional requirements are that events have a primary vertex formed from at least two tracks with $p_T > 400\ MeV$.

Two different methods of reconstructing jets are used in the analysis. Large-R jets are reconstructed using the anti-k_T algorithm with radius parameter $R = 1.0$, and sub-jet radius parameter $R_{sub-jet} = 0.2$. The jets are trimmed with sub-jet p_T-fraction $f_{p_T} = 0.05$. The details of how jets are reconstructed, trimmed, and calibrated can be found in chapter **??**.

Small-R jets are reconstructed with the anti-k_T algorithm, using radius parameter $R = 0.4$.

Large-R jets are required to have $p_T > 200\ GeV$ and $|\eta| < 2.0$. The leading large-R jet is required to have $p_T > 440\ GeV$, a selection for which the H_T trigger is fully efficient.

Small-R jets are used as candidates for b-tagging. To be considered for b-tagging, a small-R jet must have $p_T > 50\ GeV$ and $|\eta| < 2.5$. The algorithm used to tag b-jets is described in chapter **??** as well as [14, 13]. The algorithm used for b-tagging in this analysis is the fixed-efficiency 70% working point.

The control, validation, and signal regions defined in section 6.5 can be further segmented into b-tag and b-veto regions. Events with at least one b-tagged small-R jet are considered b-tag events, while those without are labelled as b-veto. When b-tagging is not taken into consideration, the region is called b-inclusive.

Additionally, large-R jets found to be within $\Delta R = 1.0$ of a b-tagged small-R jet in the same event are referred to as b-matched jets. Those large-R jets not within $\Delta R = 1.0$ of a b-tagged small-R jet are called non-b-matched.

The distinction in terminology between b-tagged and b-matched is important enough to restate for clarity. When referring to the presence or absence of a b-tagged jet *within an event*, the terms b-tag, b-veto, and b-inclusive are used. When referring to the proximity of an *individual large-R jet* to a b-tagged small-R jet, the terms b-matched and non-b-matched are used.

Templates will be divided into b-matched and non-b-matched templates, which are used to dress b-matched and non-b-matched jets, respectively. Validation and signal regions will be divided into b-tag, b-veto, and b-inclusive regions.

6.5 Control, Uncertainty Determination, Validation, and Signal Regions

Events are divided into control, uncertainty determination, validation, and signal regions.

The control region is used to derive the jet mass templates, as described in section 6.3. The control region is defined as those events with exactly three large-R jets.

There are two uncertainty determination regions (UDRs), which are used to derive the data-driven background systematic uncertainty, as detailed in section 6.6. The high-p_T UDR, known as UDR1, consists of events with exactly two large-R jets, with at least one having $p_T > 400\ GeV$. The low-p_T UDR, known as UDR2, consists of events with exactly four large-R jets, all of which have $p_T < 400\ GeV$. The UDRs are independent of the control, validation, and signal regions.

Validation region are used to check that the template method accurately estimates the M_J^Σ distribution in high-multiplicity events that are free of signal contamination. Requiring large $|\Delta\eta|$ reduces the signal contribution to the high-multiplicity regions. There are four overlapping validation regions, each requiring $|\Delta\eta| > 1.4$. The validation regions are divided into two b-tag and two b-inclusive regions. The b-tag regions require at least one b-tagged small-R jet, while the b-inclusive regions have no such requirement. The b-tag and b-inclusive regions are further subdivided into 4-jet and 5-jet regions. The 4-jet regions require *at least* four large-R jets, and leading jet $p_T > 400 GeV$ so that they are independent of UDR2. The 5-jet regions require five or more large-R jets, and have no requirement on the leading jet p_T.

Table 6.1: Summary of the requirements defining the control, uncertainty determination, validation, and signal regions. Requirements are placed on the large-R jet multiplicity (N_{jet}), the presence or absence of a b-tagged small-R jet (b-tag), the p_T of the leading jet ($p_{T,1}$), the pseudorapidity difference between the two leading jets ($|\Delta\eta_{12}|$), and the scalar sum of the first four leading jets in the event (M_J^Σ).

		N_{jet} (p_{T} > 200 GeV)	b-tag	$p_{T,1}$	$\lvert\Delta\eta_{12}\rvert$	M_{J}^{Σ}
CR	3jCR	= 3	-	-	-	-
UDR	UDR1	= 2	-	> 400 GeV	-	-
	UDR2	= 4	-	< 400 GeV	-	-
VR	4jVRb	≥ 4	Yes	> 400 GeV	> 1.4	-
	5jVRb	≥ 5	Yes	-	> 1.4	-
	4jVR	≥ 4	-	> 400 GeV	> 1.4	-
	5jVR	≥ 5	-	-	> 1.4	-
SR	4jSRb	≥ 4	Yes	> 400 GeV	< 1.4	> 1.0 TeV
	5jSRb	≥ 5	Yes	-	< 1.4	> 0.8 TeV
		≥ 5	Yes	-	< 1.4	> 0.6 TeV
	4jSR	≥ 4	-	> 400 GeV	< 1.4	> 1.0 TeV
	5jSR	≥ 5	-	-	< 1.4	> 0.8 TeV

The signal regions are divided the same way as the validation regions, into two b-tag regions: one with four or more jets, and one with five or more jets, as well as a two corresponding b-inclusive regions. The four-jet signal regions also require lead jet $p_T > 400GeV$, like the validation region. The difference between the signal and validation regions is a reversal of the $|\Delta\eta|$ requirement. All signal regions require $|\Delta\eta| < 1.4$. Additionally, the signal regions include a requirement on M_J^Σ. The four-jet b-tag signal region (4jSRb) and 4-jet b-inclusive signal region (4jSR) each require $M_J^\Sigma > 1.0\ TeV$. The five-jet b-tag signal region (5jSRb) is divided into two overlapping regions: one with a cut of $M_J^\Sigma > 0.6\ TeV$ and one with a cut of $M_J^\Sigma > 0.8\ TeV$. Finally, the five-jet b-inclusive region (5jSR) requires $M_J^\Sigma > 0.8\ TeV$.

A summary of the definitions for the control, uncertainty determination, validation, and signal regions can be found in table 6.1.

6.6 Background Systematic Uncertainty

A data-driven background systematic uncertainty is derived from the uncertainty determination regions. As can be seen in figure 6.5, the dressing procedure tends to under-predict jet masses in UDR1 and over-predict jet masses in UDR2. The degree of discrepancy depends strongly on p_T and the choice of UDR. Separate uncorrelated systematic uncertainties are derived for jets with $p_T < 400\ GeV$ and those with $p_T < 400\ GeV$. Since the discrepancy is larger in UDR1 than UDR2 for jets with $p_T < 400\ GeV$, UDR1 is used to derive the uncertainty for those jets. For jets with $p_T < 400\ GeV$, uncertainties are correlated across p_T and $|\eta|$ bins, and likewise for jets with $p_T > 400\ GeV$.

Binning of systematics

Systematic uncertainties are binned in p_T and $|\eta|$. The lowest p_T bin is for jets with $p_T < 400\ GeV$. The second bin is for jets with $400\ GeV \leq p_T < 544\ GeV$, and the highest bin is for jets with $p_T \geq 544\ GeV$.

Deriving uncertainty

For jets with $p_T \geq 400\ GeV$, uncertainties are derived only from UDR1.

For jets with $p_T < 400\ GeV$, uncertainties are derived from both UDR1 and UDR2, and the maximum uncertainty is used.

For each p_T bin in the UDR dressed mass response, a fractional error is calculated as $e_i = (< m_{kin} > - < m_{dressed} >) \,/ < m_{dressed} >$.

For the lowest and highest p_T systematic bins, the root-mean-square of fractional errors is taken as the systematic error. For the intermediate systematic bin, the maximum fractional error is taken

Propagation of uncertainty

Two separate, uncorrelated systematic uncertainties are derived. The first uncertainty accounts for the discrepancy between dressed and kinematic masses for jets with $p_T \geq 400\ GeV$, and the second accounts for the discrepancy for jets with $p_T < 400\ GeV$.

To propagate the low-p_T systematic, two shifted M_J^Σ values are calculated for each dressed M_J^Σ. The first shifted value is obtained by increasing the dressed mass of every low-p_T jet by its corresponding fractional uncertainty. This yields n_{toys} histograms of shifted M_J^Σ. The average value of each bin content over all toys is taken to obtain the systematically-shifted M_J^Σ distribution.

The second shifted distribution is obtained by decreasing the dressed mass of every low-p_T jet by its corresponding fractional uncertainty, and averaging over all the toys to obtain a downwards-shifted distribution of M_J^Σ.

The same procedure is used to propagate the high-p_T systematic, but the high-p_T jets are shifted instead of the low-p_T jets.

6.7 Signal Contamination

The presence of signal events in the kinematic sample can affect both the nominal background prediction as well as the systematic uncertainty. This effect can be quantified using a signal injection test. The background prediction is first calculated from a data sample only, and then calculated from a data sample injected with simulated signal events.

One example of this effect can be seen in figure 6.6. For this example, only the first 14.8 fb^{-1} of data are used. The injected signal simulates the cascade decay mode of gluinos with mass $m_{\tilde{g}} = 1.8\ TeV$ and neutralinos with mass $m_{\tilde{\chi}} = 50\ GeV$. For this particular choice of masses and decay mode, the background prediction is increased by approximately 10%, from 18.3 events to 20.2 events. Additionally, the systematic uncertainty is increased from 8.9 events to 13.3 events.

The effect of signal contamination on the background prediction has to be measured separately at each signal point. For each gluino and neutralino mass point, the background prediction is generated using only simulated signal events in the kinematic sample. That is, the templates are still derived from data, but the dressing is only performed on simulated signal. The signal events don't need to be included in the templates because the template control region choice reduces any signal contribution in that region to a negligible amount.

The prediction from the signal-only kinematic sample is then compared to the data-only prediction. Figure 6.7 shows the ratio of background prediction from signal-only events over the background prediction from data alone. During hypothesis testing, these ratios will be used to subtract off the signal contamination contribution to the background prediction at each signal point separately.

The signal region used for this test is the 5-jet, b-tag region, requiring $M_J^{\Sigma} > 0.8\ TeV$.

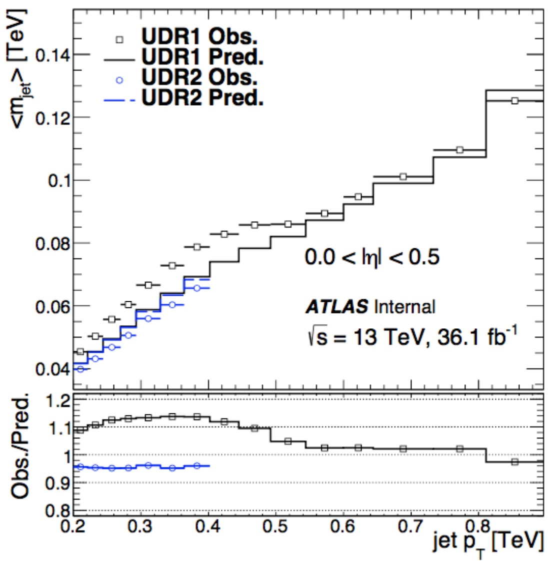

(a) $|\eta| < 0.5$

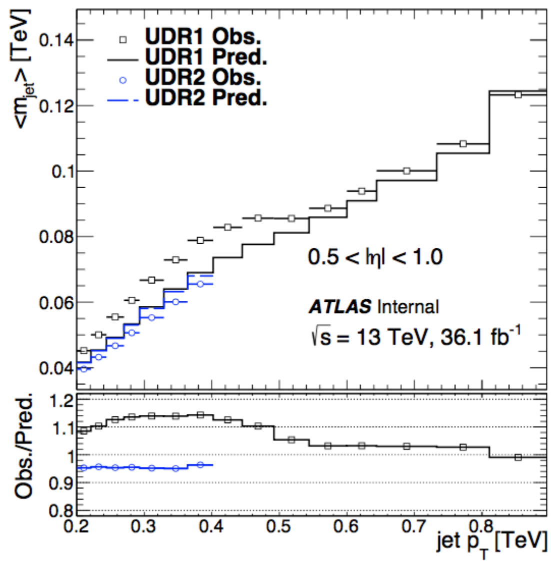

(b) $0.5 < |\eta| < 1.0$

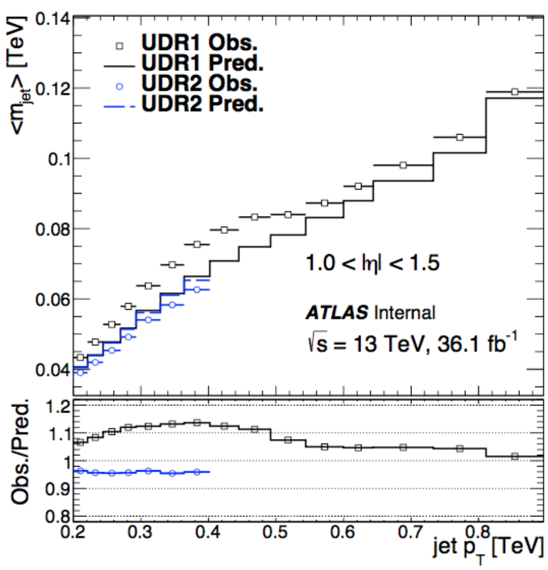

(c) $1.0 < |\eta| < 1.5$

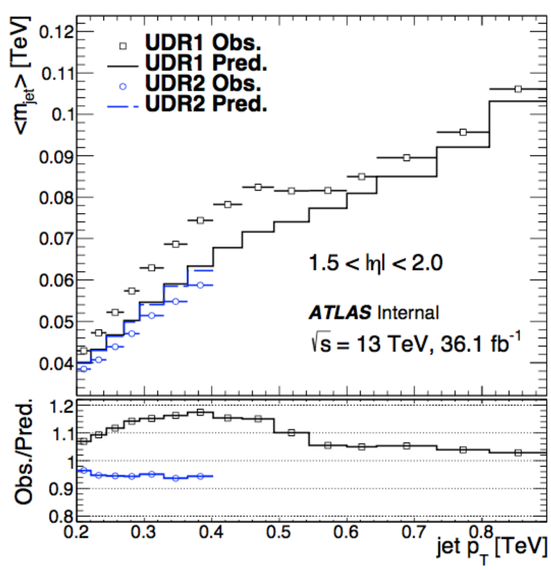

(d) $1.5 < |\eta| < 2.0$

Figure 6.5: Jet mass response plots showing the discrepancy between average dressed and kinematic jet masses in the two uncertainty determination regions, binned by p_T and $|\eta|$. Since the discrepancy is always larger in UDR1, only UDR1 is used to derive uncertainties.

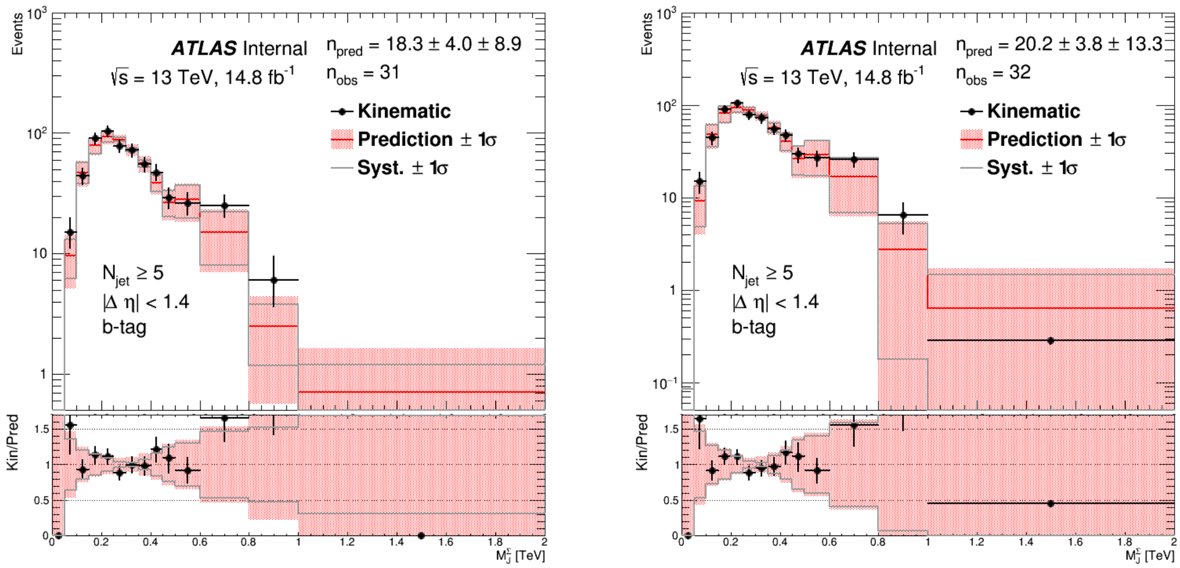

Figure 6.6: Signal injection test. The background prediction is first run only on a data sample (a), and then on a data sample injected with simulated signal events (b). The increase in background prediction and systematic uncertainty can be seen.

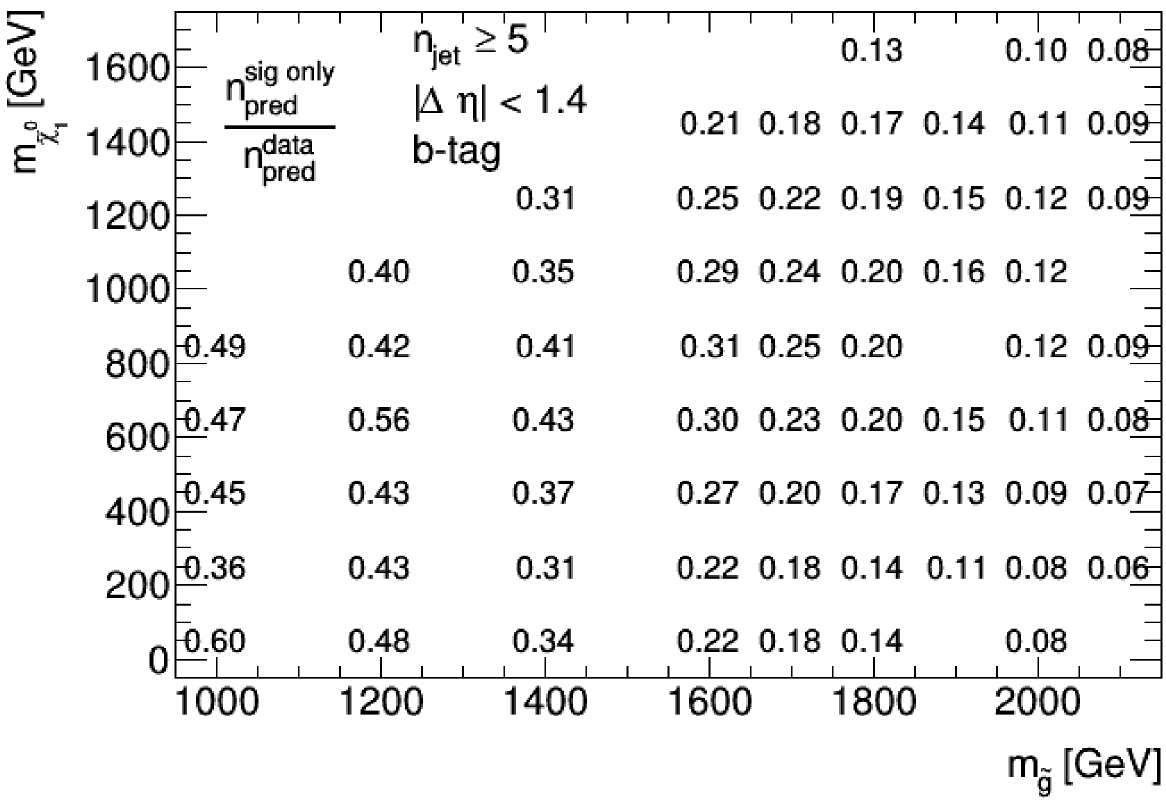

Figure 6.7: The effect of signal contamination on the nominal background prediction. At each neutralino and gluino mass, simulated signal events are used in the kinematic sample to generate a background prediction. These predictions are compared to the prediction from data only. In both cases, the templates are drawn only from data.

Chapter 7

Signal Modelling and Systematics

7.1 Signal Modeling

7.2 Signal Systematic Uncertainties

There are four main components to the systematic uncertainty on the estimated signal yield. These components are the large-R jet mass scale (JMS), the small-R b-tagging uncertainty, the Monte Carlo statistical uncertainty, and the modelling uncertainty, which includes uncertainty on parton distribution functions (PDFs), QCD scale uncertainty, and initial state radiation (ISR) modelling uncertainty.

A given systematic is evaluated by varying a nuisance parameter and determining the percent difference in signal yield between the nominal distribution and systematically varied distribution. When a systematic contains multiple components, those components are treated as uncorrelated, and their contributions are combined in quadrature.

Systematic uncertainties depend on the gluino and neutralino masses being considered, as well as the decay mode of direct or cascade. As such, they are evaluated separately at each point in the mass grid.

Jet Mass Scale Uncertainty

For the JMS uncertainty, there are four components, called the baseline, modeling, statistical, and tracking components. These components are derived from the R_{trk} method [1]. The JMS uncertainty is largest for $m_{\tilde{g}} = 1.0\ TeV$, at $\approx 24\%$, and drops to $\approx 8\%$ for signal points with $m_{\tilde{g}} = 1.8\ TeV$. It is generally dominated by the tracking uncertainty, followed by the baseline uncertainty.

b-Tagging Uncertainty

The b-tagging uncertainty is evaluated by varying a set of 25 nuisance parameters. The result is an uncertainty on the signal efficiency of between 15% and 25%. This uncertainty is only applied to the b-tag signal regions.

Monte Carlo Statistical Uncertainty

The Monte Carlo statistical uncertainty accounts for the fact that only a limited sample of simulated events are produced for each mass point. The uncertainty is derived as $\sigma = \sqrt{\epsilon(1-\epsilon)/N}$, where ϵ is the efficiency measured in the sample, and N is the sample size.

PDF, QCD scale, and ISR Uncertainties

Evalulating the contribution to the signal efficiency uncertainty from PDF, α_s and ISR modelling uncertainties requires the generation of truth-level signal simulation samples where different parameters are varied in the generation.

For PDF uncertainties, the internal event weights in the PDF set are varied up and down during the generation.

For the QCD scale uncertainty, the value of $alpha_s$ is varied up and down durin the generation.

For ISR uncertainties, the value of the matching scale, q_{cut} is varied up and down during the generation.

The PDF and QCD scale contributions to the uncertainty are highest at low gluino mass, reaching a maximum of 25% at $m_{\tilde{g}} = 1.0\ TeV$, the lowest gluino mass studied. For higher masses, these uncertainties drop to only a few percent.

Summary

The various signal systematic uncertainties are summarized in table **??**

Chapter 8

Results

8.1 Data-driven Background Uncertainty

8.2 Background Predictions and Observed Yields in Signal Regions

8.3 Signal Systematics

8.4 Statistical Interpretation

8.5 Expected and Observed Limits

Ten-quark model

Six-quark model

Model-independent limits

Chapter 9

Conclusions

Bibliography

[1] In: ().

[2] G. 't Hooft. "Symmetry Breaking through Bell-Jackiw Anomalies". In: *Phys. Rev. Lett.* 37 (1 July 1976), pp. 8–11. DOI: 10.1103/PhysRevLett.37.8. URL: https://link.aps.org/doi/10.1103/PhysRevLett.37.8.

[3] Georges Aad et al. "Topological cell clustering in the ATLAS calorimeters and its performance in LHC Run 1". In: *Eur. Phys. J.* C77 (2017), p. 490. DOI: 10.1140/epjc/s10052-017-5004-5. arXiv: 1603.02934 [hep-ex].

[4] A. Hook et al. "High Multiplicity Searches at the LHC Using Jet Masses". In: *JHEP* 3 (2012), p. 9.

[5] S. El Hedri et al. "Learning How to Count: A High Multiplicity Search for the LHC". In: *JHEP* (2013), p. 136.

[6] Ryan Atkin. "Review of jet reconstruction algorithms". In: *Journal of Physics: Conference Series* 645.1 (2015), p. 012008. URL: http://stacks.iop.org/1742-6596/645/i=1/a=012008.

[7] G. C. Blazey et al. "Run II Jet Physics: Proceedings of the Run II QCD and Weak Boson Physics Workshop". In: *ArXiv High Energy Physics - Experiment e-prints* (May 2000). eprint: hep-ex/0005012.

[8] M. Cacciari, G. P. Salam, and G. Soyez. "The anti-k_t jet clustering algorithm". In: *Journal of High Energy Physics* 4, 063 (Apr. 2008), p. 063. DOI: 10.1088/1126-6708/2008/04/063. arXiv: 0802.1189 [hep-ph].

[9] Matteo Cacciari, Gavin P. Salam, and Gregory Soyez. "FastJet user manual". In: *The European Physical Journal C* 72.3 (Mar. 2012), p. 1896. ISSN: 1434-6052. DOI: 10.1140/epjc/s10052-012-1896-2. URL: https://doi.org/10.1140/epjc/s10052-012-1896-2.

[10] ATLAS Collaboration. *A New Sub Detector for ATLAS*. 2014. URL: http://atlasexperiment.org/news/2014/a-new-sub-detector-for-ATLAS.html (visited on 06/02/2014).

[11] ATLAS Collaboration. "ATLAS Insertable B-Layer Technical Design Report". In: *CERN/LHCC 2010-013*. 2010.

[12] ATLAS Collaboration. "ATLAS Pixel Detector Electronics and Sensors". In: *JINST* 3 (2008), P07007.

[13] ATLAS Collaboration. "Optimisation of the ATLAS b-tagging performance for the 2016 LHC Run". In: (2016). URL: http://cds.cern.ch/record/2160731.

[14] ATLAS Collaboration. "Performance of b-Jet Identification in the ATLAS Experiment". In: *JINST* 11 (2016), P04008.

[15] ATLAS Collaboration. "Search for massive supersymmetric particles decaying to many jets using the ATLAS detector in pp collisions at $\sqrt{s} = 8\ TeV$". In: *Phys. Rev. D* (2015).

[16] ATLAS Collaboration. "The ATLAS Experiment at the CERN Large Hadron Collider". In: *JINST* 3 (2008), S08003.

[17] ATLAS Collaboration. "The ATLAS Transition Radiation Tracker (TRT) proportional drift tube: design and performance". In: *JINST* 2 (2013), P02013.

[18] ATLAS Collaboration. "The barrel modules of the ATLAS semiconductor tracker". In: *Nuclear Instruments and Methods in Physics Research* 568 (2 2006).

[19] Savas Dimopoulos and Howard Georgi. "Softly broken supersymmetry and SU(5)". In: *Nuclear Physics B* 193.1 (1981), pp. 150–162. ISSN: 0550-3213. DOI: https://doi.org/10.1016/0550-3213(81)90522-8. URL: http://www.sciencedirect.com/science/article/pii/0550321381905228.

[20] S. D. Ellis et al. "Jets in hadron-hadron collisions". In: *Prog. Part. Nucl. Phys.* 60 (2008), pp. 484–551. DOI: 10.1016/j.ppnp.2007.12.002. arXiv: 0712.2447 [hep-ph].

[21] Lyndon Evans and Philip Bryant. "LHC Machine". In: *Journal of Instrumentation* 3.08 (2008), S08001. URL: http://stacks.iop.org/1748-0221/3/i=08/a=S08001.

[22] Tanju Gleisberg et al. "SHERPA 1. alpha: A Proof of concept version". In: *JHEP* 02 (2004), p. 056. DOI: 10.1088/1126-6708/2004/02/056. arXiv: hep-ph/0311263 [hep-ph].

[23] P Haefner. "The ATLAS silicon microstrip tracker. Operation and performance". In: *JINST* 5 (2010), p. C12050.

[24] D. Hanneke, S. Fogwell, and G. Gabrielse. "New Measurement of the Electron Magnetic Moment and the Fine Structure Constant". In: *Phys. Rev. Lett.* 100 (12 Mar. 2008), p. 120801. DOI: 10.1103/PhysRevLett.100.120801. URL: https://link.aps.org/doi/10.1103/PhysRevLett.100.120801.

[25] Ian Hinchliffe and Thomas Kaeding. "*B*- and *L*-violating couplings in the minimal supersymmetric standard model". In: *Phys. Rev. D* 47 (1 Jan. 1993), pp. 279–284. DOI: 10.1103/PhysRevD.47.279. URL: https://link.aps.org/doi/10.1103/PhysRevD.47.279.

[26] John E. Huth et al. "Toward a standardization of jet definitions". In: *1990 DPF Summer Study on High-energy Physics: Research Directions for the Decade (Snowmass 90) Snowmass, Colorado, June 25-July 13, 1990*. 1990, pp. 0134–136. URL: http://lss.fnal.gov/cgi-bin/find_paper.pl?conf-90-249.

[27] G. Jungman, M. Kamionkowski, and K. Griest. "Supersymmetric dark matter". In: *Phys.Rept.* 267 (Mar. 1996), pp. 195–373. DOI: 10.1016/0370-1573(95)00058-5. eprint: hep-ph/9506380.

[28] Glenn F. Knoll. *Radiation Detection and Measurement*. John Wiley and Sons, 2000.

[29] "LHC Guide". Mar. 2017. URL: http://cds.cern.ch/record/2255762.

[30] A. D. Martin, W. J. Stirling, and G. Thorne R. S.and Watt. "Parton distributions for the LHC". In: *The European Physical Journal C* 63.2 (Sept. 2009), pp. 189–285.

[31] S. P. Martin. "A Supersymmetry Primer". In: *Perspectives on Supersymmetry. Edited by KANE GORDON L. Published by World Scientific Publishing Co. Pte. Ltd., 1998. ISBN #9789812839657, pp. 1-98*. Ed. by G. L. Kane. World Scientific Publishing Co, 1998, pp. 1–98. DOI: 10.1142/9789812839657_0001.

[32] R. N. Mohapatra. "Supersymmetric Grand Unification". In: *ArXiv High Energy Physics - Phenomenology e-prints* (Jan. 1998). eprint: hep-ph/9801235.

[33] H. Murayama. "Supersymmetry Phenomenology". In: *Particle Physics*. Ed. by G. Senjanović and A. Y. Smirnov. 2000, p. 296. eprint: hep-ph/0002232.

[34] N. Nikiforou. "Performance of the ATLAS Liquid Argon Calorimeter after three years of LHC operation and plans for a future upgrade". In: *ArXiv e-prints* (June 2013). arXiv: 1306.6756 [physics.ins-det].

[35] K.A. Olive and Particle Data Group. "Review of Particle Physics". In: *Chinese Physics C* 38.9 (2014), p. 090001. URL: http://stacks.iop.org/1674-1137/38/i=9/a=090001.

[36] S. Palestini. "The muon spectrometer of the ATLAS experiment". In: *Nucl. Phys. Proc. Suppl.* 125 (2003). [,337(2003)], pp. 337–345. DOI: 10.1016/S0920-5632(03)91013-9.

[37] Gavin P. Salam. "Towards jetography". In: *The European Physical Journal C* 67.3 (June 2010), pp. 637–686. ISSN: 1434-6052. DOI: 10.1140/epjc/s10052-010-1314-6. URL: https://doi.org/10.1140/epjc/s10052-010-1314-6.

[38] Jessie Shelton. "TASI Lectures on Jet Substructure". In: (Feb. 2013).

[39] Peter Speckmayer, Tancredi Carli, and Christian Wolfgang Fabjan. "Energy Measurement of Hadrons with the CERN ATLAS Calorimeter". Presented on 18 Jun 2008. 2008. URL: http://cds.cern.ch/record/1112036.

[40] Helmuth Spieler. *Semiconductor Detector Systems*. Oxford Science Publications, 2005.

[41] AC Team. "Diagram of an LHC dipole magnet. Schéma d'un aimant dipôle du LHC". June 1999. URL: https://cds.cern.ch/record/40524.